TEMPERATURE DETECTION USING MICRO PLATE VIBRATIONS

A THESIS SUBMITTED TO
THE GRADUATE SCHOOL OF NATURAL AND APPLIED SCIENCES
OF
MIDDLE EAST TECHNICAL UNIVERSITY

BY

SEDAT PALA

IN PARTIAL FULFILLMENT OF THE REQUIREMENTS
FOR
THE DEGREE OF MASTER OF SCIENCE
IN
MECHANICAL ENGINEERING

JUNE 2017

Approval of the thesis:

TEMPERATURE DETECTION USING MICRO PLATE VIBRATIONS

submitted by **SEDAT PALA** in partial fulfillment of the requirements for the degree of **Master of Science in Mechanical Engineering Department, Middle East Technical University** by,

Prof. Dr. Gülbin Dural Ünver ____________________
Dean, **Graduate School of Natural and Applied Science**

Prof. Dr. R. Tuna Balkan ____________________
Head of Department, **Mechanical Engineering**

Assist. Prof. Dr. Kıvanç Azgın ____________________
Supervisor, **Mechanical Eng. Dept., METU**

Examining Committee Members:

Prof. Dr. Mehmet Çalışkan ____________________
Mechanical Engineering Dept., METU

Assist. Prof. Dr. Kıvanç Azgın ____________________
Mechanical Engineering Dept., METU

Prof. Dr. Fevzi Suat Kadıoğlu ____________________
Mechanical Engineering Dept., METU

Assist. Prof. Dr. F. Nazlı Dönmezer Akgün ____________________
Mechanical Engineering Dept., METU

Assist. Prof. Dr. Ender Yıldırım ____________________
Mechanical Engineering Dept., Çankaya University

Date: 19.06.2017

I hereby declare that all information in this document has been obtained and presented in accordance with academic rules and ethical conduct. I also declare that, as required by these rules and conduct, I have fully cited and referenced all material and results that are not original to this work.

Name, Last name : Sedat Pala

Signature :

ABSTRACT

TEMPERATURE DETECTION USING MICRO PLATE VIBRATIONS

Pala, Sedat

M.Sc., Department of Mechanical Engineering

Supervisor: Assist. Prof. Dr. Kıvanç Azgın

June 2017, 97 pages

This thesis presents the design, modelling, fabrication and characterization of a resonant MEMS plate temperature sensor. In the proposed application, temperature change is measured by tracking natural frequency shifts of a specific mode shape of the resonating micro plate.

The design and modelling of the resonant MEMS plate temperature sensor are conducted for Chladni plate geometry that is square plate supported at the geometric center, having all edges free to move. Energy methods are utilized to solve the equation of motion of transversely vibrating Chladni plate structure to obtain the closed form equations for the mode shapes and respective natural frequencies with electrostatic softening effect. Thermo-electro-mechanical model is derived with the addition of thermal effect on top of the electromechanical solution. Finite Element (FE) simulations are conducted for each step of analytical model to verify the derived model.

The designed sensors are fabricated using a silicon-on-glass (SOG) process. The fabricated temperature sensors are characterized with frequency response and system level temperature tests. The Q-factors of modes (1,1) and (2,0) - (0,2) are measured to be 14300 and 10700 at a vacuum pressure level of 20mTorr, respectively. The Laser Doppler Vibrometer (LDV) tests at vacuum level of 0.364mTorr verify the analytical model and FE simulations. In addition, effect of electrostatic softening is also tested for a proof mass voltage range of 0-40V, and corresponding frequency shift is measured to be 0-26Hz. System level temperature tests are done with a Phase Locked Loop (PLL) to track frequency drifts with changing temperature at vacuum level of 0.405mTorr. The scale factor of the fabricated sensor is obtained as 2.0214Hz/°C and 2.7211Hz/°C for mode shapes (1,1) and (2,0) - (0,2), respectively. The temperature equivalent frequency instabilities of the fabricated sensor are measured to be 0.3725mK for (1,1) mode shapes and 0.1499mK for (2,0) - (0,2) mode shape.

Keywords: MEMS, micro plate, MEMS resonator, Chladni Plate, MEMS Resonant Temperature Sensor, Temperature Sensing.

ÖZ

MİKRO PLAKA TİTREŞİMLERİNİ KULLANARAK SICAKLIK TESPİTİ

Pala, Sedat

Yüksek Lisans, Makina Mühendisliği Bölümü

Tez Yöneticisi: Yrd. Doç. Dr. Kıvanç Azgın

Haziran 2017, 97 sayfa

Bu tez rezonant MEMS plaka sıcaklık sensörünün tasarım, modelleme, üretim ve karekterizasyonunu sunmaktadır. Önerilen uygulamada sıcaklık değişimi, titreyen mikro plakanın belirli titreşim biçimine ait doğal frekansındaki değişim takip edilerek ölçülür.

Rezonant MEMS plaka sıcaklık sensörünün tasarımı ve modellenmesi Chladni plaka geometrisi, geometrik merkezinden destekelnen ve tüm kenarları hareket edebilmesi için serbest olan kare plaka için yapıldı. Titreşim biçimleri ve bunlara karşılık gelen elektrosatik yumuşama etkisinin dahil edildiği doğal frekanslar için kapalı denklemler elde edebilmek amacıyla, enine titreşen Chladni plakanın hareket denklemlerinin çözümünde enerji yöntemleri kullanıldı. Elde edilen elektomekanik çözüme ısıl etkiler dahil edilerek termo-elektro-mekanik model elde edildi. Türetilmiş analitik modelin her bir adımını doğrulamak için Sonlu-Eleman (SE) benzetimleri yürütülmüştür.

Tasarımları yapılan sensörler cam üzeri silicon yöntemi ile üretilmiştir. Üretilen sıcaklık sensörleri frekans tepki ve sistem düzeyinde sıcaklık testleri ile karakterize edilmiştir. Titreşim şekli (1,1) ve (2,0) - (0,2) ait Q-faktörleri 20mTorr vakum basıncı seviyesinde sırasıyla 14300 ve 10700 olarak ölçülmüştür. 0.364mTorr vakum seviyesindeki Lazer Doppler Titreşimölçer (LDT) testleri analitik modelden ve SE benzetimlerinden elde edilen değerleri doğrulamaktadır. Buna ek olarak, elektrostatik tahrikin etkisi 0-40V arasında gövde kütle voltajı için test edilmiştir ve karşılık gelen doğal frekans kayması 0-26Hz olarak ölçülmüştür. Sistem seviyesi sıcaklık tesleri, sıcaklık değişimiyle kayan frekansı takip edebilmek için Faz Kilitli Döngü (FKD) ile birlikte 0.405mTorr vakum seviyesinde yapılmıştır. Üretilen sensörlerin ölçek çarpanı titreşim şekli (1,1) ve (2,0) - (0,2) için sırasıyla 2.0214Hz/°C ve 2.7211Hz/°C olarak ölçülmüştür. Üretilen sensörlerin sıcaklık eşdeğer frekans kararsızlıkları titreşim şekli (1,1) için 0.3725mK ve titreşim şekli (2,0) - (0,2) için 0.1499mK olarak ölçülmüştür.

Anahtar Sözcükler: MEMS, mikro plaka, MEMS rezonatör, Chladni plaka, MEMS resonant sıcaklık sensörü, sıcaklık ölçümü.

To

My Dear Parents, Fatma & Bahattin

My Elder Brother, Selçuk

Your endless love, support and patience made this possible…

ACKNOWLEDGMENTS

I would like to express my deep and sincere gratitude to everybody for their help and support throughout this research. First and most importantly, I would like to thank to my thesis advisor Assist. Prof. Dr. Kıvanç Azgın not only for guidance, criticism and encouragement, but also his friendly attitude. He has transformed a newly graduated engineer into a motivated MEMS researcher. It was a privilege for me to work with him.

I would like to thank Talha Köse and METU MEMS Center staff for their help in microfabrication processes and clean room trainings. I am also thankful to former group member Utku Göreke for the support, belief in my ideas and didactic discussions. Special thanks to Onurcan Kaya for his help in the tests and, before anything, for his great friendship and being a challenging colleague. I would like to express my deep thanks to Necati Emre Kesici, Tayfun Efe Ertop, Yezdan Atılgan, Melek Dicle Özcan, Tuğçe Çevik, Aslı Gülbike Uluyurt, and all my other friends, they were there whenever I need. Besides, I am also thankful to technicians in the Heat Transfer Lab and Machine Shop for sharing their valuable experiences with me.

I would like to thank the Scientific and Technological Research Council of Turkey (TÜBİTAK) for the scholarship with the code BİDEB 2210.

Most importantly, I want to express my deepest gratitude to my mother, Fatma, my father, Bahattin, and my elder brother, Selçuk. Feeling their endless support and love motivates me at the most desperate times in my life. They made possible whatever I have achieved so far. This study is dedicated to my family.

TABLE OF CONTENTS

ABSTRACT v

ÖZ vii

DEDICATION ix

ACKNOWLEDGMENTS x

TABLE OF CONTENTS xi

LIST OF TABLES xiv

LIST OF FIGURES xv

LIST OF ABBREVIATIONS xx

CHAPTERS

1. INTRODUCTION 1

  1.1. Vibration of Plates and the Chladni Plate 2

  1.2. MEMS Resonators 4

  1.3. Temperature Detection 5

  1.4. Research Objectives and Thesis Organization 8

2. DESIGN AND MODELLING OF RESONANT MEMS PLATE TEMPERATURE SENSOR 11

2.1. Basic Concepts in Plate Vibration Theory 12

2.2. Resonant MEMS Plate Temperature Sensor 14

2.2.1. Physical Structure of the MEMS Plate Resonator 14

2.2.2. Geometric Dimensions and Specifications of the Design 15

2.3. Modelling of Resonant MEMS Plate Temperature Sensor 18

2.3.1. Analytical Model of MEMS Square Plate Vibrations 19

2.3.1.1. Equation of Motion: Equilibrium Approach 20

2.3.1.2. Equation of Motion: Variational Approach 24

2.3.1.3. Solution of EOM of Plate Using Rayleigh – Ritz Method 28

2.3.2. Analytical Model of Capacitive Actuation and Detection 37

2.3.2.1. Capacitive Actuation 37

2.3.2.2. Capacitive Detection 40

2.3.2.3. Softening Effect of Capacitive Actuation 42

2.3.3. Analytical Model of Temperature Effect on Natural Frequencies of Modes-of-Interest 46

2.4. Finite Element Modelling of Resonant MEMS Plate Temperature Sensor. 48

2.4.1. Static Deflection and Pull-in Voltage Simulation of MEMS Plate 49

2.4.2. Modal Simulations of the Resonant MEMS Square Plate 52

2.4.3. Finite Element Model Simulations of the Electrostatic Effect 54

2.4.4. Finite Element Model Simulations of the Thermal Effect 56

2.5. Summary 58

3. FABRICATION AND CHARACTERIZATION EXPERIMENTS OF RESONANT MEMS PLATE TEMPERATURE SENSOR 59

3.1. Fabrication of Resonant MEMS Plate Temperature Sensor 59

3.1.1. Microfabrication Process Flow 60

3.1.2. Microfabrication Results 62

3.2. Frequency Response Characterization Tests 63

3.2.1. Frequency Response Test Setup 64

3.2.2. Frequency Response Test Results 65

3.2.3. Laser Doppler Vibrometer Test Results 70

3.2.4. Electrostatic Softening Effect Test Results 72

3.3. System Level Temperature Tests 73

3.3.1. System Level Temperature Test Setup 74

3.3.2. System Level Temperature Test Results 77

3.4. Summary 84

4. CONCLUSION AND FUTURE WORK 87

REFERENCES 91

LIST OF TABLES

TABLES

Table 2.1: Summary of the geometric dimensions, the material parameters for the plate resonator and some of the test parameters used in this study. See Figure 2.2 for variable definitions. 17

Table 2.2: Obtained mode shapes for mode-of-interest with Rayleigh-Ritz method. Mode shapes are normalized with respect to second norm of coefficient vector. 35

Table 2.3: Closed form equations for equivalent stiffness, mass and un undamped natural frequencies for modes-of-interest, which are obtained using resulting modes shapes of Rayleigh-Ritz method. 36

Table 2.4: Closed form expressions of electrostatic spring constants for both single square electrode and trapezoidal electrodes 45

Table 2.5: Closed form equation of natural frequency of mode (1,1) with the electrostatic softening effect included for trapezoidal electrode layout. 45

Table 2.6: Closed form equation of natural frequency of mode (2,0) – (0,2) with the electrostatic softening effect included for trapezoidal electrode layout. 46

Table 2.7: Closed form natural frequency equations as a function of temperature for modes-of-interest. 48

LIST OF FIGURES

FIGURES

Figure 1.1: Excitation of the Chladni plate by bowing the plate from one of its free edges and mode shapes of the square plate known as Chladni figures [6, 15]. 3

Figure 1.2: (a) Invasive type temperature sensor in contact with the substrate, (b) Noninvasive type temperature sensor, i.e., IR detector... 6

Figure 2.1: Some of the Chladni plate mode shapes.. 13

Figure 2.2: (a) Schematic of the plate supported at the geometric center with four edges free to move: The coordinate system and geometric dimensions used in modelling are shown. (b) Electrode layouts in the proposed MEMS plate resonator and orientation of electrodes with respect to plate which is shown in dark gray. 15

Figure 2.3: Induced stresses on a differential plate element under de application of bending load and coordinate system used in the modelling...................................... 20

Figure 2.4: Free body diagram of a differential plate element. Force and moment resultants are shown on the four edges of mid plane which coincides with the xy plane of coordinate system. 21

Figure 2.5: Mode shapes of modes-of-interest obtained by assuming characteristic beam function of free-free beam with 16 terms. a) (1,1) mode shape and b) (2,0) – (0,2) mode shape. Underneath the mode shapes counter lines are drawn and green counter lines stand for nodal lines, motionless lines and referred to Chladni figures. 37

Figure 2.6: The capacitance formed by plate and electrodes with applied voltages.. 38

Figure 2.7: Capacitive sensing application. Some of the eight electrodes are used for driving the resonator and the others used for sensing. These electrodes may be interchanged according to mode shape under test. 41

Figure 2.8: Mesh convergence study results done to determine mesh size 49

Figure 2.9: Static deflection pattern with exact electrodes and 15V proof mass 50

Figure 2.10: FE simulation of maximum static deflection of the plate at the corners versus applied DC proof mass voltage. 51

Figure 2.11: Undamped, free vibration modal simulation results obtained via COMSOL Multiphysics for the resonant MEMS square plate with a cylindrical post support at the geometric center. 52

Figure 2.12: Effect of electrostatic softening on the natural frequency of mode (1,1) with analytical model and FE simulation for a single piece of square electrode fully covering the area underneath the plate. 55

Figure 2.13:Effect of electrostatic softening on the natural frequency of mode (1,1) with analytical model and FE simulation for trapezoidal electrode layout. 55

Figure 2.14: Time domain response of the designed resonant MEMS plate temperature sensor. 56

Figure 2.15: Comparison of frequency shifts due to temperature change for the derived analytical model and FE model for mode (1,1) with 15V proof mass applied. 57

Figure 2.16: Comparison of frequency shifts due to temperature change for the derived analytical model and FE model for mode (2,0) - (0,2) with 15V proof mass applied. 57

Figure 3.1: 3D solid model of designed sensor structure. (a) Shows the plate and pads. (b) A portion of the plate is removed to see post, anchors, electrodes and wires clearly. 60

Figure 3.2: Microfabrication steps of the sensor in aMEMS process flow. Given figures are for cross-sectional views of the wafer. (a) The SOI wafer used in the fabrication. (b) DRIE of device layer of SOI wafer to obtained vibrating square plates. (c) The glass wafer used in the fabrication. (d) Wet etching of glass wafer to obtain plate post and anchors. (e) Obtained metal pattern after consecutive thermal evaporation and etching of metal. (f) Anodic bonding of the two wafers. (g) Handle and buried oxide layer of SOI wafer is removed to release the suspended structures. 61

Figure 3.3: Scanning Electron Microscope (SEM) image of the fabricated sensor with the plate removed to have visual access to the electrodes and plate post. 62

Figure 3.4: SEM image of the fabricated sensors 63

Figure 3.5: Experimental setup for the frequency response test of fabricated MEMS plate resonator. 64

Figure 3.6: Read out circuitry used in frequency response tests of mode shape (1,1) of MEMS plate resonator together with network analyzer. 65

Figure 3.7: Frequency response of MEMS plate resonator at 20mTorr vacuum level with 15V proof mass voltage in the frequency span of 63-68 kHz shows the pitch and roll motion of the plate around the axis passing through the post and parallel to x and y axis, respectively. 66

Figure 3.8: Frequency response test result of mode (1,1) of fabricated MEMS plate resonator at 20mTorr vacuum level with 15V proof mass voltage. 67

Figure 3.9: Frequency response test result of mode (2,0) - (0,2) of fabricated MEMS plate resonator at 20mTorr vacuum level with 16V proof mass voltage. 68

Figure 3.10: Frequency response of the fabricated resonator at 20mTorr ambient pressure with 15V proof mass voltage between 22-66 °C 69

Figure 3.11: Frequency response of the fabricated resonator with changing temperature from 22 to 66 °C at 20mTorr ambient pressure. The proof mass voltage is 15V. Both increasing and decreasing cases are presented. 70

Figure 3.12: Frequency response of the plate at vacuum level of 0.364mTorr measured with Ploytec micro system analyzer MSA - 500 Scanning Laser Doppler Vibrometer between 0-175 kHz frequency range at 0.364mTorr vacuum pressure level with 15V proof mass voltage. Mode shapes are measured for the one quarter of the plate due to optical capabilities of the measurement device. 71

Figure 3.13: Test results of electrostatic softening effect on the natural frequency of mode (1,1) with analytical model and FE simulation for trapezoidal electrode layout at 20mTorr ambient vacuum pressure for proof mass voltage of 0-40V. 72

Figure 3.14: The PLL controller with its main elements that are VCO, plate resonator, TIA, phase shifter, multiplier and controller used in this study. 74

Figure 3.15: Experimental setup for the system level temperature tests showing oscilloscope, frequency counter, signal generator used as VCO, power supply, vacuum pump and chamber, network analyzer and readout circuitry. 75

Figure 3.16: The PLL circuit shown in detail with main blocks that are , VCO, a controller, amplifier stages and a phase detector (multiplier). 76

Figure 3.17: The obtained results for natural frequency of mode (1,1) of the fabricated plate resonator and its temperature vs time. 77

Figure 3.18: Natural frequency of mode (1,1) of the fabricated plate resonator and its temperature vs time in larger temperature range. 78

Figure 3.19: Change of natural frequency of mode (1,1) with respect to temperature. 78

Figure 3.20: Test results of thermal effect on the natural frequency of mode (1,1) with analytical model and FE simulation for the temperature of 25-55°C. 79

Figure 3.21: Natural frequency vs Time for mode (1,1) plot obtained from the data acquired over 50000s with a sampling rate of 6.01 Hz for the sensor and PLL electronics together. 80

Figure 3.22: Allan variance plot for the natural frequency of mode (1,1). 80

Figure 3.23: Natural frequency of mode (2,0) – (0,2) of the fabricated plate resonator and its temperature vs time. 81

Figure 3.24: Natural frequency of mode (2,0) – (0,2) of the fabricated plate resonator and its temperature vs time in larger temperature range. 81

Figure 3.25: Change of natural frequency of mode (2,0) – (0,2) with respect to temperature. 82

Figure 3.26: Test results of thermal effect on the natural frequency of mode (2,0) – (0,2) with analytical model and FE simulation for the temperature of 25-66°C. 82

Figure 3.27: Natural frequency vs Time for mode (2,0) – (0,2) plot obtained from the data acquired over 40000s with a sampling rate of 200Hz for the sensor and PLL electronics together. 83

Figure 3.28: Allan variance plot for the natural frequency of mode (2,0) – (0,2). The Allan variance analysis is done to determine minimum detectable temperature. 84

LIST OF ABBREVIATIONS

ABBREVIATIONS

AC	Alternating Current
AlN	Aluminum Nitride
Au	Gold
BC	Boundary Conditions
CMOS	Complementary Metal Oxide Semiconductor
Cr	Chromium
DC	Direct Current
DETF	Double Ended Tuning Fork
DRIE	Deep Reactive Ion Etching
DUT	Device under Test
EOM	Equation of Motion
FBAR	Film Bulk Acoustic Resonator
FBD	Free Body Diagram
FEM	Finite Element Modelling
GaN	Gallium Nitride
GPS	Global Positioning System
HF	Hydrofluoric Acid
HPF	High Pass Filter
IC	Integrated Circuits
IR	Infrared Radiation
LDV	Laser Doppler Vibrometer
LPF	Low Pass Filter
MEMS	Micro-Electro-Mechanical Systems

METU	Middle East Technical University
Op-amp	Operational Amplifier
PLL	Phase Locked Loop
Q-factor	Quality Factor
RF	Radio Frequency
RTD	Resistor Temperature Detector
SAW	Surface Acoustic Wave
SEM	Scanning Electron Microscope
SNR	Signal to Noise Ratio
SOG	Silicon on Glass
SOI	Silicon on Insulator
SSE	Single Square Electrode
TE	Trapezoidal Electrode
TE Cooler	Thermoelectric Cooler
TIA	Trans-impedance Amplifier
VCO	Voltage Controlled Oscillator

CHAPTER 1

INTRODUCTION

Miniaturization of devices has continuously gained more importance since the development of microelectronics due to the advantages of smaller size, lower cost, and lower power consumption. Rising energy demand directed researchers to energy efficient solutions for most of the problems, boosting the effort spent on miniaturized devices. This revolution of miniaturization starts with the invention of transistors, as Richard P. Feynman states that there are plenty of room at the bottom [1].

Developments in the microfabrication of the integrated circuits (IC) have made fabrication of micro scale mechanical structures possible. The combination of microelectronics and micromechanics has resulted in a new research area, Micro-Electro-Mechanical-Systems (MEMS). The integration of mechanical and electrical structure on the same substrate has diversified the application areas of MEMS devices. Owing to their advantages of small size and mass, low power consumption, low cost of fabrication, and easy integration with other systems, MEMS devices are utilized in many industries including civil, automotive, military, and health.

The dimensions of MEMS devices range from sub-micron to several millimeters. The first MEMS device realized was a pressure sensor developed in 1980s [2]. Since then, various devices as sensors and actuators have been designed, fabricated and developed. Market share of the MEMS industry has an exponential increase since the year 2004 and it is predicted to increase exponentially in the upcoming years as well [3]. Although gyroscopes, accelerometers, pressure sensors and microphones has

dominated the field at the beginning, diversity of realized sensors, and actuators has increased. Among the variety of sensors, radio frequency (RF) MEMS devices and infrared (IR) detectors have a notable importance in MEMS industry [4]. In today’ s portable electronics, one key element of the circuits is the time sources they use. As an example, performances of global positioning system (GPS) are directly related with the synchronization of two clocks; the two clocks of GPS receiver and satellite. On the other hand, detecting lights with a wavelength outside the visible region is a fundamental need in most of the research areas such as space exploration. Also, light having a wavelength inside the infrared region is used to determine the temperature of the substance from which it comes.

This chapter introduces a literature survey of time keeping and IR detecting mechanisms. As a first section of the chapter, literature of the plate vibrations is presented. Then, the literature on MEMS resonators is summarized for time keeping devices. Since a resonator is analyzed as a temperature detecting device in this study, temperature detection is the focus of next section. Lastly, research objectives and organization of the thesis are presented.

1.1. Vibration of Plates and the Chladni Plate

Plates, with other fundamental machine elements like beams and shells, have been heavily investigated since the first machine introduced. Both static and dynamic behavior of the plates have been studied [5]. Although most of the effort has been spent on the behavior of the plates under static conditions, dynamic behavior has also been investigated for the past two centuries [6]. This dynamic behavior, most of the time, is also called vibration characteristics.

Several geometries and boundary conditions of the plate have been investigated [7, 8, 11, 13, 14]. Among those, square plates having four edges free to move is focus of this study which are called the “Chladni plate” named after, Chladni, first scientist who discovered the nodal patterns [15]. These nodal patterns are then called “Chladni figures”.

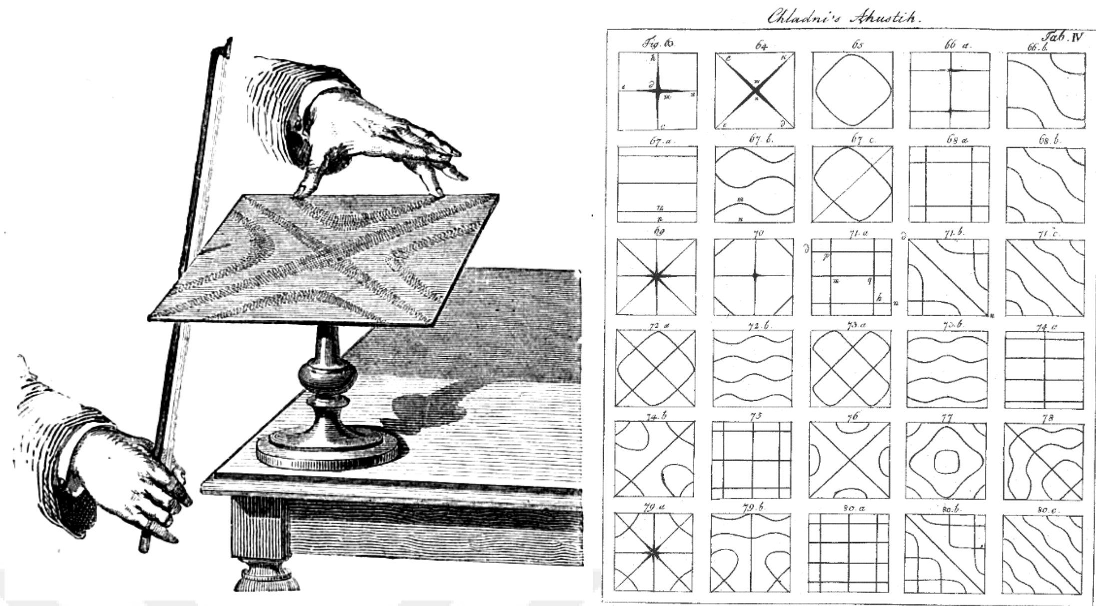

Figure 1.1: Excitation of the Chladni plate by bowing the plate from one of its free edges and mode shapes of the square plate known as Chladni figures [6, 15].

Transverse vibration of thin plate structures have been investigated for past two centuries. Although accurate estimation of the natural frequencies and the mode shapes were absent back then due to its complicated formulation, the shapes of those modes have been known. Ernst Chladni was the first scientist who visualized the mode shapes of plates with different geometries by bowing a plate as shown in Figure 1.1. He has demonstrated the nodal lines of transversely vibrating plate using sand particles and obtained the mode shapes of the various plate geometries which can be found at [15].

At [7], the closed form equation of fundamental natural frequency of plate with four free edges is presented, which is mostly used in the MEMS literature. Even though [7] presents a good approximation for the first natural frequency, higher modes are not available. A comprehensive study is done by Leissa covering rectangular and circular plates with several different boundary conditions [8]. Moreover, Leissa also studied the free vibration of rectangular plates [9]. Analytical solution of plate is not available for some edge conditions such as all edges are free to move. Researchers focused on approximate solutions to obtain a reasonable solution of the problem [10]. At [11],

solution of free-free beam is used in Rayleigh-Ritz energy method to solve vibration problem of the plate having four edges free [12].

1.2. MEMS Resonators

Performance of today's digital systems is highly dependent on the stability and accuracy of the time source they use. For time and frequency control, different types of resonators are utilized which can be used as either filter or oscillators. Crystal oscillators have been used widely in recent decades due to their excellent properties of high accuracy and stability [16]. However, besides these two key properties, small size, low power consumption and low cost are also very important requirements, especially in today's portable applications.

There are several types of frequency references such as oven stabilized crystal oscillators, Cesium atoms of atomic clocks, etc. Among those, ceramic filters, surface acoustic wave (SAW) filters, quartz crystals and recently the film bulk acoustic resonators (FBAR) are capable of having high Quality Factor (Q) for many applications like filtering, sensing and time keeping. However, they are all off-chip components meaning that they need to be interfaced with the rest of the electronics, which results in a considerable size and assembly cost [16]. In this manner, micro-electromechanical systems (MEMS) solutions satisfy the miniaturization and low power consumption without making any concession of Q-factor. One other advantage of MEMS devices is that they are usually compatible with CMOS (complementary metal-oxide-semiconductor) applications. Therefore, CMOS-MEMS resonators are widely viewed as an alternative for portable electronics [17, 18].

In the literature, there are several examples of MEMS resonators used in applications of time keeping, force sensing, temperature sensing, and IR detection with different type and physical shape of the vibrating body. For instance, body modes of the mechanical vibration of beams (tines) are utilized in double ended tuning fork (DETF) structures. With proper selection of mode with vacuum operation, it is possible to achieve quality factors as high as 65000 [19]. DETF sensors are also utilized to sense several physical phenomenon such as force, magnetic field, temperature, rotational

rate so on [20-23]. FBAR resonators are used as IR detectors in one of the studies [24] with a quality factor of 1407. In another bulk acoustic wave resonator application [25], a MEMS resonator is used as IR sensor. In addition to beams, mechanical vibrations of plate structures are also utilized as resonators. A MEMS plate resonator having (resonance frequency)×Q=3.4×10^{11} has also been reported for mass detection in liquids [26].

Most of the applications of plate resonator structures are in the form plates supported from four corner as in the case of [27] which has quality factor ranging from 800 to 1900. Corner support limits the number of available mode shapes due to anchor losses. If the corners are not on nodal lines, anchor losses will be higher, which decreases the Q-factor. Because of this reason, Chladni plate is selected in this work to enlarge the number of available mode shapes without changing the structure. The only example of a MEMS Chladni plate resonators in the literature is found at [28], which was targeting filter applications. In this study multiple plates are mechanically coupled, supporting each other from the corners. The reported quality factor of this structures exceeds 9000.

1.3. Temperature Detection

Among all the physical quantities, temperature is the one that is the most commonly measured. Due to reason that almost all material properties are functions of temperature, performance of any measurement device (whether it is mechanical or electrical) is subject to change with ambient temperature.

There has been great amount of work done to develop highly sensitive temperature sensors, which diversifies the types of these sensors. There are three main type of temperature detection method categorized according to geometric positions of the sensor and the substance of which its temperature will be measured. These categories are invasive, semi-invasive, and non-invasive temperature detection. In the case of invasive temperature detection, the sensor and the substance are in contact. On the other hand, the sensor and the substance are away from each other in the case of non-invasive temperature detection. In semi-invasive detection, the detecting element is in

contact with the substance; however, the reading is done remotely. Heat sensitive paints can be given as an example, where the color change of the paint is observed remotely.

Commonly used types of temperature sensors are thermocouples, resistor temperature detectors (RTD), thermistors, infrared (IR) sensors, semiconductors and thermometers. Among all, thermocouples are the most widely used ones, due to their low cost, high sensitivity, fast and linear response. Working range of thermocouples is the highest with some sacrifice in their accuracy. On the other hand, RTD measurements are more accurate and repeatable. As an example from the literature, a resolution of 6mK is achieved in one of the studies [29]. In another study, a resistor based temperature sensor with 2.8mK is demonstrated [30].

In this study, thermomechanical properties of silicon are utilized to detect the temperature of substances both in contact and contactless detectors, which are mostly called temperature sensors and IR detectors, respectively. There is a distinct difference between the temperature sensors and IR detectors, which is the means of thermal heat transfer. Temperature sensors heat up or cool down with the heat transferred from or into the detecting body in the form of convection and/or conduction. On the other hand, heat is transferred from the body to the IR detector by means of radiation. Both cases are visualized in *Figure 1.2.*

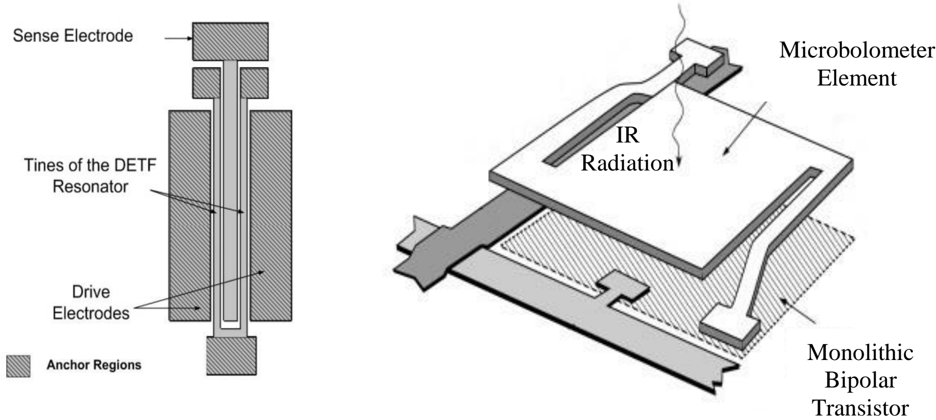

Figure 1.2: (a) Invasive type temperature sensor in contact with the substrate, (b) Noninvasive type temperature sensor, i.e., IR detector.

In Figure 1.2 (a), a temperature sensor utilizing a double ended tuning fork (DETF) is shown. Sensing element is a thin double ended beam [31].The temperature of the substance in contact with the detector is measured by means of tracking one of the physical properties of the material, which should be a function of temperature [32]. Although the working principle of the IR detector shown in Figure 1.2 (b) is very similar to the one in Figure 1.2 (a), the temperature of the detector changes due to incident radiation onto the surface area of the detector.

Scientists have developed many methods to detect infrared radiation since the first experiment done by Herschel (1800s) with thermometers [33]. In one of those experiments, Langley has combined two platinum tape as the legs of Wheatstone bridge in 1880 [34]. He has continued to develop his bolometer for about 20 years and managed to detect heat of a cow from a quarter mile distance [35].

IR detectors have been categorized into two main subjects; photon detectors and thermal detectors. Photon detectors have very high SNR (signal to noise ratio) and fast response; however, they need cryogenic cooling. On the other hand, thermal detectors eliminate the need for cryogenic cooling. Thus, they have been widely studied for three decades. As an example, a thermal detector having 650μs thermal time constant and noise equivalent power of $7nW/Hz^{1/2}$ has been demonstrated in [24]. In another study, a thermal detector having 63μs thermal time constant and 520Hz/μW sensitivity has been reported in [36]. In one of the studies which is compatible with CMOS techniques, very high electromechanical performance is reported with a quality factor of 1062, electromechanical coupling coefficient of 1.62% and noise equivalent power of 2.4 $nW/Hz^{1/2}$ [37]. In a study, the fabricated prototype AlN MEMS resonator has a reported sensitivity of 310Hz/ μW, 1.3ms thermal time constant, $3.5nW/Hz^{1/2}$ and power consumption of 2.3mW [38], showing that resonators are promising candidates for uncooled IR detector applications. There are also examples of studies utilizing GaN (gallium nitride) resonators, having greater sensitivity and SNR than the other type of uncooled IR detectors [39].

Apart from these, resonators are also used as temperature sensors [40]. The advantages of high sensitivity, high dynamic range, low mechanical compliance and digital output

of DETFs are utilized for the purpose of temperature compensation of a capacitive accelerometer in one of the studies. The reported resolution is 1.1mK [41]. There are also examples of semi assisted and fully MEMS resonators used as temperature detectors. For a MEMS semi assisted temperature sensor, reported resolution is 20µK [42]. It is also reported that, a dual MEMS resonator temperature to digital converter have 40µK resolution [43].

1.4. Research Objectives and Thesis Organization

With the increasing demand for energy, decreasing cost and ease of integration with other systems, MEMS become the focus of most researchers. It is not hard to predict that application areas of MEMS will continue to increase in the near future [3]. One of these application areas is thermal detectors on which world wide effort has been spent to develop high sensitive detectors [44]. This thesis proposes an application of resonators being used as thermal detectors. The designed and fabricated thermal detectors consist of a micro plate and underneath electrodes. Plate material is single crystalline silicon having physical properties susceptible to change with temperature. The electrodes are used in driving and sensing purposes. The main objectives of this research are:

1. Development of a micromachined thermal sensor utilizing micro plate vibrations. Thermal detecting element should utilize a resonator to take the advantages such as high sensitivity, high dynamic range, low power consumptions.

2. Derivation of the analytical electromechanical model of the silicon plate with four edges free to move under periodic loading for first and higher modes. Most of the work done in the literature for dynamic behavior of micro plate uses a well-known closed form equation for the first natural frequency for non-silicon materials; however, higher modes together with the first mode should be modelled for the structural material silicon.

3. Derivation of the analytical thermo-electro-mechanical model of the designed thermal sensor. The thermo-electro-mechanical model should include electrostatic actuation and thermal effects on the mechanical vibration.

4. Finite element simulations of the mechanical, electro-mechanical, and thermo-electro-mechanical models. The micro plate sits on top of a post being the support; therefore, effect of the post should be considered in the FE simulations. The analytical model and FE simulations should be compared in terms of natural frequencies, mode shapes, electrostatic effects and thermal effects.

5. Characterization and performance tests of the fabricated micro plate resonant based temperature sensors to verify derived analytical models. Characterization tests should compose of frequency response and system level temperature tests. Performance tests should cover thermal sensitivity, range and bias instability. In the characterization tests, a closed loop excitation system should be implemented to keep the system at resonance while counting the frequency, which is directly related to the temperature change of the plate structure.

The organization of the thesis is given as follows:

Chapter 2 presents the design and modelling of resonant MEMS square plate temperature sensor. The proposed application is given in detail before the modelling subsection. This chapter contains fundamentals of plate vibration, equation of motion (EOM) of the transversely vibrating plate, solution method for the EOM, electrostatic driving and actuation, analytical model of the electrostatic softening and thermal effects on the natural frequencies of the plate. As a last subsection, finite element (FE) simulations are presented. In the FE simulation section, transverse vibration of the plate, electromechanical effect and thermo-electro-mechanical model is simulated. Results of analytical models and FE simulations are also compared.

Chapter 3 presents the fabrication flow and characterization experiment results for the resonant MEMS square plate temperature sensor. In the first section, the micro

fabrication steps are explained and the flow is given. Then, experimental test setups for each test are explained. For the frequency response tests, test results are compared with the electromechanical model and corresponding FE simulation. For the system level tests, the results are compared with the thermo-electro-mechanical analytical mode and corresponding FE simulations.

As the final chapter, Chapter 4 presents the conclusions derived from the results obtained in this research and recommendations for the future work.

CHAPTER 2

DESIGN AND MODELLING OF RESONANT MEMS PLATE TEMPERATURE SENSOR

In this chapter, the design and modeling of resonant a MEMS plate temperature sensor is presented. For micromachined devices, the modeling of the interaction between electrical and mechanical domains requires a multidisciplinary study. In this chapter, electromechanical study is presented with the thermal effect added. In Section 2.1, basic concepts related with the plate vibration theory are introduced. Definitions of mode shape, nodal line, natural frequency and naming of the Chladni figures are given. In addition to design parameters and physical structure of the sensor, the proposed application of the resonant MEMS plate as a temperature sensor is explained in detail in Section 2.2. As for Section 2.3, analytical model of plate vibrations are presented starting from EOM of transverse vibration of plate. Solution of EOM with Rayleigh - Ritz method is explained in detail as a subsection. Electrostatic actuation and sensing are formulated. Electrostatic softening effects on the natural frequencies of mode shapes are included. Lastly, in this section, thermal effects are added to the derived analytical model. Then, FEM simulations are given in Section 2.4 with the corresponding sequence in the analytical model section, that is transverse vibration of MEMS plate, electrostatic effect and thermal effect. As a last section, Section 2.5 gives the summary of the chapter in a nutshell.

2.1. Basic Concepts in Plate Vibration Theory

A dynamic system is defined as the system in which single or multiple aspects change in time. Vibration, on the other hand, occurs in the presence of elements in the dynamic system having mass and elasticity. Vibration, by definition, is the oscillation around equilibrium point. In this chapter, the mechanical vibration of a micro plate is analyzed and modelled.

Natural frequency, frequency of oscillation in free and harmonic vibration, is determined solely by system parameters. Therefore, it is an invariant property of the system [45]. Most of the time, fundamental frequency refers to the lowest natural frequency of the system. Undamped natural frequencies are the obtained eigenvalues from the solution of eigenvalue problem. Mode shape; on the other hand, is the shape which the vibrating body takes when it is vibrated with corresponding natural frequency. Mode shapes are the eigenvectors in the solution of eigenvalue problem.

As the last basic concept, nodal points are defined as motionless points in the body of the vibrating structure. Sequencing the mode shape is related with the nodal points. Mode shapes are named with the number of half sine waves in the vibrating body which equals to one minus the number of nodal points. If the ends of the structure are supported, they are also counted as nodal points. It is necessary to systematically name mode shapes of a plate given in Figure 2.1. In the literature, mode shapes of a plate are named with the number of nodal lines parallel to x and y axes shown in Figure 2.2. Number of nodal lines are m and n parallel to x and y axes, respectively. As described above, this number includes the edge if the edge is supported. Nodal lines are approximately parallel to one of the edges if the plate is rectangular; however, they may not be parallel to edges if the plate is square. Those non-parallel nodal patterns (seen in Figure 2.1) were first observed by the 18th century researcher Chladni [15]. For the square plates, if one of m and n is odd and the other is even, normal modes of vibration is (m , n) type. For the other case, that is, both m and n are even or odd, normal mode shapes are of the type $(m,n)+(n,m)$ or $(m,n)-(n,m)$. The details of the naming are not given here as they can be found in [8].

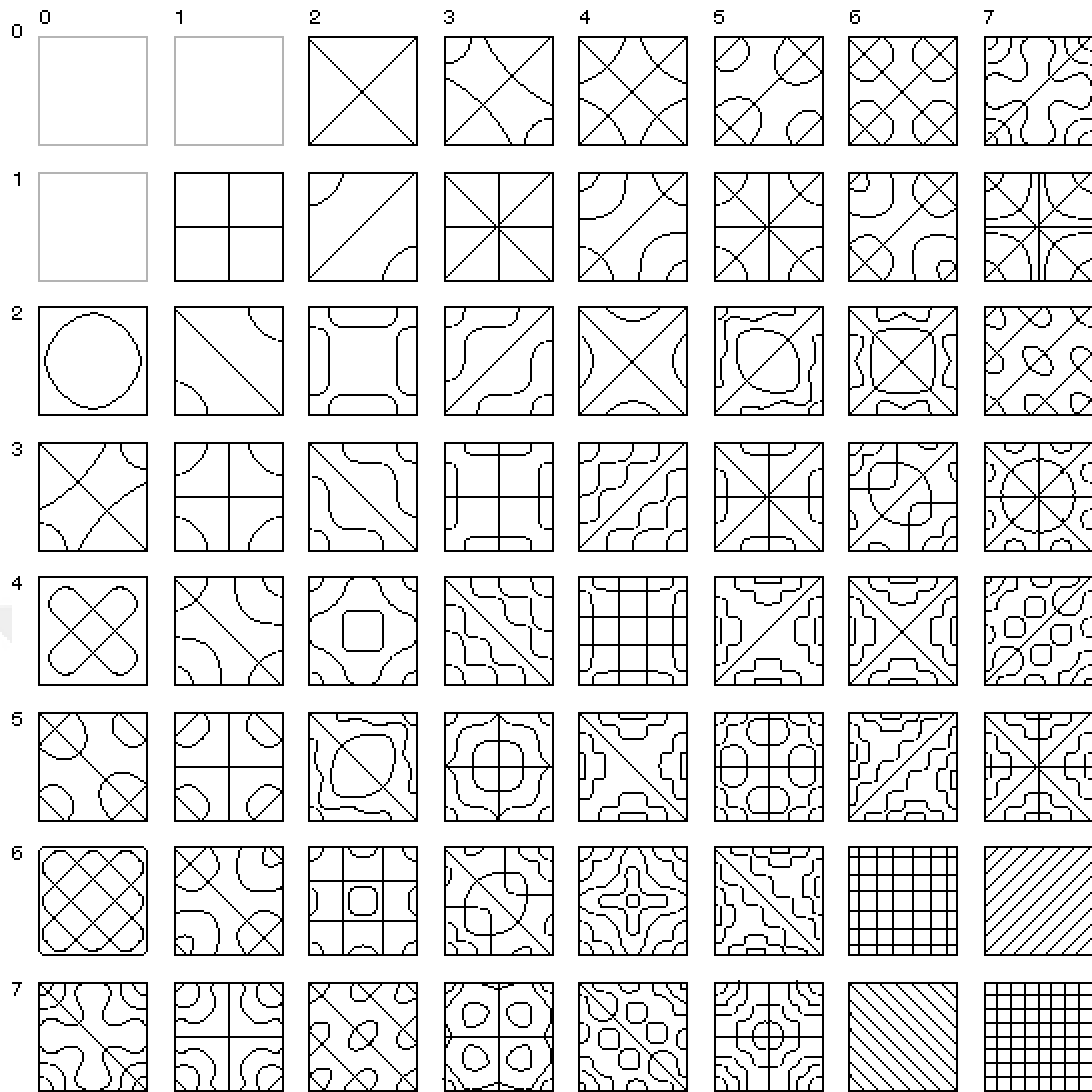

Figure 2.1: Some of the Chladni plate mode shapes.

Plates can be supported at any point; however, there are several boundary conditions on which a lot of effort has been made. As mentioned before, plates are used as structural elements; therefore, supporting from one or more edges is widely studied. To define the supported edges, the initial of the support type is abbreviated. For example, the plate having one of the edges clamped and other three edges free to move is called as CFFF (Clamped-Free-Free-Free) plate. Another example is CSCF plate, which is clamped from two opposite edges, one of the edges is simply supported and the other edge is free to move. In the scope of this thesis study, FFFF plates are analyzed.

2.2. Resonant MEMS Plate Temperature Sensor

Temperature detection of a subject has so far been crucial in most engineering problems. As explained in Chapter 1, some of the applications are in manufacturing, global warming investigations, customer electronics, health monitoring, research and civil and military applications. Hence, temperature detection of a subject has been a one of the most focused area in the MEMS sensing applications.

As mentioned in Section 2.1, for a structural system having mass and stiffness, natural frequency is a parameter of this system. Natural frequency, by definition, is the function of other system parameters which are mass, stiffness and damping. Most of the mechanical properties affecting the vibration characteristics of a structure such as modulus of elasticity, Poisson's ratio, dimensions are subjected to change with temperature. In other words, natural frequency of the vibrating body is function of temperature through different mechanisms. In this thesis study, the temperature is measured using silicon MEMS plate vibrations. The designed thermal sensor is type of invasive temperature detector, i.e., the resonant MEMS plate temperature sensor measures the temperature of a substance which is in contact with the sensor. Change in temperature also causes changes in the frequency of oscillations of the plate. This frequency change can be tracked with a closed loop controller as amplitude detection, phase lock loop (PLL) etc. to detect the temperature change of the vibrating plate.

2.2.1. Physical Structure of the MEMS Plate Resonator

The structure of the resonator proposed in this thesis study is composed of single crystal silicon plate, glass post (stem) and gold electrodes beneath the plate and over glass substrate. The square plate sits on top of the post as visualized in Figure 2.2 (a).

In Figure 2.2 (a), Cartesian coordinate system used in analytical modelling is shown. a is the side length in the direction of both x and y axes. The electrostatic gap between plate and electrodes is given as g.

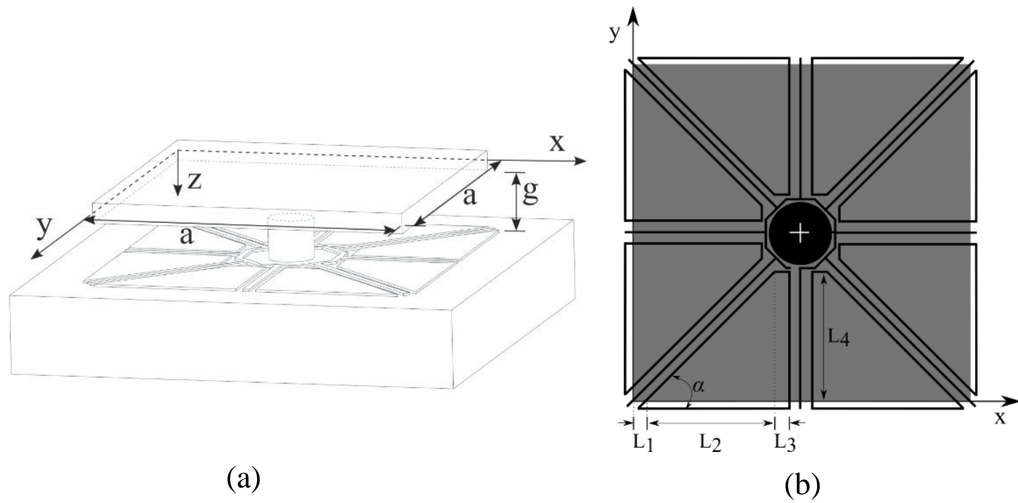

Figure 2.2: (a) Schematic of the plate supported at the geometric center with four edges free to move: The coordinate system and geometric dimensions used in modelling are shown. (b) Electrode layouts in the proposed MEMS plate resonator and orientation of electrodes with respect to plate which is shown in dark gray.

Among the several actuating and sensing principles in the literature for MEMS devices, capacitive actuation and sensing principle are utilized in this study due to the availability of experimental setups in the laboratory and their well-defined mathematical model. The capacitive plates are the resonating plate itself and the electrodes on top of the glass substrate. Trapezoid shaped electrodes are shown in Figure 2.2 (b). In the figure, L_1 is the distance from the origin to the point where trapezoid electrode starts to be beneath the plate, L_3 is the short side length, L_4 is height of the trapezoidal electrode. Long side length of the trapezoidal electrode equals to summation of L_1, L_2, and L_3.

2.2.2. Geometric Dimensions and Specifications of the Design

The proposed micro plate resonator is a square plate as it can also have rectangular or circular shape. However, as explained in Chapter 1, square plates supported at their geometric center, Chladni plates, have distinctive mode shapes. Almost all the mode shapes shown in Figure 2.1 have a nodal point at the geometric center. One should

notice that for a two dimensional structure, there are nodal lines instead of nodal points. There are several advantages of selecting square geometry and supporting the square plate at its geometric center. They can be summarized as follow:

1. One of the key concerns in supporting the vibrating structures in MEMS applications is to minimize the anchor loss. Supporting point is selected as the intersection of the nodal lines, which minimizes shear and normal stresses on the post and mitigates coupling to the structure.

2. Decreasing anchor loses improves the quality factor, Q-factor, of the resonator. Quality factor of a resonator is one of the most significant parameter for ranking the performance of the resonators.

3. The effect of excitation of the base on the mode shapes is mitigated with the same reasoning that no strains are coupled between the plate and post.

4. This advantage is specific to this study. The analytical model of transverse vibration of the plate is derived using free-free beam solutions. Since the plate is fixed at one of the nodal points of the beam, the effect of post on the frequencies is suppressed, which simplifies the analytical model.

5. To investigate large number of mode shapes without modifying the resonator, square geometry is selected and supported at the geometric center. The number of nodal lines may pass through center contrary to rectangular shape, which allows for at most two nodal lines passing through center.

6. Modes-of-interest in this study have large deflections compared to higher order modes, which increases both the signal-to-noise ratio for the detection electrodes and generated force for the driving electrodes.

7. In spite of the complexities of MEMS fabrication processes, designing such a robust geometry enables to produce simpler and high yielding fabrication process flow.

In addition, for the electrode layout shown in Figure 2.2, a DC biased applied wire is placed between all the AC electrodes without forming a closed loop. Proof mass voltage is applied to transversely vibrating plate with a wire placed between all electrodes. A DC bias is applied as proof mass voltage and it prevents the interaction of nearby AC signals created or applied to the electrodes. However, one should notice that, this wire does not form a close loop in order not to create a current picked up from electromagnetic induction. Another comment on the design is that trapezoidal electrodes are bigger than the plate. With the fringing field created, driving and sensing electrodes create higher forces and signal-to-noise ratio, respectively.

The summary of the geometric dimensions, material parameters and some of the test parameters used in this study are given in Table 2.1. Some of the parameters used in tests are not given in this table as they are subject to change in each test. Hence, they are given in the corresponding sections.

Table 2.1: Summary of the geometric dimensions, the material parameters for the plate resonator and some of the test parameters used in this study. See Figure 2.2 for variable definitions.

Quantity	**Symbol**	**Value**
Side length in x and y directions	a	1400 μm
Plate thickness	h	35 μm
Capacitive gap (Plate handle length)	g	8.73 μm
Trapezoidal angle of the electrodes	α	45°
Side length of trapezoidal electrode outside the plate	L_1	50 μm
Rest of the long side length of trapezoidal electrode underneath the plate	L_2	450 μm
Short side length of trapezoidal electrode beneath the plate	L_3	172 μm
Height of the trapezoidal electrode	L_4	450 μm

Young's modulus of (111) Si [20]	E	$170\ GPa$
Poisson's ratio of (111) Si [46]	v	0.262
Mass density of Si [20]	ρ	$2330\ kg/m^3$
Permittivity of the dielectric (vacuum)	ε_0	$8.85\ x10^{-12}\ F/m$
Thermal coefficient of expansion of silicon [47]	α_{Si}	$2.6\times10^{-6}/K$
Thermal expansion coefficient of silicon dioxide [48]	α_{SiO_2}	$0.5\times10^{-6}/K$
Thermal coefficient of Young's Modulus of silicon [49]	α_E	$-60\times10^{-6}/K$
Proof mass voltage	V_{PM}	$15\ V$
Feedback resistance in read out trans impedance amplifier	R_{fb}	1 MΩ
Ambient room temperature	T_0	$25\,^oC$

2.3. Modelling of Resonant MEMS Plate Temperature Sensor

Plates are, by definition, the structural elements with one of the dimensions, generally called thickness, being much smaller than the other two dimensions. Oscillations in the direction of thickness are called transverse vibration of plates. Deformations are measured from midplane in the direction of normal vector of midplane. Midplane is defined as the plane parallel to faces of plate dividing thickness into two halves. In the literature, plates are classified in terms of thin and thick plates; however, only thin plates are analyzed in the scope of this thesis study.

The problem in hand is composed of transverse vibration of plate, called mechanical part, electrostatic driving and actuating part, called electrostatic part and thermal effect on those two parts. Therefore, analytical modelling is divided into three parts to analyze all of them. The results of the analytical model are compared with the Finite Element Model (FEM) in this section and will be compared with test results in the next

chapter. FE models are also divided into three parts to be consistent with analytical modelling.

2.3.1. Analytical Model of MEMS Square Plate Vibrations

For the analytical model, equation of motion (EOM) of a transversely vibrating plate can be obtained via Equilibrium Approach or Variational Approach. In both approach, there are several assumptions given as [14]:

1. It is a thin plate that is thickness is very small compared to other two dimensions and deflection of the mid surface is small when compared to thickness.

2. The midplane remains unstrained upon the application of bending load also called as neutral surface.

3. Plane sections which are initially normal to midplane remain plane upon the application of bending load. This implies that the vertical shear strains are negligible. In other words, plate resists lateral and in plane loads by bending, not trough block like compression or tension in the thickness direction.

4. The effect of transverse shear deformations and rotary inertia are neglected.

5. Transverse normal strain under transverse loading can be neglected. Transverse normal stresses are small; hence, they can be neglected compared to other stress components.

6. Throughout the study, material silicon is assumed to be isotropic and has uniform thickness.

With this assumptions, small deflection theory of thin plates which is also called as *classical plate theory* or *Kirchhoff's theory* is built upon the similar assumptions used in thin beam theory, also known as *Euler-Bernoulli beam theory*.

2.3.1.1. Equation of Motion: Equilibrium Approach

For a given plate, stresses and coordinate system used in driving EOM is given in Figure 2.3. As seen, mid plane of the plate coincides with the xy plane of the coordinate system. Transverse deflection denoted as $w(x, y, z, t)$ is function of spatial coordinates and time.

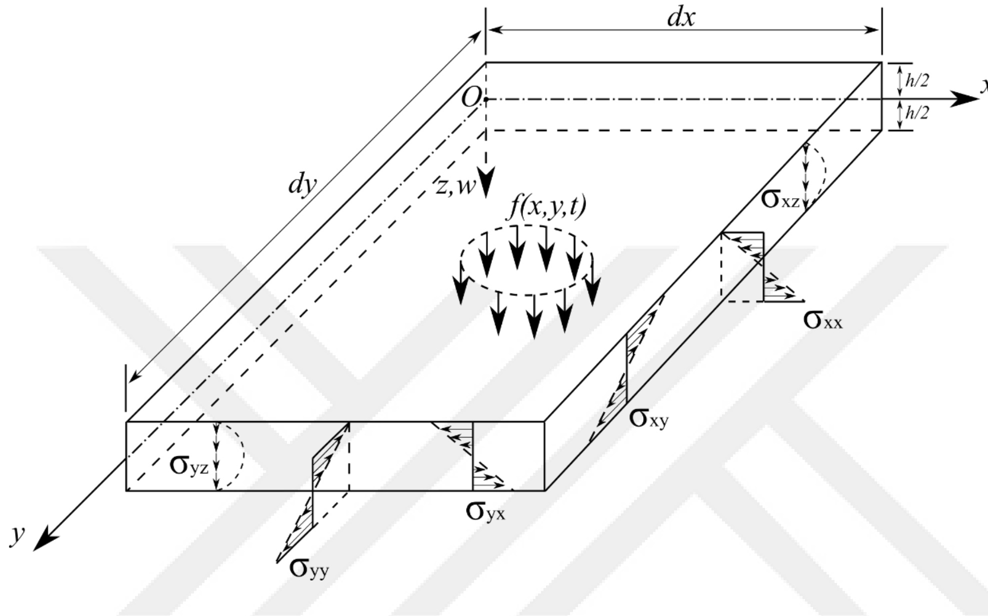

Figure 2.3: Induced stresses on a differential plate element under de application of bending load and coordinate system used in the modelling.

In plate theory, it is convenient to work with stress resultant along on the mid surface edges instead of stresses on the edges. For the given plate under bending loading (transverse loads and bending), direct stresses in z direction, σ_{zz} , are usually neglected, which can be inferred from the fifth assumption given above. Since only flexural (bending) deformations are considered, there is no net force in the directions of x and y axes. Stress resultants in x and y directions are written as:

$$\int_{-h/2}^{h/2} \sigma_{xx} dz = 0$$
$$\int_{-h/2}^{h/2} \sigma_{yy} dz = 0 \qquad (2.1)$$

As in the beam theory, stresses vary linearly and parabolic as shown in Figure 2.3. Those stresses are used to get following force and moment resultants.

$$
\begin{gathered}
M_x = \int_{-h/2}^{h/2} \sigma_{xx} z dz \qquad and \qquad M_y = \int_{-h/2}^{h/2} \sigma_{yy} z dz \\
M_{xy} = \int_{-h/2}^{h/2} \sigma_{xy} z dz = M_{yx} \\
Q_x = \int_{-h/2}^{h/2} \sigma_{xx} dz \qquad and \qquad Q_y = \int_{-h/2}^{h/2} \sigma_{yy} dz
\end{gathered}
\tag{2.2}
$$

Stress resultants in all edges given Equation 2.2. Using these equations, Figure 2.3 is converted to a free body diagram (FBD) of differential element and presented Figure 2.4.

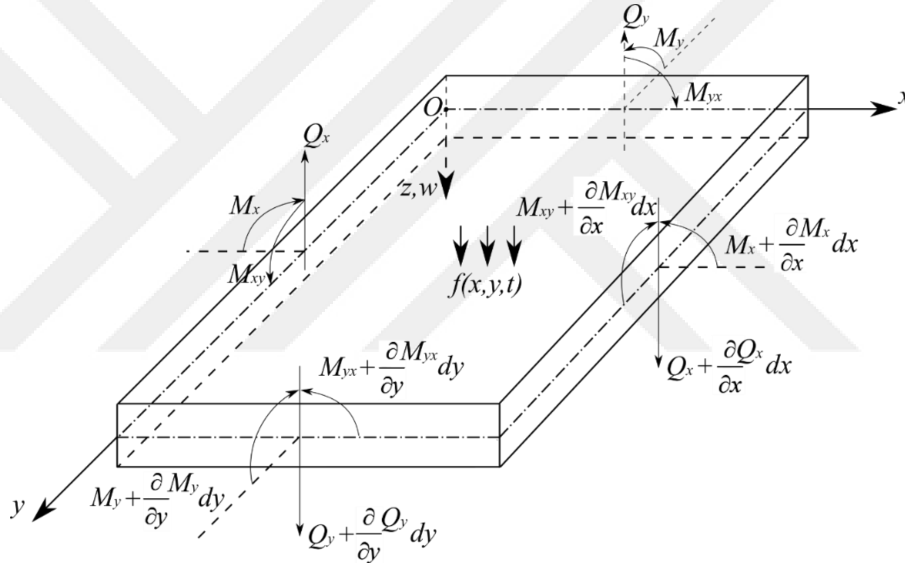

Figure 2.4: Free body diagram of a differential plate element. Force and moment resultants are shown on the four edges of mid plane which coincides with the xy plane of coordinate system.

Since the FBD of the plate given as force and moment resultant, one should notice that given $f(x, y, t)$ is the intensity of the externally distributed force. Dynamic equilibrium equations are written to derive EOM. Writing force balance equation in z direction results as follow.

$$\left(Q_x+\frac{\partial Q_x}{\partial x}dx\right)dy+\left(Q_y+\frac{\partial Q_y}{\partial y}dy\right)dx$$
$$+f(x,y,t)dxdy-Q_xdy-Q_ydx=\rho hdxdy\frac{\partial^2 w}{\partial t^2} \tag{2.3}$$

Force equilibrium in z direction is simplified as:

$$\frac{\partial Q_x}{\partial x}+\frac{\partial Q_y}{\partial y}+f(x,y,t)=\rho h\frac{\partial^2 w}{\partial t^2} \tag{2.4}$$

Equilibrium of moments in x direction is given as:

$$\left(Q_y+\frac{\partial Q_y}{\partial y}dy\right)dxdy=\left(M_y+\frac{\partial M_y}{\partial y}dy\right)dx+\left(M_{xy}+\frac{\partial M_{xy}}{\partial x}dx\right)dy-M_ydx-M_{xy}dy$$
$$-f(x,y,t)dxdy\frac{dy}{2}+\left(Q_x+\frac{\partial Q_x}{\partial x}dx\right)dy\frac{dy}{2}-Q_xdy\frac{dy}{2} \tag{2.5}$$

Cancelling the terms having opposite signs and neglecting the higher order terms, Equation 2.5 is simplified in Equation 2.6.

$$Q_y=\frac{\partial M_y}{\partial y}+\frac{\partial M_{xy}}{\partial x} \tag{2.6}$$

Similarly, moment equilibrium in y direction is given as:

$$Q_x=\frac{\partial M_x}{\partial x}+\frac{\partial M_{yx}}{\partial y} \tag{2.7}$$

At this point, strain - displacement relations which can be found in [5] are used. Bending deformation of a differential element is:

$$u = -z\frac{\partial w}{\partial x}$$
$$v = -z\frac{\partial w}{\partial y} \tag{2.8}$$

From the small deformations theory, linear strain - displacement relations are given as:

$$\varepsilon_{xx} = \frac{\partial u}{\partial x}, \qquad \varepsilon_{yy} = \frac{\partial v}{\partial x}, \qquad \varepsilon_{xy} = \frac{\partial u}{\partial y} + \frac{\partial v}{\partial x} \tag{2.9}$$

Inserting Equation 2.8 into Equation 2.9 gives:

$$\varepsilon_{xx} = -z\frac{\partial^2 w}{\partial x^2}, \ \varepsilon_{yy} = -z\frac{\partial^2 w}{\partial y^2}, \ \varepsilon_{xx} = -2z\frac{\partial^2 w}{\partial x \partial y} \tag{2.10}$$

The state of the stress in the plane is assume to be plane stress. Stress - strain relations are defined by the well-known relation, Hooke' s Law as:

$$\sigma_{xx} = \frac{E}{1-v^2}\varepsilon_{xx} + \frac{vE}{1-v^2}\varepsilon_{yy}$$
$$\sigma_{yy} = \frac{E}{1-v^2}\varepsilon_{yy} + \frac{vE}{1-v^2}\varepsilon_{xx} \tag{2.11}$$
$$\sigma_{xy} = \frac{E}{2(1+v)}\varepsilon_{xy}$$

Inserting strain – stress displacement and stress – strain relations into Equation 2.2 and defining flexural rigidity of the plate as in Equation 2.12 result in the force and moment resultants as a function of displacements given in Equation 2.13.

$$D = \frac{Eh^3}{12(1-v^2)} \tag{2.12}$$

where h is the plate thickness, E is the Young' s modulus and v is the Poisson' s ratio. Force and moment resultants are;

$$M_x = -D\left(\frac{\partial^2 w}{\partial x^2} + \nu\frac{\partial^2 w}{\partial y^2}\right)$$

$$M_y = -D\left(\frac{\partial^2 w}{\partial y^2} + \nu\frac{\partial^2 w}{\partial x^2}\right)$$

$$M_{xy} = -D(1-\nu)\frac{\partial^2 w}{\partial x \partial y} \quad (2.13)$$

$$Q_x = -D\frac{\partial}{\partial x}\left(\frac{\partial^2 w}{\partial x^2} + \frac{\partial^2 w}{\partial y^2}\right)$$

$$Q_y = -D\frac{\partial}{\partial y}\left(\frac{\partial^2 w}{\partial x^2} + \frac{\partial^2 w}{\partial y^2}\right)$$

To get EOM of the plate, force and moment resultants and flexural rigidity are introduced in the Equation 2.4.

$$D\left(\frac{\partial^4 w}{\partial x^4} + 2\frac{\partial^2 w}{\partial x \partial y} + \frac{\partial^4 w}{\partial y^4}\right) + \rho h\frac{\partial^2 w}{\partial t^2} = f(x, y, t) \quad (2.14)$$

where ρ is the density of the plate material. Biharmonic operator is defined as:

$$\nabla^4 = \frac{\partial^4}{\partial x^4} + 2\frac{\partial^2}{\partial x \partial y} + \frac{\partial^4}{\partial y^4} \quad (2.15)$$

Then, most general form of EOM of a transversely vibrating thin plate is found in Equation 2.16.

$$D\nabla^4 w + \rho h\frac{\partial^2 w}{\partial t^2} = f(x, y, t) \quad (2.16)$$

2.3.1.2. Equation of Motion: Variational Approach

This method also known as *Hamilton Principle* utilizes potential and kinetic energy equations to derive EOM, which helps understanding of the method described in section 2.3.1.3. Due assumptions done previously, stress state is assumed to be plane

stress. Stresses given in Equation 2.11 can be written as a function of displacement instead of strains with the given strain – displacement equations given in Equation 2.10.

$$\sigma_{xx} = -\frac{Ez}{1-\nu^2}\left(\frac{\partial^2 w}{\partial x^2} + \nu\frac{\partial^2 w}{\partial y^2}\right)$$
$$\sigma_{yy} = -\frac{Ez}{1-\nu^2}\left(\frac{\partial^2 w}{\partial y^2} + \nu\frac{\partial^2 w}{\partial x^2}\right) \quad (2.17)$$
$$\sigma_{xy} = -\frac{Ez}{(1+\nu)}\frac{\partial^2 w}{\partial x \partial y}$$

Strain energy density is defined as in Equation 2.18 as it can be found in [50].

$$V_0 = \frac{1}{2}\left(\sigma_{xx}\varepsilon_{xx} + \sigma_{yy}\varepsilon_{yy} + \sigma_{xy}\varepsilon_{xy}\right) \quad (2.18)$$

Inserting Equations 2.10 and 2.17 into Equation 2.18 gives:

$$V_0 = \frac{Ez^2}{2(1-\nu^2)}\left[\left(\frac{\partial^2 w}{\partial x^2}\right)^2 + \left(\frac{\partial^2 w}{\partial y^2}\right)^2 + 2\frac{\partial^2 w}{\partial x^2}\frac{\partial^2 w}{\partial y^2} + 2(1-\nu)\left(\frac{\partial^2 w}{\partial x \partial y}\right)^2\right] \quad (2.19)$$

Integration of strain energy over volume of the plate gives the total potential energy of the plate as given in Equation 2.20.

$$V = \iiint_V V_0 dV = \iint_A dA \int_{-h/2}^{h/2} V_0 dV$$
$$= \frac{E}{2(1-\nu^2)}\iint_A \left[\left(\frac{\partial^2 w}{\partial x^2}\right)^2 + \left(\frac{\partial^2 w}{\partial y^2}\right)^2 + 2\frac{\partial^2 w}{\partial x^2}\frac{\partial^2 w}{\partial y^2} + 2(1-\nu)\left(\frac{\partial^2 w}{\partial x \partial y}\right)^2\right] dA \int_{-h/2}^{h/2} z^2 dz \quad (2.20)$$

Note that

$$\int_{-h/2}^{h/2} z^2 dz = \frac{h^3}{12} \quad (2.21)$$

From the definition of flexural rigidity of the plate;

$$\frac{E}{2\left(1-\nu^2\right)}\int_{-h/2}^{h/2} z^2 dz = \frac{D}{2} \tag{2.22}$$

Then the potential equation becomes

$$V = \frac{D}{2}\iint_A \left\{\left(\frac{\partial^2 w}{\partial x^2}+\frac{\partial^2 w}{\partial y^2}\right)^2 - 2(1-\nu)\left[\frac{\partial^2 w}{\partial x^2}\frac{\partial^2 w}{\partial y^2}-\left(\frac{\partial^2 w}{\partial x \partial y}\right)^2\right]\right\} dxdy \tag{2.23}$$

With the same assumptions, kinetic energy equation is written as:

$$T = \frac{\rho h}{2}\iint_A \left(\frac{\partial w}{\partial t}\right)^2 dxdy \tag{2.24}$$

Lastly, the work done on the plate by the external force is calculated as below.

$$W = \iint_A f\left(x, y, t\right) w dxdy \tag{2.25}$$

Lagrange is defined as:

$$L = V - T - W \tag{2.26}$$

Applying Hamilton' s principle to Lagrange given above gives the EOM of the transversely vibrating plate.

$$\delta\int_{t_1}^{t_2} L dt = \delta\int_{t_1}^{t_2}\left(V - T - W\right) dt = 0 \tag{2.27}$$

Substituting energy equations given in Equation 2.23, 2.24 and 2.25 into Equation 2.27 to get:

$$\delta\int_{t_1}^{t_2}\left(\begin{array}{l}\frac{D}{2}\iint_A\left\{\left(\frac{\partial^2 w}{\partial x^2}+\frac{\partial^2 w}{\partial y^2}\right)^2-2(1-\nu)\left[\frac{\partial^2 w}{\partial x^2}\frac{\partial^2 w}{\partial y^2}-\left(\frac{\partial^2 w}{\partial x\partial y}\right)^2\right]\right\}dxdy\\ -\frac{\rho h}{2}\iint_A\left(\frac{\partial w}{\partial t}\right)^2 dxdy-\iint_A f(x,y,t)wdxdy\end{array}\right)dt=0 \quad (2.28)$$

Harmonic operator is defined as:

$$\nabla^2=\frac{\partial^2}{\partial x^2}+\frac{\partial^2}{\partial y^2} \quad (2.29)$$

Equation 2.28 is divided into four simpler integrations and solved in detail in [50]. As the solution of this complicated integration, EOM and boundary conditions (BC) are obtained. In the Equation 2.30, C denotes boundary of the plate, n indicates outward drawn normal to the boundary.

$$\int_{t_1}^{t_2}\left\{\begin{array}{l}\iint_A\left(D\nabla^4 w+\rho h\frac{\partial^2 w}{\partial t^2}-f(x,y,t)\right)\delta w dxdy\\ +D\int_C\left[\nabla^2 w-(1-\nu)\frac{\partial}{\partial s}\left(\frac{\partial^2 w}{\partial x^2}\sin^2\theta-2\frac{\partial^2 w}{\partial x\partial y}\sin\theta\cos\theta+\frac{\partial^2 w}{\partial y^2}\cos^2\theta\right)\right]\frac{\partial\delta w}{\partial n}dC\\ -D\int_C\left[\frac{\partial\nabla^2 w}{\partial n}-(1-\nu)\frac{\partial}{\partial s}\left[\left(\frac{\partial^2 w}{\partial x^2}-\frac{\partial^2 w}{\partial y^2}\right)\cos\theta\sin\theta+\frac{\partial^2 w}{\partial x\partial y}\left(\sin^2\theta-\cos^2\theta\right)\right]\right]\delta w dC\end{array}\right\}dt=0 \quad (2.30)$$

where s is tangent line to the boundary and the angle θ is angle between the outward normal and x axis. Each term inside the integral in Equation 2.30 should be zero, since δw is arbitrary. Then EQM and BCs are obtained by equation each of them to zero, separately.

$$D\nabla^4 w+\rho h\frac{\partial^2 w}{\partial t^2}-f(x,y,t)=0$$

$$\left[\nabla^2 w-(1-\nu)\frac{\partial}{\partial s}\left(\frac{\partial^2 w}{\partial x^2}\sin^2\theta-2\frac{\partial^2 w}{\partial x\partial y}\sin\theta\cos\theta+\frac{\partial^2 w}{\partial y^2}\cos^2\theta\right)\right]\frac{\partial\delta w}{\partial n}=0 \qquad (2.31)$$

$$\frac{\partial\nabla^2 w}{\partial n}-(1-\nu)\frac{\partial}{\partial s}\left[\left(\frac{\partial^2 w}{\partial x^2}-\frac{\partial^2 w}{\partial y^2}\right)\cos\theta\sin\theta+\frac{\partial^2 w}{\partial x\partial y}\left(\sin^2\theta-\cos^2\theta\right)\right]=0$$

Then the EOM obtained by variational approach can be written as:

$$D\nabla^4 w+\rho h\frac{\partial^2 w}{\partial t^2}=f(x,y,t) \qquad (2.32)$$

As expected, EOMs obtained from both approaches are the same. Equilibrium approach is straightforward and does not require calculation of integral as complicated as variational approach requires. However, there are two significant advantages of using variational approach. First one is that variational approach gives not only the equation of motion but also boundary conditions which are very hard to construct time to time. Second advantage is that energy equations are calculated in the procedure of the variational approach. These equations can be used in the solution of EOM, if one of the energy method is selected as in the case of this thesis study. It helps to understand the solution procedure.

2.3.1.3. Solution of EOM of Plate Using Rayleigh – Ritz Method

Solution method for equation of motion of plate varies with boundary conditions. Boundary conditions of having two opposite edges are simply supported and other two are either free or clamped have been widely studied and well documented. As stated in [7], the problem of vibration of plate having all edges free or clamped is much more complicated. It is possible to find exact and simple characteristic equation for the six cases which includes two simply supported (SS), clamped (C) and free (F) edges. These exact solutions for SS-C-SS-F, SS-SS-SS-SS, SS-C-SS-C, SS-F-SS-F, SS-SS-SS-F and SS-SS-SS-C plates are given in [9]. However, due to difficulties and

complexities in obtaining simple and compact solution for FFFF plate as stated before, energy methods are utilized. For the plate having all edges free, there are only natural boundary conditions at the free edges and free corners. Therefore, selected trial functions which are comparison functions for assumed modes should satisfy those natural boundary conditions, as described later.

For the free vibration of plates, EOM is reduced to Equation 2.33. Corresponding boundary conditions are the zero shear force and moments at all of the edges.

$$D\nabla^4 w + \rho h \frac{\partial^2 w}{\partial t^2} - f(x, y, t) = 0 \tag{2.33}$$

The transverse displacement of any point in xy plane $w(x, y, t)$ is given by:

$$w(x, y, t) = B\theta(x)\phi(y)\sin(\omega t) \tag{2.34}$$

where $\theta(x)$ and $\phi(y)$ are characteristic beam functions for different mode shapes as proposed in [11] and B is the amplitude of oscillations. In general, it is possible to find a deflection wave form $w(x, y, t)$ satisfying Equation 2.33 and all boundary conditions. An infinite series is assumed for the mode shape with the condition that each of the terms in the assumed series satisfy the natural boundary conditions. However, this method yields a matrix with infinite dimensions. Determinant of that matrix later will be equated to zero to obtain characteristic equation. Roots of the determinant is actually eigenvalues of the eigenvalue problem obtained using the assumed mode shapes. Natural frequencies are obtained by taking square root of the eigenvalues [11]. Since it is impractical to calculate determinant of matrix having infinite dimensions, energy methods are utilized with the assumed mode shapes satisfying geometric boundary conditions. This principle is known as Rayleigh method and it is described in [12]. In this method, maximum value of a natural frequency is calculated for only one mode shape. In other words, natural frequency of the mode shape is always smaller than the value found using Rayleigh method, because incorrect assumption of the mode shape imposes extra constraints to the system. In this thesis study, Rayleigh-Ritz method used due to two main advantages:

1. One can calculate several number of natural frequencies and mode shapes at once. In this method, number of trial functions (p) is equal to the dimensions of square stiffness and mass matrices. It will be equal to number of eigenvalues obtained from the eigenvalue problem constructed using these matrices.

2. As the number of assumed mode shapes, trial functions, increased, accuracy of the mode shapes increases. The most significant improvement in accuracy is on the first natural frequency. Effect of the improvement decreases from the first to the last mode shape of interest.

Energy equations for a rectangular plate are given at [13] which are also given in Section 2.3.1.2. The variational approach method for deriving the EOM is chosen to understand the energy methods used in solution better, as described. The method for solution is based on Rayleigh' s principle which can be stated as that the frequency of vibration of a conservative system (no dissipating elements and non-conservative forces) has a stationary value in the neighborhood of a natural mode which is, in fact, a minimum value in the neighborhood of the fundamental natural mode [51]. Rayleigh principle is actually a minimization problem of the Rayleigh quotient (R) which is defined as:

$$R = \omega^2 = \frac{V_{mav}}{T_{\max}} \tag{2.35}$$

In the Rayleigh-Ritz method, a closer approximation to the stationary value can be obtained by superposing several trial functions rather than using a single one. As the number of trial functions increases, accuracy and computational work also increase.

The Potential energy equation is given as:

$$V = \frac{D}{2} \iint_A \left\{ \left(\frac{\partial^2 w}{\partial x^2} + \frac{\partial^2 w}{\partial y^2} \right)^2 - 2(1-\nu) \left[\frac{\partial^2 w}{\partial x^2} \frac{\partial^2 w}{\partial y^2} - \left(\frac{\partial^2 w}{\partial x \partial y} \right)^2 \right] \right\} dxdy \tag{2.36}$$

Kinetic energy equation is:

$$T = \frac{\rho h}{2} \iint_A \left(\frac{\partial w}{\partial t} \right)^2 dxdy \tag{2.37}$$

Mode shapes in the form of given Equation 2.38 are assumed to be as follow for the Rayleigh-Ritz method.

$$W(x, y) = \sum_m \sum_n C_{mn} \theta(x) \phi(y) \tag{2.38}$$

where C_{mn} are unknown constant, Ritz coefficients, and $\theta(x)$ and $\phi(y)$ are characteristic beam functions for different mode shapes and boundary conditions. For the beams with both ends are free to move, the characteristic beam functions are given as:

$$\theta(x) = 1 \text{for } m = 0$$

$$\theta(x) = 1 - \frac{2x}{a} \quad \text{for } m = 1$$

$$\theta(x) = \cos\left[\gamma\left(\frac{x}{a} - \frac{1}{2}\right)\right] - \frac{\sin\left(\frac{\gamma}{2}\right)}{\sinh\left(\frac{\gamma}{2}\right)} \cosh\left[\gamma\left(\frac{x}{a} - \frac{1}{2}\right)\right] \quad \text{for } m = 2,4,6...$$

$$\text{where} \quad \tan\left(\frac{\gamma}{2}\right) + \tanh\left(\frac{\gamma}{2}\right) = 0 \tag{2.39}$$

$$\theta(x) = \sin\left[\gamma'\left(\frac{x}{a} - \frac{1}{2}\right)\right] + \frac{\sin\left(\frac{\gamma}{2}\right)}{\sinh\left(\frac{\gamma}{2}\right)} \sinh\left[\gamma'\left(\frac{x}{a} - \frac{1}{2}\right)\right] \quad \text{for } m = 3,5,7...$$

$$\text{where} \quad \tan\left(\frac{\gamma'}{2}\right) - \tanh\left(\frac{\gamma'}{2}\right) = 0$$

For $\phi(y)$, one needs to replace x with y. With the assumed mode given in Equation 2.38, the maximum strain and kinetic energy can then be expressed as:

$$V_{\max} = \frac{D}{2} \iint_A \left\{ \left(\frac{\partial^2 W}{\partial x^2} + \frac{\partial^2 W}{\partial y^2} \right)^2 - 2(1-\nu) \left[\frac{\partial^2 W}{\partial x^2} \frac{\partial^2 W}{\partial y^2} - \left(\frac{\partial^2 W}{\partial x \partial y} \right)^2 \right] \right\} dxdy$$
$$= \frac{1}{2} \sum_{i=1}^{p} \sum_{j=1}^{p} c_i c_j k_{ij} = \frac{1}{2} \vec{c}^{\mathrm{T}} [K] \vec{c} \tag{2.40}$$

$$T_{\max} = \frac{\rho h}{2} \iint_A \left(\frac{\partial W}{\partial t} \right)^2 dxdy = \frac{1}{2} \sum_{i=1}^{p} \sum_{j=1}^{p} c_i c_j m_{ij} = \frac{1}{2} \vec{c}^{\mathrm{T}} [M] \vec{c} \tag{2.41}$$

From the theory of Rayleigh principle,

$$T_{\max} = \omega^2 T^*{}_{\max} \tag{2.42}$$

In the maximum energy equations (Equations 2.40 and 2.41), $[K]$ and $[M]$ are stiffness and mass matrices, respectively. $\vec{c}$ is the vector composed of unknown constant coefficients which are denoted as C_{mn} in the assumed mode shape Equation 2.38. p is the number of terms in that mode shape that is:

$$p = m \times n \tag{2.43}$$

The unknown coefficient vector is:

$$\vec{c} = \begin{Bmatrix} c_1 \\ c_2 \\ \vdots \\ c_p \end{Bmatrix} \tag{2.44}$$

Putting the potential and kinetic energy terms given in Equations 2.40 and 2.41 into Rayleigh quotient given in Equation 2.35, R is obtained as a function of unknown coefficients.

$$R(c_1, c_2, \cdots, c_p) = \frac{V_{\max}(c_1, c_2, \cdots, c_p)}{T_{\max}(c_1, c_2, \cdots, c_p)} \tag{2.45}$$

As stated before, vibration frequencies have stationary value in the neighborhood of natural frequencies. That is the minimum value of Rayleigh' s quotient and it can be found by equating rate of change of R with respect to constant coefficients to zero.

$$\begin{aligned}
&\frac{\partial R}{\partial c_i}=\frac{T^*{}_{\max}\left(\dfrac{\partial V_{\max}}{\partial c_i}\right)-V_{\max}\left(\dfrac{\partial T^*{}_{\max}}{\partial c_i}\right)}{T^*{}_{\max}{}^2}=0, \qquad i=1,2,\cdots,p\\
&\frac{1}{T^*{}_{\max}}\left[\left(\frac{\partial V_{\max}}{\partial c_i}\right)-\frac{V_{\max}}{T^*{}_{\max}}\left(\frac{\partial T^*{}_{\max}}{\partial c_i}\right)\right]=0, \qquad i=1,2,\cdots,p\\
&\frac{1}{T^*{}_{\max}}\left(\frac{\partial V_{\max}}{\partial c_i}-\lambda^{(p)}\frac{\partial T^*{}_{\max}}{\partial c_i}\right)=0, \qquad i=1,2,\cdots,p
\end{aligned} \tag{2.46}$$

where $\lambda^{(p)}$ is the pth eigenvalue of the eigenvalue problem. Moreover, $\lambda^{(p)}$ is defined as Rayleigh' s quotient and it is equal to ω^2. Equation 2.46 can be written in matrix form as well, which gives the correlation between stiffness and mass distributions found in Equations 2.40 and 2.41.

$$\frac{\partial R}{\partial \vec{c}}=\frac{1}{T^*{}_{\max}}\left(\frac{\partial V_{\max}}{\partial \vec{c}}-\lambda^{(p)}\frac{\partial T^*{}_{\max}}{\partial \vec{c}}\right)=\vec{0} \tag{2.47}$$

where

$$\begin{aligned}
\frac{\partial V_{\max}}{\partial \vec{c}}&=\frac{1}{2}\vec{c}^{\mathrm{T}}[K]\\
\frac{\partial T^*{}_{\max}}{\partial \vec{c}}&=\frac{1}{2}\vec{c}^{\mathrm{T}}[M]
\end{aligned} \tag{2.48}$$

Then the Equation 2.46 is written in matrix form follow:

$$\left[[K]-\lambda^{(p)}[M]\right]\vec{c}=\vec{0} \tag{2.49}$$

which is an eigenvalue problem of order p. Well known nontrivial solution of this eigenvalue problem gives the natural frequencies of the plate.

$$\omega_i = \sqrt{\lambda_i^{(p)}}, \quad i = 1,2,\cdots,p \tag{2.50}$$

After finding natural frequencies of the plate, the vector of Ritz coefficients, $\vec{c}_i$, corresponding to i^{th} natural frequency should be determined by solving the eigenvector part of the eigenvalue problem.

$$\left[[K] - \lambda^{(p,i)}[M]\right]\vec{c}^{(i)} = \vec{0} \tag{2.51}$$

Then the mode shape of ith mode is given as:

$$\begin{aligned} W^{(i)}(x,y) &= \sum_m \sum_n c_p{}^{(i)} \theta_m(x) \phi_n(y) \\ &= c_1{}^{(i)} \theta_1(x)\phi_1(y) + c_2{}^{(i)} \theta_1(x)\phi_2(y) + \cdots, \qquad i = 1,2,\cdots,p \end{aligned} \tag{2.52}$$

In this thesis work, first two mode shapes, (1,1) and (2,0) - (0,2), of a Chladni plate is studied due to two main reasons;

1. In the modelling of vibration of plate, shear deformations are neglected. Shear deformations are smallest at these mode shapes. Therefore, analytical model is more accurate for those mode shapes.

2. Deflections in modes-of-interest are greater than the higher mode shapes, which results higher actuating force and sense signal.

The transverse vibration of a square plate can be solved with infinite series assumption as stated before. However, it is solved by an equivalent n-degree-of-freedom system. The accuracy of results of Rayleigh-Ritz method increases with increasing number of trial functions. To see this effect clearly, number of terms in the mode shapes assumption for p=3, 4, 9, 16, 25, 36 and 64 are studied. Changes in natural frequencies of modes-of-interest are smaller than 0.1% for $n > 16$. Moreover, it is observed that effect of hyperbolic functions in the assumed mode shape is very small. Therefore, they can also be dropped. In this study, results of assumed mode shapes with 16 terms containing hyperbolic functions are given. In Table 2.2, mode shapes for modes (1,1)

and (2,0) - (0,2) are presented. The given mode shapes are normalized with respect to second norm of the coefficient vector.

Table 2.2: Obtained mode shapes for mode-of-interest with Rayleigh-Ritz method. Mode shapes are normalized with respect to second norm of coefficient vector.

Mode shapes of modes-of-interest	
$W_{(1,1)}(x,y) = 0.99911\theta_1(x)\phi_1(y) - 0.0307\theta_1(x)\phi_3(y) - 0.0307\theta_3(x)\phi_1(y) - 0.0039\theta_3(x)\phi_3(y)$	(2.53)
$W_{(2,0)-(0,2)} = 0.70711\phi_2(y) - 0.70711\theta_2(x)$	(2.54)

Mode shapes obtained with Rayleigh-Ritz method are useful in building a closed form equation for natural frequencies of the plate. To write a closed form equation for natural frequencies, total strain and kinetic energy stored in the mode shape are written. Equivalent stiffness and masses are found for each mode shapes.

$$V_{\max} = \frac{D}{2}\iint_A \left\{ \left(\frac{\partial^2 W}{\partial x^2} + \frac{\partial^2 W}{\partial y^2} \right)^2 - 2(1-\nu)\left[\frac{\partial^2 W}{\partial x^2}\frac{\partial^2 W}{\partial y^2} - \left(\frac{\partial^2 W}{\partial x \partial y} \right)^2 \right] \right\} dxdy = \frac{1}{2} K_{eff} [W_0(x_0, y_0)]^2 \tag{2.55}$$

$$T_{\max}{}^* = \frac{\rho h}{2}\iint_A [W(x,y)]^2 dxdy = \frac{1}{2} M_{eff} [W_0(x_0, y_0)]^2 \tag{2.56}$$

where $W_0(x_0, y_0)$ is the point on the square plate which has the maximum deflection and (x_0, y_0) is the location of that point. The maximum deflection point differs for different mode shapes. Then, undamped natural frequency in Hz is calculated as:

$$\omega_n = \frac{1}{2\pi}\sqrt{\frac{K_{eff}}{M_{eff}}} \tag{2.57}$$

In Table 2.3, closed form expressions for effective stiffness and mass together with the closed form natural frequency equations for the modes-of-interest are presented.

Table 2.3: Closed form equations for equivalent stiffness, mass and un undamped natural frequencies for modes-of-interest, which are obtained using resulting modes shapes of Rayleigh-Ritz method.

	Mode (1,1)		**Mode (2,0) – (0,2)**	
K_{eff}	$5.1276\times10^{-5}\dfrac{Eh^3}{12a^4\left(1-\nu^2\right)}$	(2.58)	$1.5544\times10^{-4}\dfrac{Eh^3}{12a^4\left(1-\nu^2\right)}$	(2.59)
M_{eff}	$2.6658\times10^{-7}\rho h$	(2.60)	$3.7910\times10^{-7}\rho h$	(2.61)
ω_n	$\dfrac{13.869}{2\pi a^2}\sqrt{\dfrac{Eh^2}{12\rho\left(1-\nu^2\right)}}$	(2.62)	$\dfrac{20.249}{2\pi a^2}\sqrt{\dfrac{Eh^2}{12\rho\left(1-\nu^2\right)}}$	(2.63)

The constant coefficients in the closed form equations of natural frequency are 13.869 and 20.249 for modes (1,1) and (2,0) – (0,2), respectively. Corresponding constants for each mode shape are stated as 13.49 and 19.79 in [9]. Both values are very close. The reasons of difference are;

1. Number of trial functions in the assumed mode shape is different.
2. In the literature, researcher have investigated material steel; however, specifically for this thesis study, material silicon is used and it has a Poisson' s ratio different than steel.

It is well known and proved that electrostatic actuation has a negative effect on stiffness [52]. In the effective stiffness equations given in Table 2.3, effect of electrostatic actuation is not included as it will be included in Section 2.3.2.3.

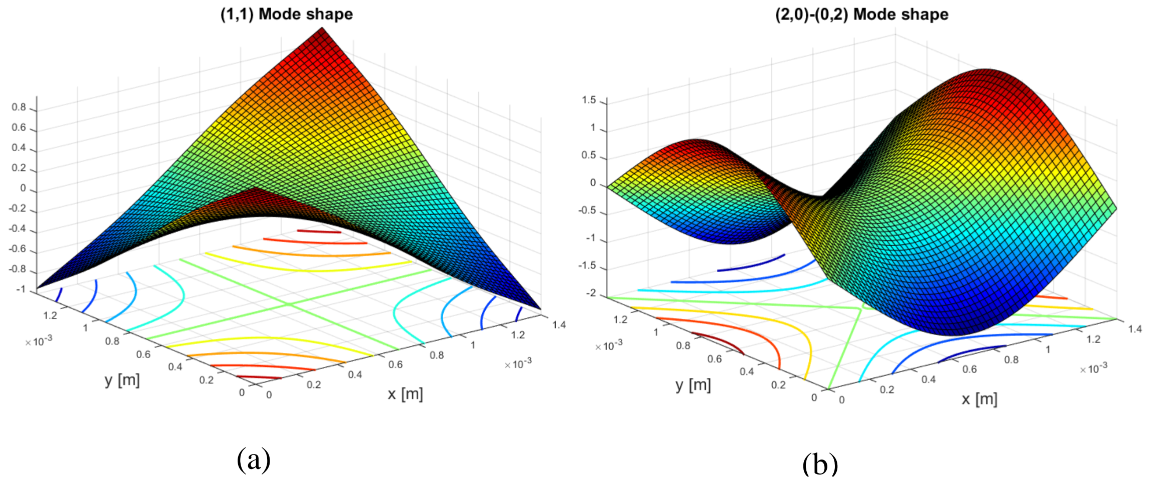

(a) (b)

Figure 2.5: Mode shapes of modes-of-interest obtained by assuming characteristic beam function of free-free beam with 16 terms. a) (1,1) mode shape and b) (2,0) – (0,2) mode shape. Underneath the mode shapes counter lines are drawn and green counter lines stand for nodal lines, motionless lines and referred to Chladni figures.

With the analytical model given above for transverse vibration of FFFF plate, the natural frequencies of mode (1,1) and (2,0) – (0,2) are calculated to be 100.71 kHz and 147.04 kHz, respectively. Corresponding mode shapes are given in Figure 2.6. Green counter lines are the nodal lines and they are identical to Chladni figures of corresponding modes. As stated before, the mode shapes are normalized with respect to length of Ritz coefficients vector; therefore, maximum deflections are not unity.

2.3.2. Analytical Model of Capacitive Actuation and Detection

Capacitive actuation and sensing is one of the mostly used technique for the purpose of driving and sensing in MEMS devices. Mechanical displacement of a conductive material is converted to electrical signal or vice versa. In both case, energy is transduced between two domains, mechanical and electrical.

2.3.2.1.Capacitive Actuation

Electrostatic force is induced to minimize the stored electrostatic energy by the attraction or repelling of two differently charged conductive substances. The

electrostatic force driving the MEMS square plate resonator is due to attraction between the plate itself and the electrodes placed underneath the plate.

Electrostatic force is equal to the gradient of the electrostatic energy with respect to spatial coordinates. In the case of plate resonator, electrostatic potential energy is function of one spatial coordinate, since displacement is in one axis, z . Then the electrostatic force is calculated as:

$$F_e = \frac{\partial}{\partial z} \underbrace{\left(\frac{1}{2} C V^2 \right)}_{Electrocstatic energy} \qquad (2.64)$$

where C is the capacitance and V is the difference of potentials applied to the resonating plate and electrodes. In Figure 2.6, formed capacitance and applied potentials are visualized.

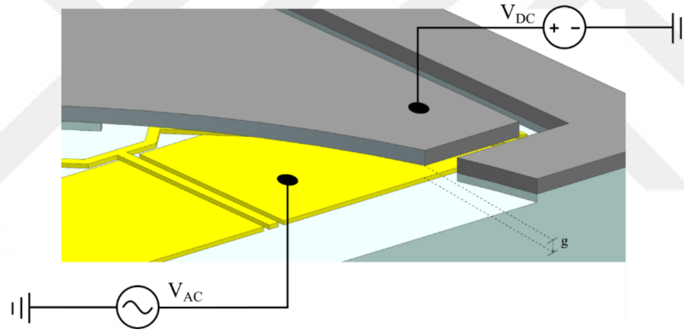

Figure 2.6: The capacitance formed by plate and electrodes with applied voltages.

A DC voltage is applied to resonating body as proof mass voltage and a AC voltage is applied to the driving electrodes. Then the formed capacitance is calculated as:

$$C = \frac{\varepsilon_0 A}{g} \qquad (2.65)$$

In Equation 2.65, ε_0 is the dielectric permittivity of the medium between the plate and the electrodes, A is the capacitive area that is the overlapping area, and g is the capacitive gap. It is also well known that there are fringing field effects for the formed

capacitance. Fringing field factor is an empirical factor and it depends on the shape and thickness of the structure [23]. In this study, the effect of this fringing field is ignored. The gap between the proof mass and the electrodes subject to change upon the application of potentials to the proof mass and the electrodes. Since the capacitance is function of the gap, it also changes. Then, the force generated is calculated as:

$$F_e = \frac{\partial}{\partial z}\left[\frac{1}{2}\left(\frac{\varepsilon_0 A}{g-z}V^2\right)\right] \tag{2.66}$$

In Equation 2.66, only the gap is function of displacement. Then the derivative is calculated as:

$$F_e = -\frac{1}{2}\frac{\varepsilon_0 a^2}{(g-z)^2}V^2 \tag{2.67}$$

As stated before, a represents the side length of a square plate. Potential difference between the plate and electrodes is the difference of AC and DC voltages shown in Figure 2.6.

$$\begin{aligned} V &= V_{ac}\sin(\omega t) - V_p \\ V^2 &= V_{ac}^{\ 2}\sin^2(\omega t) - 2V_p V_{ac}\sin(\omega t) + V_p^{\ 2} \end{aligned} \tag{2.68}$$

Rearranging the terms with half sine formula yields:

$$V^2 = \underbrace{\left(\frac{V_{ac}^{\ 2}}{2} + V_p^{\ 2}\right)}_{DC\ term} - \underbrace{2V_p V_{ac}\sin(\omega t)}_{Single\ frequency\ term} - \underbrace{\left(\frac{V_{ac}^{\ 2}}{2}\cos(2\omega t)\right)}_{Double\ frequency\ term} \tag{2.69}$$

Combining Equations 2.66 and 2.69, electrostatic force due to the displacement of capacitive plates is calculated as:

$$F_e = -\frac{1}{2}\frac{\varepsilon_0 a^2}{(g-z)^2}\left[\underbrace{\left(\frac{V_{ac}^{\ 2}}{2}+V_p^{\ 2}\right)}_{DC\ \ term} - \underbrace{2V_pV_{ac}\sin(\omega t)}_{Single\ \ frequency\ \ term} - \underbrace{\left(\frac{V_{ac}^{\ 2}}{2}\cos(2\omega t)\right)}_{Double\ \ frequency\ \ term}\right] \quad (2.70)$$

The main driving force is the single frequency term in Equation 2.70. This force is linearly dependent on the magnitudes of applied AC and DC voltages. In addition, driving force and AC voltage are in phase. On the other hand, there are DC and double frequency terms in the generated force as well. DC term is proportional to sum of the squares of amplitude of applied AC and DC voltages. Double frequency term has a frequency of twice the frequency of applied AC voltage and its magnitude is function of magnitude of the AC voltage. Most of the time in tests, the magnitude of the AC voltage is very small due to device capabilities used in frequency response characterizations. Therefore, double frequency term has very small magnitude compared to the single frequency term. By designing natural frequency of the resonator at the frequency of applied AC voltage, the DC term and double frequency term in force equation can be neglected, since the amplitude of oscillations in resonance are very large compared to the amplitudes at zero and double frequencies.

In the modelling of electrostatic actuation, static deflection of the plate under the applied proof mass voltage is much smaller than the original capacitive gap. This assumption is validated with an electromechanical FE simulation in the Section 2.4.1.

2.3.2.2.Capacitive Detection

The displacement of the proof mass affects the capacitance formed between electrodes and the proof mass. Capacitive sensing is based on this capacitance change as in the case of capacitive driving. As the capacitance between proof mass and sense electrodes changes, stored charge in the capacitance also changes by means of the current flowing through sense electrodes. There are two types of capacitive sensing: varying gap and varying overlap area. In the former, capacitance change is due to change in gap between capacitive plates. On the other hand, capacitance changes due to the change

in the overlapping area of the capacitive plates for the letter case. In the varying gap capacitors, capacitance is a nonlinear function of displacement, whereas overlap area capacitors are linear functions of the displacement. The sensitivity of varying gap capacitor is higher, since it depends on square of the gap.

As stated, stored charges varies with a current passing through the capacitor. This current is converted into voltages with a trans-impedance amplifier (TIA) as shown in Figure 2.7.

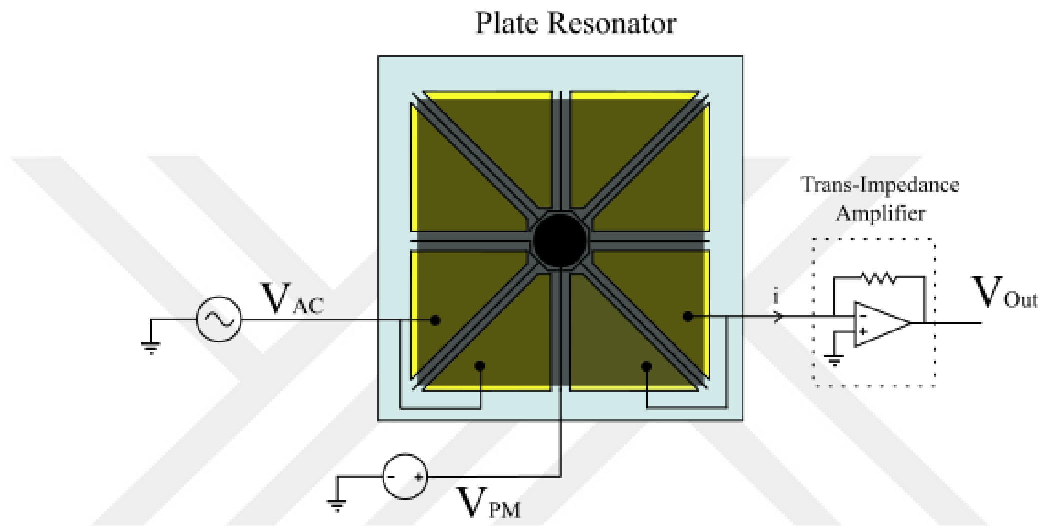

Figure 2.7: Capacitive sensing application. Some of the eight electrodes are used for driving the resonator and the others used for sensing. These electrodes may be interchanged according to mode shape under test.

Electrodes used for driving and sensing purposes are grouped according to the mode shape of interest. There are eight electrodes standing on the glass substrate and each of them can be used either for driving or sensing. The charge in a capacitor is calculated as follows:

$$Q = CV \tag{2.71}$$

where Q is the charge. Then the current through that capacitor equals to time rate of change of the charge. That is:

$$\frac{\partial Q}{\partial t} = i = \frac{\partial C}{\partial t} V + C \frac{\partial V}{\partial t} \qquad (2.72)$$

As stated before, the magnitude of AC signal is very small compared to the proof mass voltage and sensing electrodes are connected to the virtual ground of operational amplifier. Therefore, the second term in Equation 2.72 is almost zero and it is neglected. Then, the current is written as follows using the chain rule of differentiation:

$$i = \frac{\partial C}{\partial z} \frac{\partial z}{\partial t} V_{DC} = -\frac{\varepsilon_0 a^2}{(g-z)^2} \frac{\partial z}{\partial t} V_{PM} \qquad (2.73)$$

Equation 2.73 implies that, the current output of a capacitance change is actually a measure of velocity of the proof mass with a DC voltage applied. As seen in Figure 2.7, an op-amp is used in TIA. The output is connected to inverting leg with an impedance. Then:

$$V_{out} = -iZ = -iR_{fb} \qquad (2.74)$$

The impedance is a feedback resistor and values of all the parameters are given in Table 2.1. Inserting Equation 2.73 into Equation 2.74 yields:

$$V_{out} = -\frac{\varepsilon_0 a^2}{(g-z)^2} R_{fb} V_{PM} \frac{\partial z}{\partial t} \qquad (2.75)$$

It is obvious that output voltage is expected to have a 90° phase difference with respect to the applied AC signal, since there is a differentiation.

2.3.2.3.Softening Effect of Capacitive Actuation

Capacitances formed by moving parts experience a softening affect due to the nonlinear nature of the forces created by the electrical field within the capacitor. This effect is studied and formulated for beam structures as it can be found in [19]. For this study, energy equations are utilized to model this softening effect in transverse

vibration of the plates. As before, the electrostatic energy in the capacitance formed by electrodes and the plate is given as:

$$E = \frac{1}{2} C V^2 \tag{2.76}$$

The potential difference between proof mass and electrodes is taken as V_{PM} , since the amplitude of AC voltage applied to the electrodes are very small compared to proof mass voltage. The capacitance is written in terms of deflections in the modes-of-interest.

$$C = \frac{\varepsilon_0 A}{g - BW(x, y)} \tag{2.77}$$

where B is the amplitude of vibration, ε_0 is the permittivity of the medium between plate and electrodes and A is the overlapping area. Then the energy equation yields to:

$$E = \frac{1}{2} \iint_A \frac{\varepsilon_0 A}{g - Bw(x, y)} V_{PM}{}^2 dA \tag{2.78}$$

The overlapping area is important at this point. For the actual design, overlapping area composes of eight trapezoids that are the electrodes. Therefore, the integration limits should be taken accordingly. To validate the correctness of the approach of finding electrostatic stiffness, the overlapping area is taken as both a single square electrode having side length exactly same as the plate side length and actual design that is the area of eight trapezoidal electrodes. Results of both case is compared with the finite element simulations and test results whichever is available in the upcoming sections.

The equivalent electrostatic stiffness at the maximum deflection points is calculated with the same approach used for equivalent stiffness and mass calculation. That is:

$$E = \frac{1}{2} \iint_A \frac{\varepsilon_0}{g - Bw(x, y)} V_{PM}{}^2 dA = \frac{1}{2} k_e \left[BW_0(x_0, y_0) \right]^2 \tag{2.79}$$

The integral in Equation 2.79 can be simplified as follow:

$$\iint_A \frac{\varepsilon_0}{g - Bw(x,y)} V_{PM}{}^2 dA = \frac{\varepsilon_0 V_{PM}{}^2}{g} \iint_A \frac{1}{1 - \frac{Bw(x,y)}{g}} dA \tag{2.80}$$

Further simplification is done using Taylor Series expansion to the term inside the integral 2.80.

$$\frac{\varepsilon_0 V_{PM}{}^2}{g} \iint_A \frac{1}{1 - \frac{Bw(x,y)}{g}} dA = \frac{\varepsilon_0 V_{PM}{}^2}{g} \iint_A \left[1 + \frac{B}{g} w(x,y) + \left(\frac{B}{g}\right)^2 w^2(x,y) + \cdots \right] dA \tag{2.81}$$

For the modes-pf interest, integral of odd power of deflection equals to zero due to fact that positively and negatively deflected regions are equal and they cancel each other. Knowing that the effect of higher terms is small, they are neglected. The oscillations are around the equilibrium point. Therefore, the constant one in the Equation 2.81 which is not function of oscillations is responsible for static deflection and has no effect on the softening. Hence; it also neglected and following equation is obtained.

$$\frac{\varepsilon_0 V_{PM}{}^2}{g} \iint_A \frac{1}{1 - \frac{Bw(x,y)}{g}} dA \cong \frac{\varepsilon_0 V_{PM}{}^2}{g} \iint_A \left(\frac{B}{g}\right)^2 w^2(x,y) dA = \frac{B^2 \varepsilon_0 V_{PM}{}^2}{g^3} \iint_A w^2(x,y) dA \tag{2.82}$$

Inserting Equation 2.82 into Equation 2.79 yields to electrostatic spring constant.

$$k_e = \frac{\varepsilon_0 V_{PM}{}^2}{g^3} \iint_A w^2(x,y) dA \tag{2.83}$$

Table 2.4 summarizes the calculated electrostatic spring constant for both single square electrode case, SSE, which is all the plate area is used as capacitive area and trapezoidal electrode case, TE, which is the designed case.

Table 2.4: Closed form expressions of electrostatic spring constants for both single square electrode and trapezoidal electrodes

Electrostatic spring constant	**Mode (1,1)**	**Mode (2,0) – (0,2)**
$k_{e,SSE}$	$\frac{0.136\varepsilon_0 a^2}{g^3} {V_{PM}}^2$ (2.84)	$\frac{0.193\varepsilon_0 a^2}{g^3} {V_{PM}}^2$ (2.85)
$k_{e,TE}$	$\frac{0.106\varepsilon_0 a^2}{g^3} {V_{PM}}^2$ (2.86)	$\frac{0.174\varepsilon_0 a^2}{g^3} {V_{PM}}^2$ (2.87)

Closed form frequency equation is obtained by utilizing the electrostatic spring constant given in Table 2.4 and Equation 2.57. For the designed electrode layout, the closed form natural frequency equation for mode (1,1) is given in Table 2.5.

Table 2.5: Closed form equation of natural frequency of mode (1,1) with the electrostatic softening effect included for trapezoidal electrode layout.

	Mode (1,1)	
K_{eff}	$5.1276\times10^{-5} \frac{Eh^3}{12a^4(1-\nu^2)}$	(2.88)
$k_{e,TE}$	$\frac{0.106\varepsilon_0 a^2}{g^3} {V_{PM}}^2$	(2.89)
M_{eff}	$2.6658\times10^{-7}\rho h$	(2.90)
ω_n	$\frac{1}{2\pi}\sqrt{\frac{5.1276\times10^{-5} \frac{Eh^3}{12a^4(1-\nu^2)} - \frac{0.106\varepsilon_0 a^2}{g^3} {V_{PM}}^2}{2.6658\times10^{-7}\rho h}}$	(2.91)

For the designed electrode layout, the closed form natural frequency equation for mode (2,0) – (0,2) is given in Table 2.6.

Table 2.6: Closed form equation of natural frequency of mode (2,0) – (0,2) with the electrostatic softening effect included for trapezoidal electrode layout.

	Mode (2,0) – (0,2)	
K_{eff}	$1.5544\times10^{-4}\dfrac{Eh^3}{12a^4(1-\nu^2)}$	(2.92)
$k_{e,TE}$	$\dfrac{0.174\varepsilon_0 a^2}{g^3}V_{PM}{}^2$	(2.93)
M_{eff}	$3.7910\times10^{-7}\rho h$	(2.94)
ω_n	$\dfrac{1}{2\pi}\sqrt{\dfrac{1.5544\times10^{-4}\dfrac{Eh^3}{12a^4(1-\nu^2)}-\dfrac{0.174\varepsilon_0 a^2}{g^3}V_{PM}{}^2}{3.7910\times10^{-7}\rho h}}$	(2.95)

As expected, increasing proof mass voltage decreases the natural frequency of the structure due to softening effect. Derived formulas are validated with finite element simulations and test results whichever is available in the next sections.

2.3.3. Analytical Model of Temperature Effect on Natural Frequencies of Modes-of-Interest

As mentioned before, natural frequency of a structural system having mass and stiffness is a system parameter. Natural frequency, by definition, is function of other system parameters which are mass, stiffness and damping. Most of the mechanical properties effecting the vibration characteristics of a substance such as modulus of elasticity, Poisson's ratio, dimensions are subjected to change with temperature. That means, natural frequency of the vibrating body is function of temperature. Given closed form equations in Section 2.3.2.3 are functions of geometric and material parameters, all of which are also function of temperature. Then, the effect of

temperature on the natural frequencies are modelled by inserting the temperature effect into each and every parameter.

Thermal coefficient of modulus of elasticity, thermal coefficient of expansion for the materials silicon and silicon dioxide are given in Table 2.1. In this section, the subscribe zero stand for the initial state that is the state at room temperature. Table 2.1 contains the values of initial states.

Effect of temperature on the density is obtained as:

$$\rho = \frac{m}{\forall} \tag{2.96}$$

where m is the mass and $\forall$ is the volume of the structure. Since the mass of the body does not change as it is heated up to a comparable value with the room temperature, density is obtained from the initial mass and volume.

$$\begin{aligned} m &= \rho \forall = \rho_0 \forall_0 \\ \rho &= \rho_0 \frac{\forall_0}{\forall} = \rho_0 \frac{a_0^{\,2} h_0}{a_0^{\,2}(1+\alpha_{Si}\Delta T)^2 h_0 (1+\alpha_{Si}\Delta T)} \end{aligned} \tag{2.97}$$

Then density is obtained as a function of temperature difference as follow:

$$\rho = \frac{\rho_0}{(1+\alpha_{Si}\Delta T)^3} \tag{2.98}$$

Temperature effect on the natural frequencies is modelled by inserting all of the parameters as a function of temperature into the natural frequency equations of modes-of-interest.

Table 2.7: Closed form natural frequency equations as a function of temperature for modes-of-interest.

Mode Shape	Undamped Natural Frequency, ω_n	
(1,1)	$\frac{1}{2\pi}\sqrt{\frac{5.1276\times10^{-5}\frac{E_0(1+\alpha_E\Delta T)h_0^{\,3}(1+\alpha_{Si}\Delta T)}{12a_0^{\,4}(1-\nu^2)}-\frac{0.106\varepsilon_0 a_0^{\,2}(1+\alpha_{Si}\Delta T)^4}{g_0^{\,3}(1+\alpha_{SiO_2}\Delta T)^3}V_{PM}^{\,2}}{2.6658\times10^{-7}\rho_0 h_0}}$	(2.99)
(2,0)-(0,2)	$\frac{1}{2\pi}\sqrt{\frac{1.5544\times10^{-4}\frac{E_0(1+\alpha_E\Delta T)h_0^{\,3}(1+\alpha_{Si}\Delta T)}{12a_0^{\,4}(1-\nu^2)}-\frac{0.174\varepsilon_0 a_0^{\,2}(1+\alpha_{Si}\Delta T)^4}{g_0^{\,3}(1+\alpha_{SiO_2}\Delta T)^3}V_{PM}^{\,2}}{3.7910\times10^{-7}\rho_0 h_0}}$	(2.100)

Closed form natural frequency equations as a function of temperature are given in Table 2.7. Using these closed form equations, it is possible to obtain thermal sensitivity of the designed resonant plate, which will be a long and complicated equation. Results of all the analytical models are validated with the finite element simulations in the next sections.

2.4. Finite Element Modelling of Resonant MEMS Plate Temperature Sensor

The analytical models provided in the previous sections are validated with 3D Finite Element Modelling (FEM). FEM simulations are held in COMSOL Multiphysics environment. This section contains Modal Analysis, Electro-Mechanical Analysis and Thermal Analysis in order to validate analytical models. Moreover, FEM simulations are held in order to see the static deflections under applied proof mass voltage, parasitic modes and behavior of the resonator with changing temperature.

In the FEM analysis, a tetrahedral mesh having size of 0.1µm – 20µm range is used as a result of mesh convergence study given in Figure 2.8. There is only one physical boundary condition which is the fixed post of the resonator. All four edges of the plate are free to move. For the material parameters, values in Table 2.1 are utilized. The built-in library for materials in COMSOL Multiphysics is used for the parameters not given in Table 2.1.

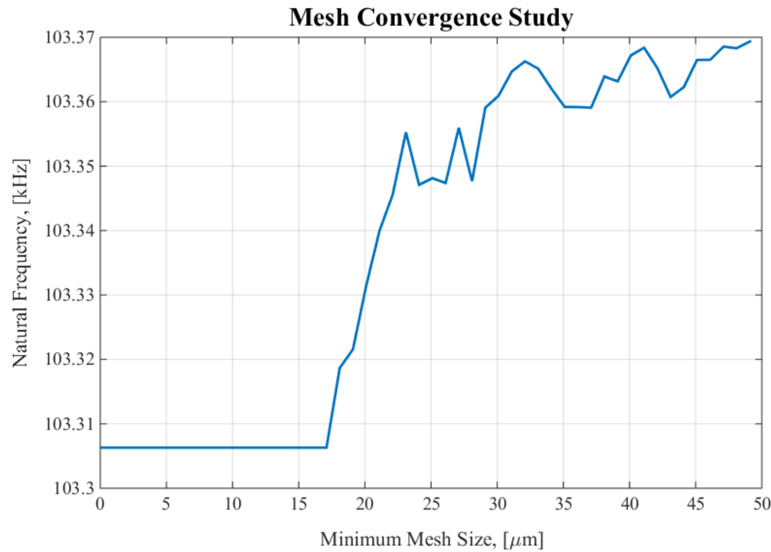

Figure 2.8: Mesh convergence study results done to determine mesh size

As seen, the result of the FE simulation does not change much (smaller than 0.01%) for the mesh sizes smaller than 17µm. The mesh size used in the FE simulations is determined as 0.1-10µm from the results obtained mesh convergence study.

2.4.1. Static Deflection and Pull-in Voltage Simulation of MEMS Plate

In the analytical model of undamped natural frequencies, static deflections are neglected, since they are very small compared to initial gap. To validate this assumption, a static deflection FEM simulations are done for 15V proof mass voltage and grounded bottom electrodes. In this electromechanical FE simulation, electromechanical solver of COMSOL Multiphysics is used. Three dimensional (3D) geometry of the thermal sensor is drawn in SIEMENS Unigraphics software and then it is imported to COMSOL environment. For the physics definitions, all of the bodies, i.e. plate, post and electrodes, are defined as linear elastic materials with the material properties given in Table 2.1. Electrodes underneath the plate are fixed using fixed constraint in the domains selection, since all electrodes are three dimensional bodies. The bottom surface of the post which is connected to substrate is fixed using fixed constraint in the boundaries selection as it is being a surface boundary condition. In addition to these mechanical boundary conditions, there are also electrical boundary

conditions The plate is applied a proof mass voltage of 15V with the selection of terminal and type of terminal is selected as voltage. As mentioned before, applied AC voltage to the electrodes is very small in magnitude compared to proof mass voltage. Therefore, in the static deflection simulations, electrodes are grounded. The capacitive gap between plate and electrodes is filled with a material having unity relative permittivity representing the vacuum.

For the meshing of the geometry, a built-in mesh of type tetrahedral mesh having size of 0.1µm – 20µm range is used. The substrate is not drawn and not included in the FE simulations, since it will create high number of meshes, which increases the simulation time. For the solution, a stationary study utilizing the electromechanics as physics interface is used. In Figure 2.9, the deflection pattern for the applied proof mass voltage of 15V is given. A maximum deflection of 0.773nm is observed at the corners of FFFF plate.

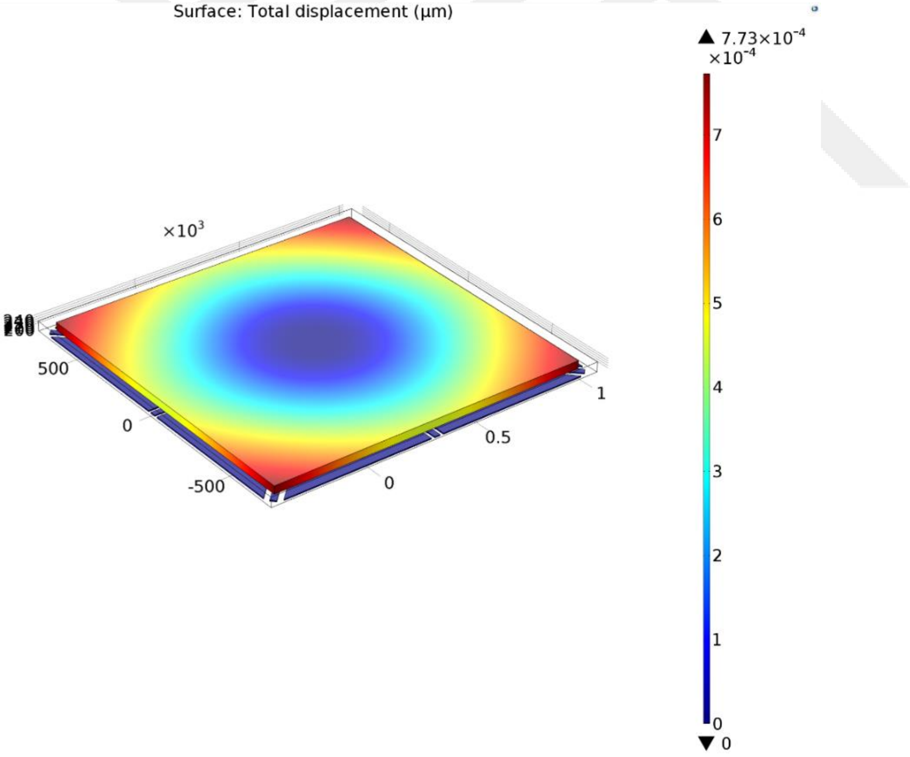

Figure 2.9: Static deflection pattern with exact electrodes and 15V proof mass

Maximum deflections at the corner is very small compared to initial capacitive gap. Therefore, neglecting static deflections for 15V proof mass voltage is reasonable approximation in the modelling. In addition to that, effect of gravity is also simulated by adding a gravity physics to the electromechanical simulations and it is observed that deflections due to gravity is much smaller than the static deflections. It is in the order of one tenth of the static deflections and they are also ignored in the analytical model.

In addition to static deflections, a pull-in analysis done in FE simulations to determine the pull-in voltage. For this electromechanical FE simulation, the electrodes are biased to voltages ranging from 0-1000V in the COMSOL Multiphysics.

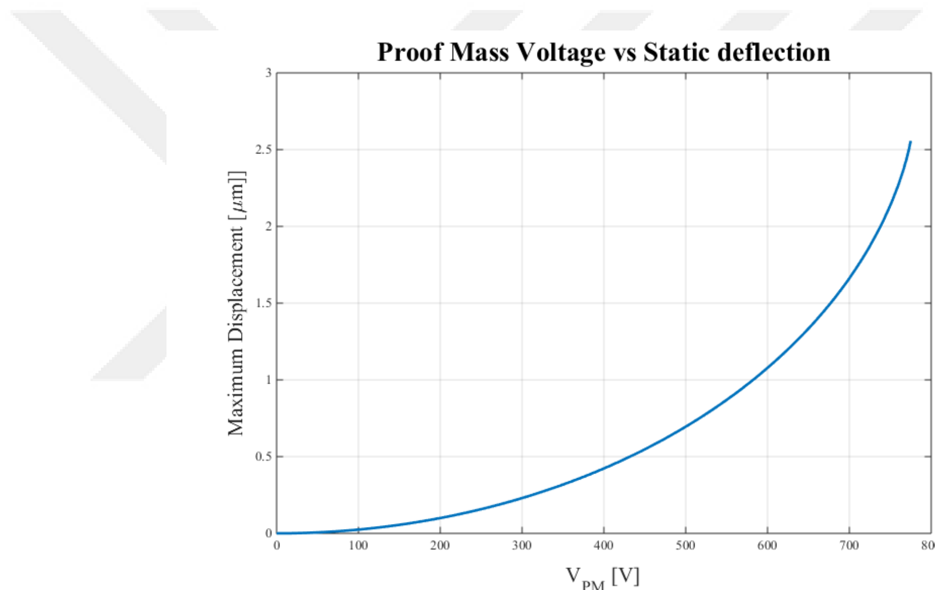

Figure 2.10: FE simulation of maximum static deflection of the plate at the corners versus applied DC proof mass voltage.

In Figure 2.10, the relation between static deflection and applied proof mass voltage is given. FE simulations show that the pull-in voltage is 775V. FE simulations are done for 1V increment each step. Therefore, Pull-in voltage may not be exactly 775V; however, purpose of this analysis is to see the order of pull-in voltage which is much greater than the proof mass voltage used in tests. At this polarization voltage, the modal frequency of mode shape (1,1) is also analyzed and it is found to drop down to 80.49kHz.

2.4.2. Modal Simulations of the Resonant MEMS Square Plate

The modal simulations are held to validate the results obtained from the analytical model of natural frequency calculation of the modes-of-interest. In this part, 3D solid model of only MEMS plate and post are drawn in SIMENS Unigraphics due to purpose of minimizing the number of mashes in FE simulations. In modal FE simulation, solid mechanics solver is used in COMSOL Multiphysics.

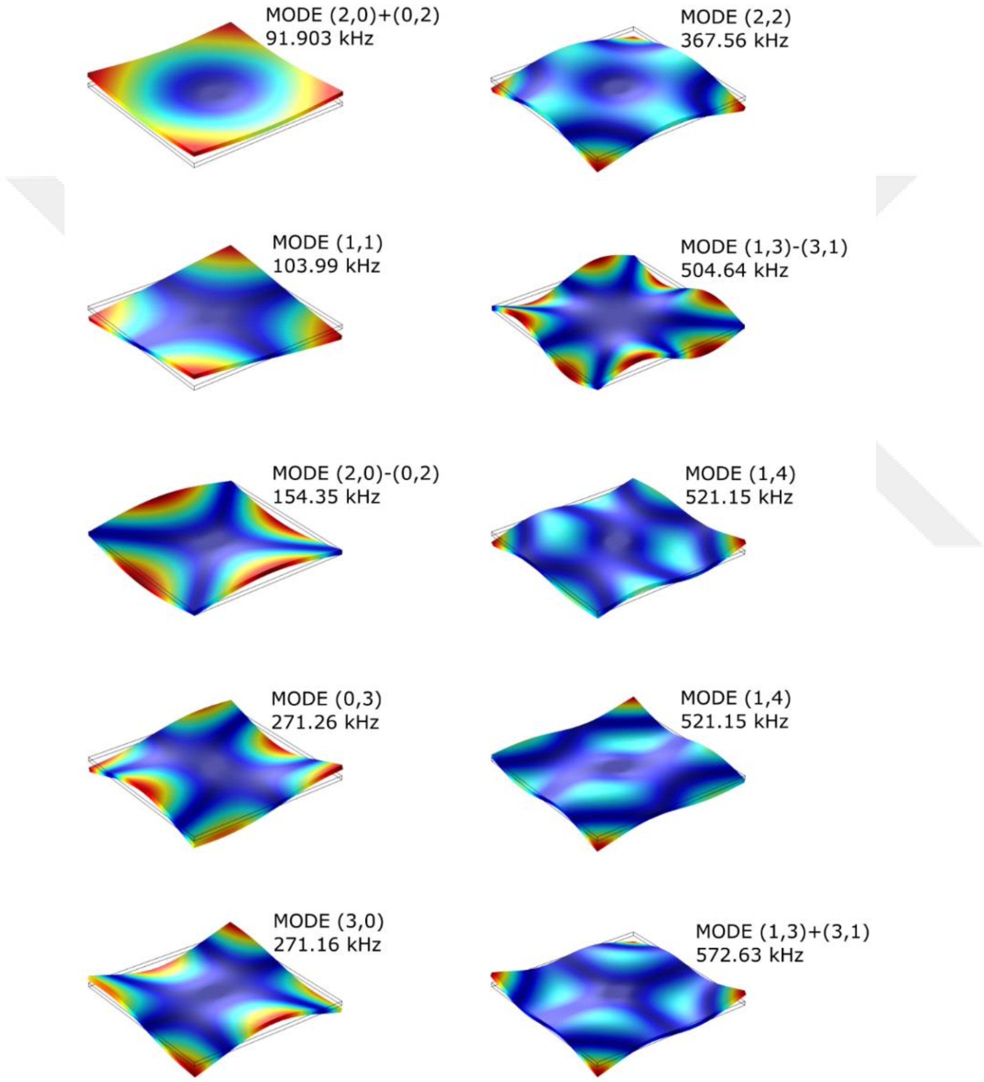

Figure 2.11: Undamped, free vibration modal simulation results obtained via COMSOL Multiphysics for the resonant MEMS square plate with a cylindrical post support at the geometric center.

The only boundary condition in the modal analysis is the fixed surface of the post. Fixed constraint selection in the boundaries list is used to define this boundary condition. For the materials, single crystal, isotropic silicon is used for plate and silicon dioxide is used for the post with the parameters given in Table 2.1. An eigenfrequency study is conducted to model the first twenty mode shapes. Geometric nonlinearities are included in the FE model. In Figure 2.11, some of the mode shapes are given.

FE modal simulation shows both (m,n) and $(m,n)\pm(n,m)$ modes. There are mode shapes having natural frequencies very close to each other. As an example, modes (4,1) and (1,4) are called "sibling" modes, which is the result of symmetric structure of square plate resonator. Another important outcome of the modal simulations is to see the effect of post. Anchoring the plate at the nodal lines is important to decrease anchor loss by minimizing the normal and shear stresses at the anchor during oscillations. It is also verified that modes-of-interest are the only two modes having the largest area of deflection, that maximizes the signal created at the formed capacitance.

As stated, eigenfunctions of free-free beam are used in the mathematical model of plate vibrations as trial functions in Rayleigh-Ritz method, meaning that the presence of the post is not included in the model. Instead, the post is placed at the intersection of nodal lines which suppresses the effect. However, as the diameter of the post increases, the effect becomes more prominent. FE modal simulations show the effect of post more clearly. The deviation in natural frequency calculations of (1,1) mode shape is only 3.35%. For the mode shape (2,0) – (0,2), the deviation is 6.15%. This deviation can be decreased by decreasing the post diameter, since the post tries to resist to motion, the structure is more stiff and the natural frequencies obtained from analytical model is greater than the FE simulations. To make analytical model and FE simulation comparable, another modal simulation is done for the plate only; in other words, modal analysis is done for plate without the post. Undamped, free natural frequencies of modes (1,1) and (2,0) – (0,2) are found to be 100057.752 Hz and 145981.065 Hz, respectively. These values correspond to deviation of 0.65% and 0.72% for the modes-of-interest. This FE modal simulations reveals the effect of post and validates the analytical model derived using Rayleigh-Ritz method.

2.4.3. Finite Element Model Simulations of the Electrostatic Effect

For this FE modelling, an electromechanical simulation is done just in the cases of static deflection, but this time simulation is done for the modal analysis. Three dimensional (3D) geometry of the thermal sensor is drawn in SIEMENS Unigraphics software and then it is imported to COMSOL environment. For the physics definitions, all of the bodies, i.e. plate, post and electrodes, are defined as linear elastic materials with the material properties given in Table 2.1. Electrodes underneath the plate are fixed using fixed constraint in the domains selection, since all electrodes are three dimensional bodies. In addition to mechanical boundary conditions, there are also electrical boundary conditions The plate is applied a proof mass voltage of 0-40V range with the selection of terminal and type of the terminal is selected as voltage. As mentioned before, applied AC voltage to the electrodes is very small in magnitude compared to proof mass voltage. Therefore, in the modal analysis simulations, electrodes are grounded. The capacitive gap between plate and electrodes is filled with a material having relative permittivity of unity representing the vacuum.

The mesh dimensions and types are exactly same as the previous FE simulation. For the solution, both stationary and prestressed eigenfrequency studies which utilize the electromechanics as physics interface is used. The analytical model of electrostatic softening is given for both single electrode and exact trapezoidal electrodes. To validate the approach used in the analytical model, FE simulations of both cases is done and the results are presented in Figure 2.12 and Figure 2.13.

Effect of electrostatic softening on the natural frequency of mode (1,1) in the analytical model perfectly agrees with the FE simulations for the single electrode layout that is a single square electrode underneath the plate. Moreover, results are in well agreement for the proof mass voltage values smaller than 20V for the trapezoidal electrode layout as seen in Figure 2.13. This results validate the method used to drive closed form equation for electrostatic softening effect for the square plate resonators.

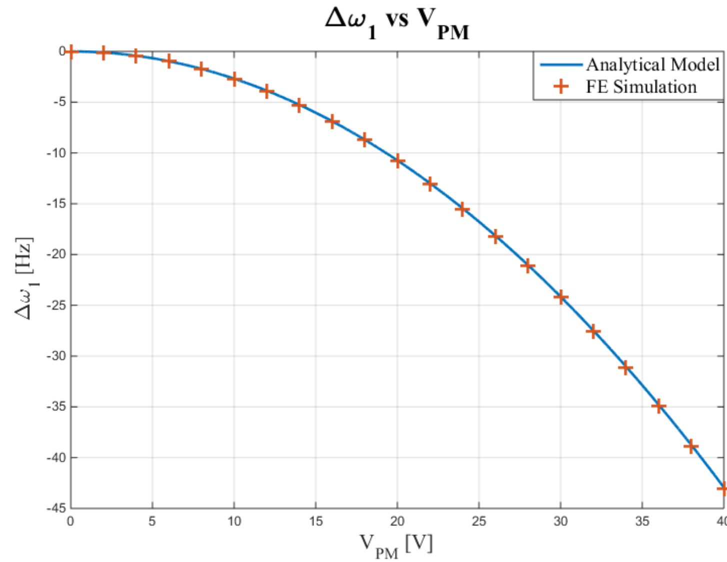

Figure 2.12: Effect of electrostatic softening on the natural frequency of mode (1,1) with analytical model and FE simulation for a single piece of square electrode fully covering the area underneath the plate.

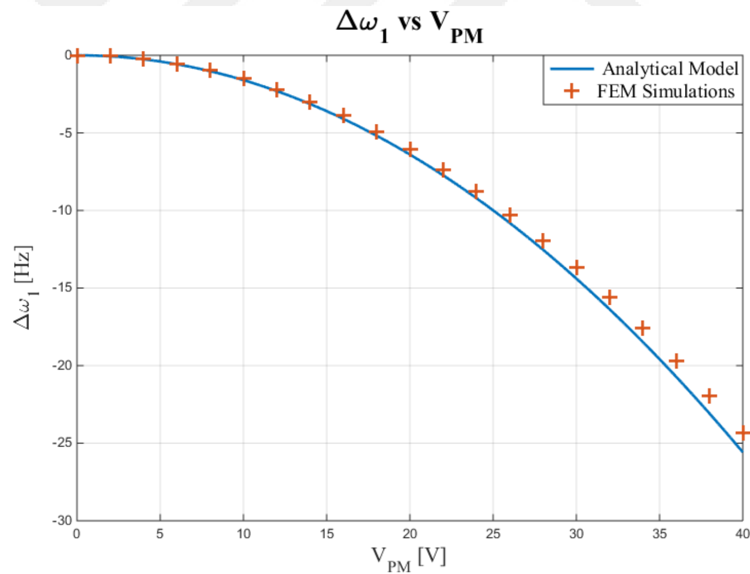

Figure 2.13:Effect of electrostatic softening on the natural frequency of mode (1,1) with analytical model and FE simulation for trapezoidal electrode layout.

It is also observed that electrostatic softening shifts the natural frequency of mode (1,1) by 3.6 Hz for applied proof mass voltage of 15V in both analytical model and FEM simulations.

2.4.4. Finite Element Model Simulations of the Thermal Effect

The analytical model of the temperature effect on the modes-of-interest shape is validated with FE simulation. For this FE modelling, an electromechanical simulation is done just in the cases of static deflection and modal analysis, but this time linear elastic materials have thermal expansion nodes.

For the physics definitions, all of the bodies, i.e. plate, post and electrodes, are defined as linear elastic materials with the material properties given in Table 2.1 having thermal expansion nodes. All of the mechanical boundary conditions are same as before. The plate is applied a proof mass voltage of 15V. As mentioned before, applied AC voltage to the electrodes is very small in magnitude compared to proof mass voltage. Therefore, in the thermal simulations also, electrodes are grounded. The capacitive gap between plate and electrodes is filled with a material having relative permittivity of unity representing the vacuum.

Same mesh size and type as before is utilized for thermal simulations. The temperature distribution in the vibrating plate is assumed to be uniform. A thermal response simulation is conducted to obtain thermal time constant. As described before temperature of a substance in contact with the sensor is determined. Figure 2.14 shows the time domain response of the designed sensor placed on top of a hotter substance.

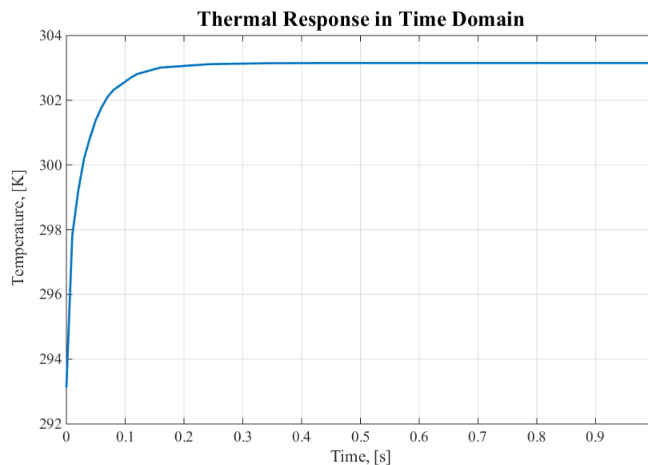

Figure 2.14: Time domain response of the designed resonant MEMS plate temperature sensor.

The time constant is around 0.1-0.125s showing that the sensor can be used as temperature detection for the applications where temperature change occurs in periods larger than 0.1-0.125s. Comparison of the derived analytical and FE simulation is given in Figure 2.15. The analyzed range of temperature difference is limited to 22-66 °C, since the test setup is capable of change the sensor that much.

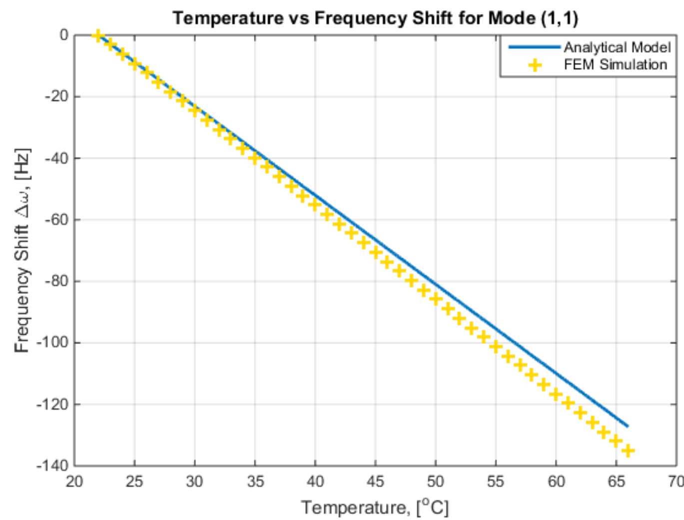

Figure 2.15: Comparison of frequency shifts due to temperature change for the derived analytical model and FE model for mode (1,1) with 15V proof mass applied.

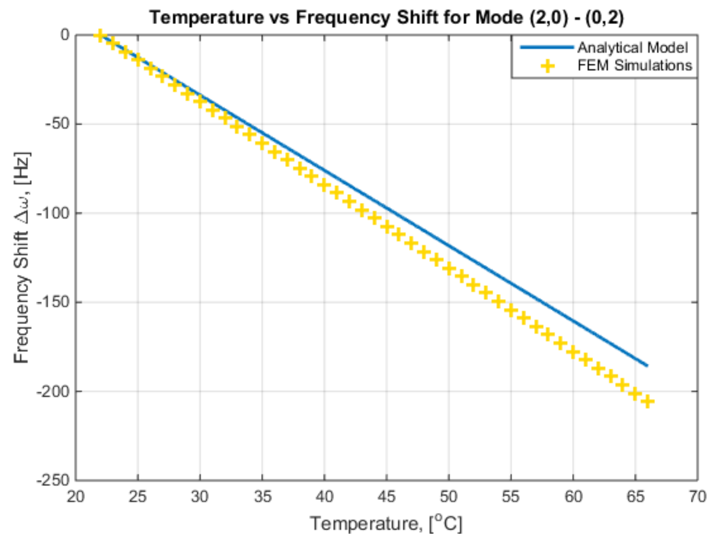

Figure 2.16: Comparison of frequency shifts due to temperature change for the derived analytical model and FE model for mode (2,0) - (0,2) with 15V proof mass applied.

As seen, results of both analytical and FE models are very close to each other for the small temperature differences for mode (1,1). However, as the temperature difference increases, the two models deviate from each other, but one should note that the deviation is less than 1 % at the maximum value of 44 °C temperature difference. For the mode (2,0) - (0,2), the discrepancy between the analytical model and FE simulations gets bigger as the temperature increases. However, for the small temperature differences, these model support each other. One of the reasons of the discrepancy of the between the analytical model and FE simulations for both modes is the fact that the plate and the post have different material having different thermal expansion coefficients. Therefore, upon the presence of temperature difference, strains built on them are different, which creates an internal stress in both them [31]. This stress is not included in the analytical model.

2.5. Summary

In this chapter, both analytical and finite element modelling of resonant based MEMS plate temperature sensor is presented. Basic concepts in vibration theory of thin plates are provided. The proposed application is explained in detail with dimensions and design concerns. The kinematics of vibration, equation of motion, is investigated in detail. Additionally, solution of EOM is provided using Rayleigh – Ritz method. Moreover, electrostatics of the sensor is given in the subsections of electrostatic driving and sensing technique. As one of the important contributions of this study, electrostatic softening effect on the natural frequencies of modes-of-interest are presented for plate resonators. Corresponding closed form equations are given. Thermal effect on the natural frequencies are included on top of the electro mechanic analytical model. Later, each and every analytical model is validated with FE simulation. In the last section, comparison of analytical and FE model is given. All possible reasons of dispersions between analytical model and FEM simulations are underlined.

CHAPTER 3

FABRICATION AND CHARACTERIZATION EXPERIMENTS OF RESONANT MEMS PLATE TEMPERATURE SENSOR

In this chapter, the fabrication and characterization experiments of resonant MEMS plate temperature sensor are presented. MEMS devices are fabricated in clean rooms due to the fact that any contamination may result in malfunctioning in the device. In Section 3.1, microfabrication flow of resonant MEMS plate temperature sensors is explained. In the subsections, details of the fabrication flow and SEM images of the fabricated devices are presented. Section 3.2 explains the frequency response characterization test setup and results. In this section, frequency responses of the modes-of-interest, result of Laser Doppler Vibrometer experiment and electrostatic softening effect tests are presented. The acquired data from the experiments is compared with the analytical model and FE simulations. In the Section 3.3, system level temperature tests are given. As a subsection, system level experimental setup is explained and the results are presented in the upcoming subsection. Frequency stability analysis is done for the system level temperature test results. Finally, Section 2.5 gives the summary of the chapter in a nutshell and gives the characteristic values of the developed temperature sensor.

3.1. Fabrication of Resonant MEMS Plate Temperature Sensor

For the fabrication of resonator plates, the advance MEMS (aMEMS) process is used, which is a high-yielding and reliable silicon on insulator (SOI) based microfabrication technique developed at the METU-MEMS Research and Application Center. Two

wafers are used in the fabrication; substrate wafer (glass wafer) and device wafer (SOI wafer). The two wafers are bonded with anodic bonding after patterning. Then sensor structures are obtained after removal of handle and buried oxide layers of SOI wafer.

3.1.1. Microfabrication Process Flow

Microfabrication starts with an SOI wafer having 35μm thick device layer (Figure 3.2 (a)). Device layer of SOI wafer is patterned to form sensor structure using deep-reactive-ion-etching (DRIE). This step is visualized in Figure 3.2 (b). The patterned SOI wafer is ready to be bonded after a piranha cleaning. As a substrate, glass wafer is used (Figure 3.2 (c)). Device layer of the SOI wafer is bonded on top of parts which are plate post and the anchors defined on the glass wafer, as seen in Figure 3.2 (d). Plate post and anchors are formed with etching using hydrofluoric acid, HF, solution. Metal wires and electrodes are defined with consecutive thermal evaporation and etching steps (Figure 3.2 (e)). First chromium (Cr) layer is evaporated on top of the patterned glass wafer in order gold to stick better to the surface. Then gold (Au) is thermally evaporated on top of chromium. To pattern electrical connections, chromium and gold are wet etched in the reverse order of deposition sequence. The anodic bonding takes place after piranha cleaning of glass wafer. Bonded wafers are shown in Figure 3.2 (f). After anodic bonding, first handle layer, then buried oxide layer of SOI wafer is removed to release the suspended resonator structures (Figure 3.2 (g)).

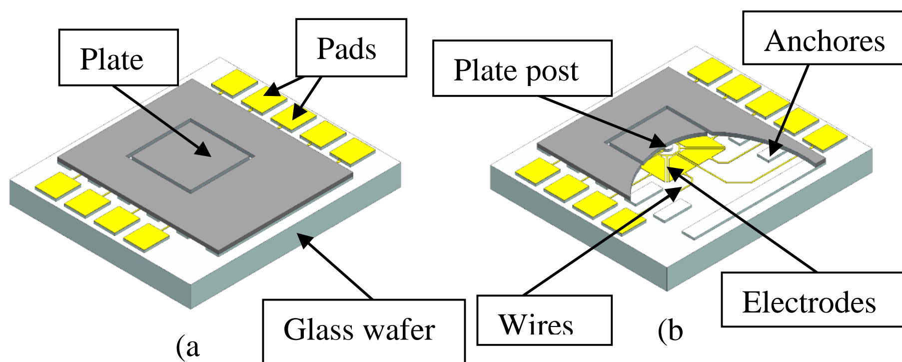

Figure 3.1: 3D solid model of designed sensor structure. (a) Shows the plate and pads. (b) A portion of the plate is removed to see post, anchors, electrodes and wires clearly.

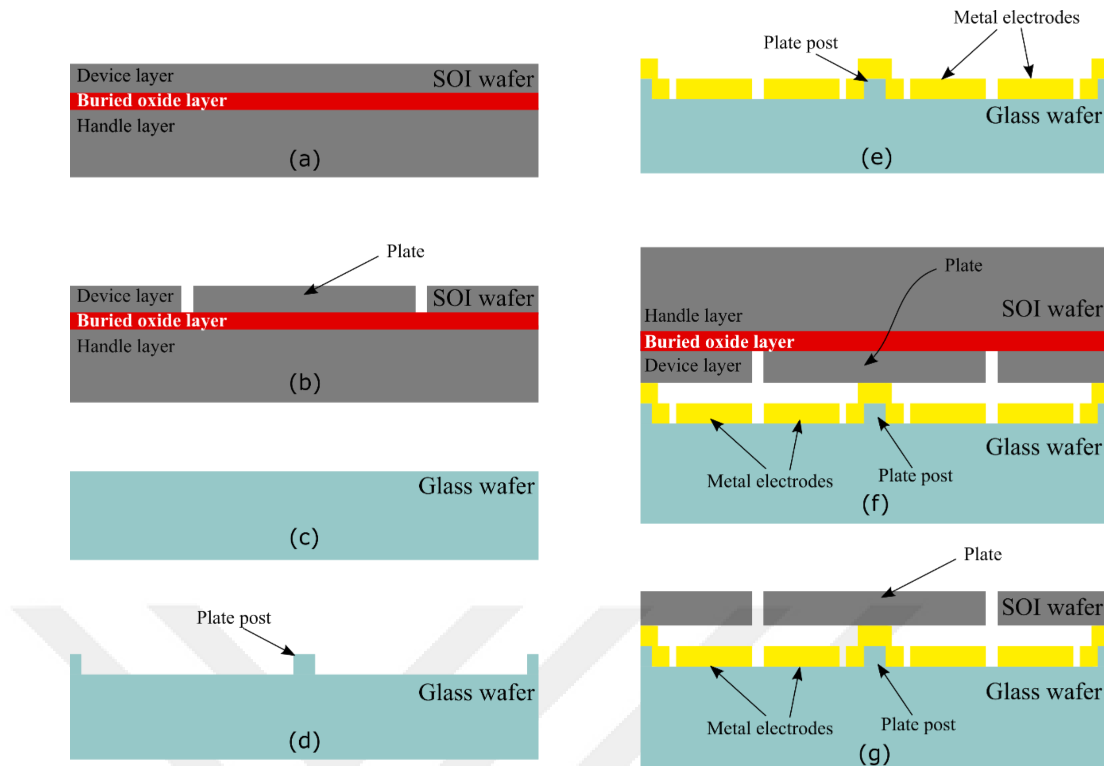

Figure 3.2: Microfabrication steps of the sensor in aMEMS process flow. Given figures are for cross-sectional views of the wafer. (a) The SOI wafer used in the fabrication. (b) DRIE of device layer of SOI wafer to obtained vibrating square plates. (c) The glass wafer used in the fabrication. (d) Wet etching of glass wafer to obtain plate post and anchors. (e) Obtained metal pattern after consecutive thermal evaporation and etching of metal. (f) Anodic bonding of the two wafers. (g) Handle and buried oxide layer of SOI wafer is removed to release the suspended structures.

The details of the fabrication process are not given here as they can be found in [31]. In addition, details of the aMEMS process are given in [53]. In Figure 3.1, the 3D solid model of the resonant MEMS plate temperature sensors drawn in SIEMENS Unigraphics is given. Figure 3.1 (a) shows the single resonant MEMS plate temperature sensors with pads used to access electrodes and proof mass. Figure 3.1 (b) shows the single sensor structure and some portion of the resonator plate is removed to see post, anchors, electrodes and wires clearly.

3.1.2. Microfabrication Results

In Figure 3.3 and Figure 3.4, scanning electron microscope images of fabricated sensors with the details of electrodes, post, plate and gap are given. The SEM images are taken at METU-MEMS Research and Application Center. In addition, resonator plate is removed in Figure 3.3 to have visual access to the electrodes.

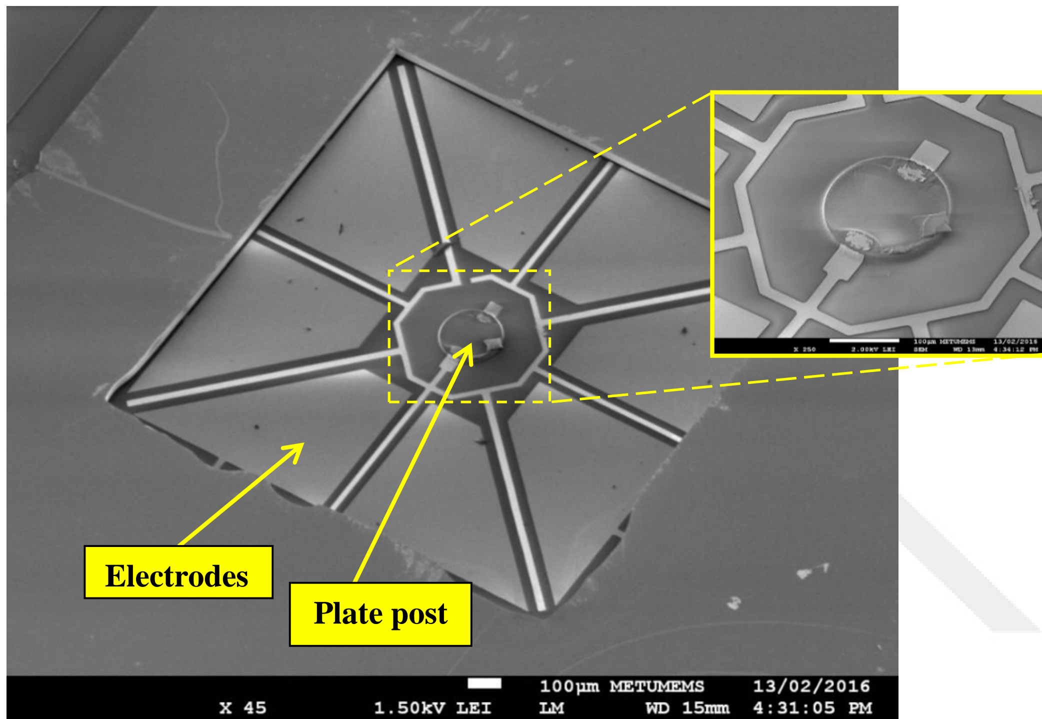

Figure 3.3: Scanning Electron Microscope (SEM) image of the fabricated sensor with the plate removed to have visual access to the electrodes and plate post.

As seen in these figures, the designed structures are well fabricated to proceed further for test; however, fabrication is not perfect. Sides of the resonator is not perfect lines, there are some undercuts which affect the natural frequency and mode shapes. Natural frequency of a square plate having smaller side lengths is greater than that of square plate having larger side lengths. Natural frequencies of the fabricated devices are expected to be greater than the calculated and simulated ones due to these undercuts making the structure stiffer in the transverse direction and effective mass less.

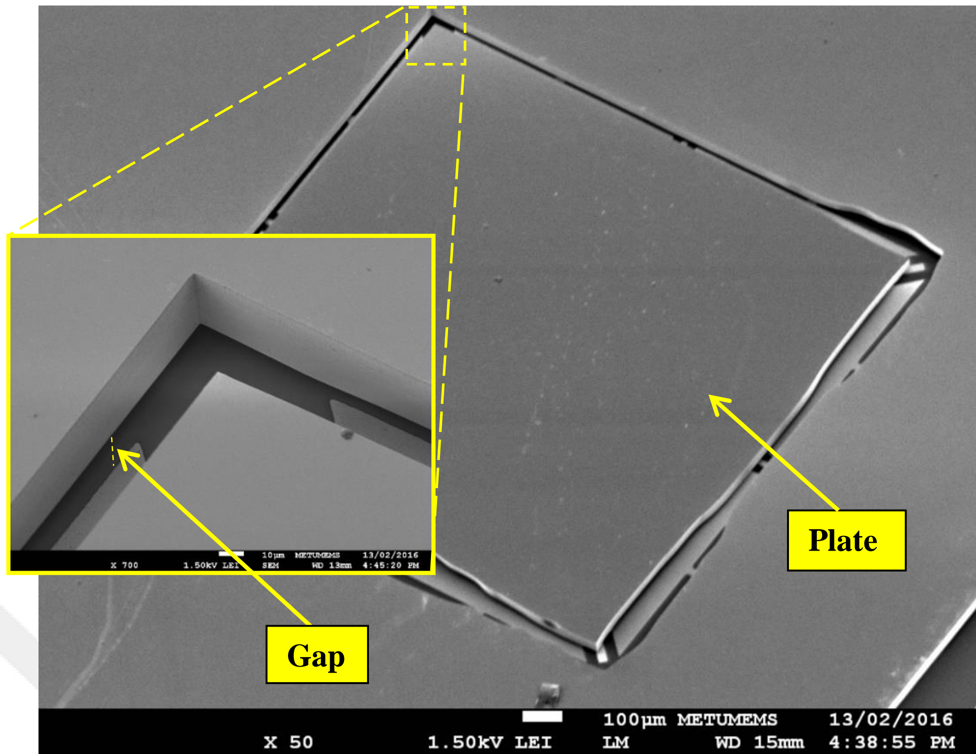

Figure 3.4: SEM image of the fabricated sensors

Another unavoidable common problem in MEMS fabrication is the contamination. It may result from both environments of the clean-room and process itself. In Figure 3.3, it is possible to observe a little contamination; however, there is no contamination observed on the surfaces of the suspended structure, the plate. It is important to have clean moving parts and electrodes, since they affect the displacement and generated force and read signals.

3.2. Frequency Response Characterization Tests

For the purpose of verification of the validated analytical model with FE simulations, frequency responses of the fabricated MEMS resonators are measured in a vacuum chamber at a vacuum level of around 20mTorr. Laser Doppler Vibrometer tests are held to verify closed form equations for both natural frequency and corresponding mode shape.

3.2.1. Frequency Response Test Setup

The experimental setup for frequency response tests composes of vacuum pump, vacuum chamber, vacuum level indicator, trans-impedance amplifier circuitry (TIA) and device under test (DUT). Experimental setup is given in Figure 3.5.

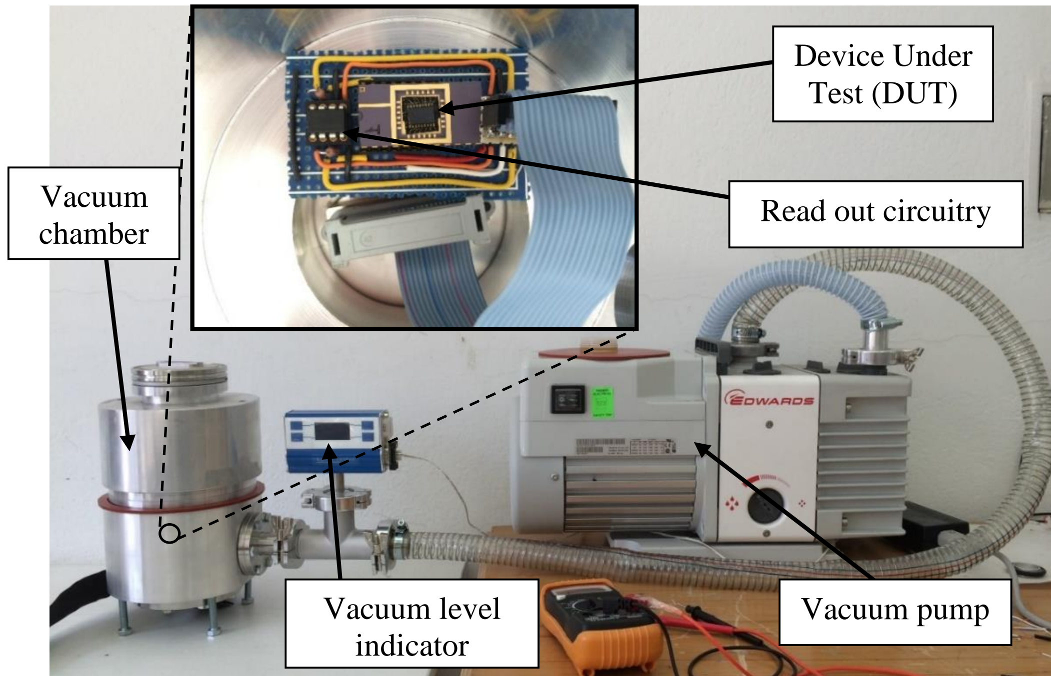

Figure 3.5: Experimental setup for the frequency response test of fabricated MEMS plate resonator.

In all of the experiments in this study, Agilent E5061B Network Analyzer is used to drive the resonators by applying AC voltage and used to collect response data to draw frequency response plots (Bode plots). As seen in the experimental setup, TIA is placed close vicinity of the resonator in order to minimize the feedthrough (stray) capacitance. A trans-impedance amplifier with 1 MΩ feedback resistance is used for characterization of the plate resonator. There are eight electrodes underneath the plate, which enables to drive several modes in single design. For testing (1,1) mode shape, corresponding electrode layout for driving and sensing is given in Figure 3.6 together with network analyzer and TIA. For DC voltages supplied to op-amps, Agilent E3631A Power Supply is used.

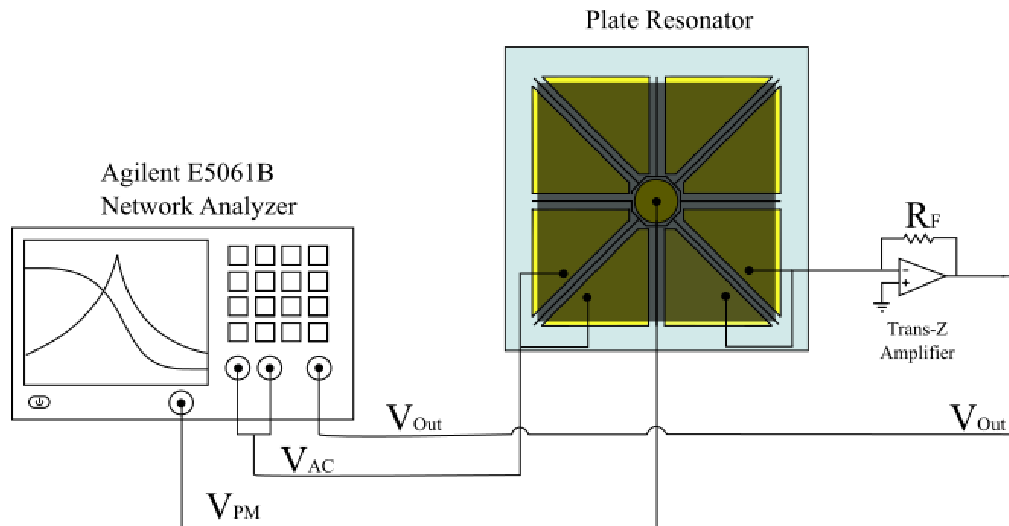

Figure 3.6: Read out circuitry used in frequency response tests of mode shape (1,1) of MEMS plate resonator together with network analyzer.

Frequency response tests are held at 20mTorr ambient pressure. Driving signals are applied to the corresponding electrodes for each mode shape and applied AC voltage has a magnitude of 100mVpp (peak to peak). Current pumped out from the sensing capacitance is converted to voltage with the TIA utilizing LF353 operational amplifier by Texas Instrument. For proof mass voltage, 15V DC voltage is applied to mass of the resonating body. Mechanical response of the resonator is measured by subtracting stray response from overall response. In other words, the frequency response is collected with 15V proof mass voltage and logged in the network analyzer. Then, proof mass of the resonator is grounded. The data called as stray or feedthrough data is collected. These two logged data are subtracted from each other in the complex domain and mechanical response is obtained. This subtraction is done on a separate computer using MS Excel and/or MATLAB. Final frequency response is plotted utilizing one of these two commercial software.

3.2.2. Frequency Response Test Results

Frequency responses of modes-of-interest are obtained with the test procedure explained previous section. To locate the frequency of each mode shapes, first, frequency response of the resonator is taken for a very large frequency span. From 0

Hz to 200 kHz, response is collected and following results are obtained. After located each mode shape, response is recollected in smaller frequency span of 100-200 Hz.

At around 65 kHz, two distinct mode shapes are captured which are not modelled in the modelling section. These mode shapes are actually pitch and roll of the plate around the axis passing through the center and parallel to x and y, respectively. The given frequency response in Figure 3.7 shows these modes in the frequency range of 63-68 kHz.

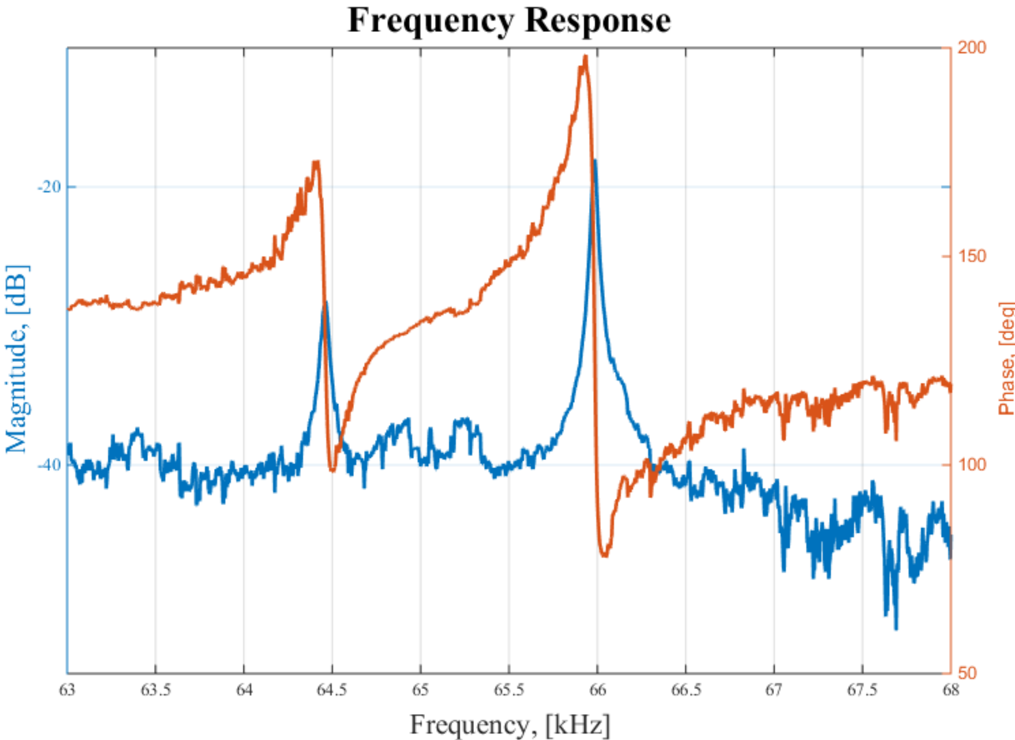

Figure 3.7: Frequency response of MEMS plate resonator at 20mTorr vacuum level with 15V proof mass voltage in the frequency span of 63-68 kHz shows the pitch and roll motion of the plate around the axis passing through the post and parallel to x and y axis, respectively.

The pitch and roll motion are expected to be at the same frequency, since the square plate structure is symmetric about its center. However, the fabrication imperfections mentioned in the previous section causes these modes to separate. The amount of

separation in terms of frequency is very small. One of these modes is at 64.46 kHz and the other mode shape is at 65.98 kHz.

The measured frequency response of mode (1,1) at 20mTorr ambient pressure with proof mass voltage of 15V is given in Figure 3.8.

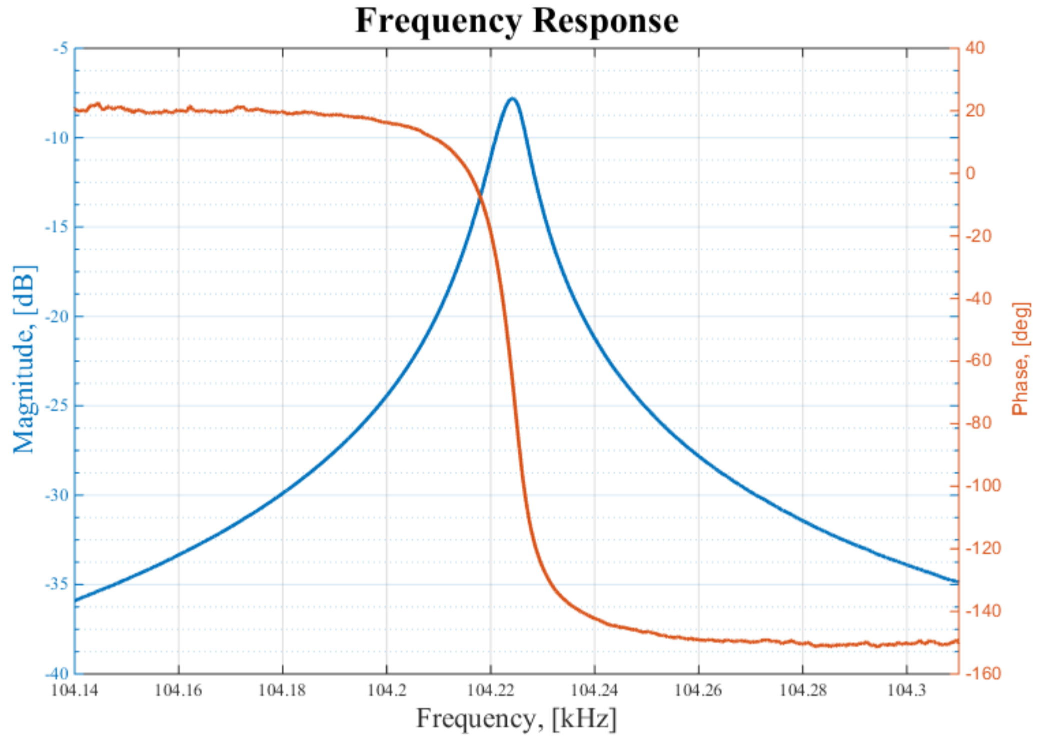

Figure 3.8: Frequency response test result of mode (1,1) of fabricated MEMS plate resonator at 20mTorr vacuum level with 15V proof mass voltage.

As expected, resonance frequency of mode (1,1) is in good agreement with the analytical model and FE simulations. Natural frequency of mode (1,1) is measured to be 104.225 kHz with a Q-factor around 14300. Quality factor is one of the key properties of the resonators but not only. In terms of Q-factor comparison, resonator in this study is placed at a good point among the ones in literature. Differences in frequency between analytical model and test results are originated from facts that:

1. Analytical model does not take post into account. It is discussed that post increases the transverse stiffness of the plate resulting higher natural frequencies.

2. Fabrication imperfections such as undercut effect the geometry of the plate. Natural frequency of the plate is inversely proportional to side length of square plate and directly proportional to thickness of the plate. Therefore, undercuts increase the natural frequency as measured in this study.

In addition to mode (1,1), result of analytical model and FE simulations are also verified with frequency response tests for mode (2,0) – (0,2). Figure 3.9 shows the frequency response of mode (2,0) – (0,2) at 20mTorr vacuum level with 16V proof mass voltage.

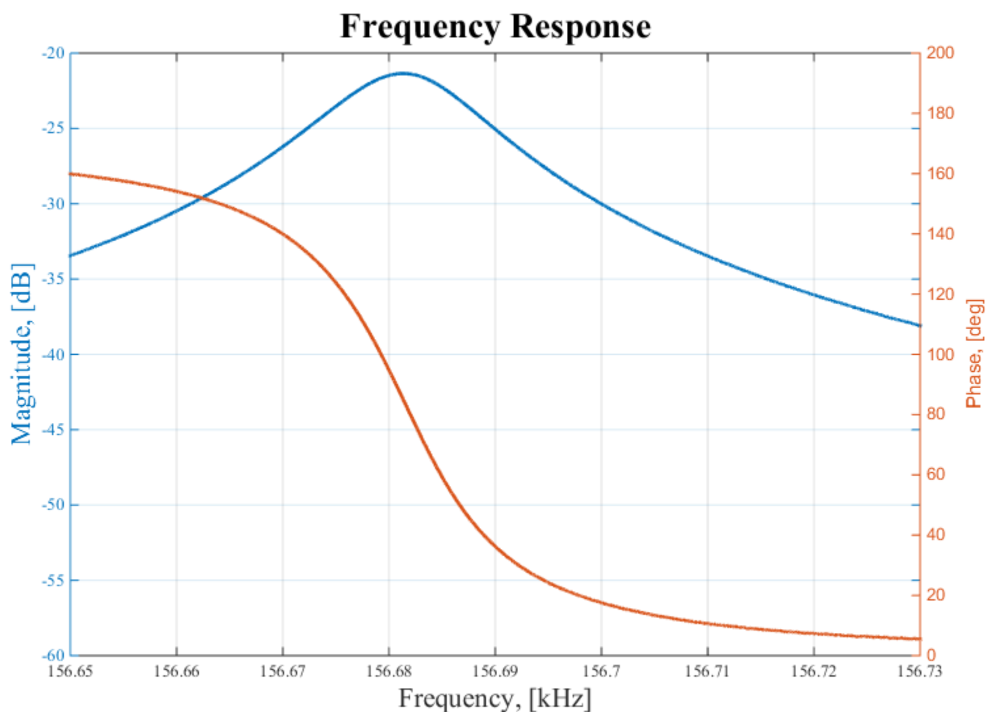

Figure 3.9: Frequency response test result of mode (2,0) - (0,2) of fabricated MEMS plate resonator at 20mTorr vacuum level with 16V proof mass voltage.

As expected, resonance frequency of mode (2,0) – (0,2) is also in good agreement with the analytical model and FE simulations. Natural frequency of mode (2,0) – (0,2) is

measured to be 156.682 kHz with a Q-factor around 10700. The differences between models and tests result from exactly same arguments made for mode (1,1).

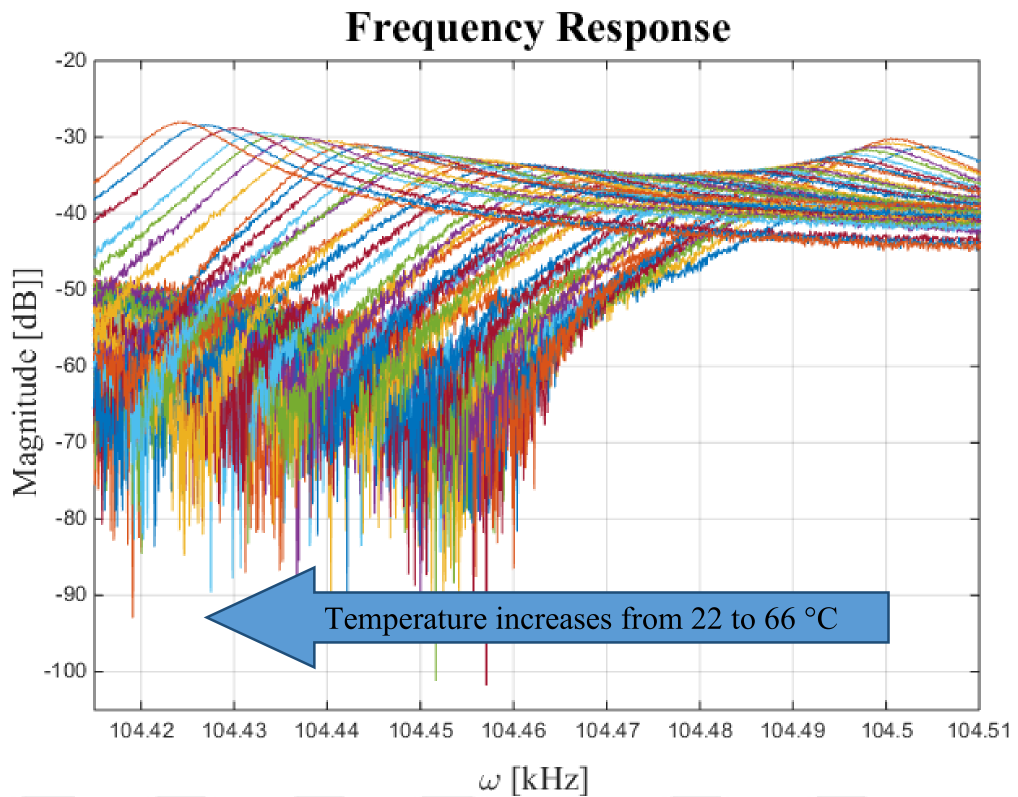

Figure 3.10: Frequency response of the fabricated resonator at 20mTorr ambient pressure with 15V proof mass voltage between 22-66 °C

In addition to identification of mode shapes, temperature effect on (1,1) mode is also tested. The Figure 3.10 shows the frequency response of the fabricated resonators at vacuum level of 20mTorr with 15V proof mass voltage. The frequency response test with changing temperature of the resonator is repeated for increasing and decreasing temperature. As a result, Figure 3.11 is obtained.

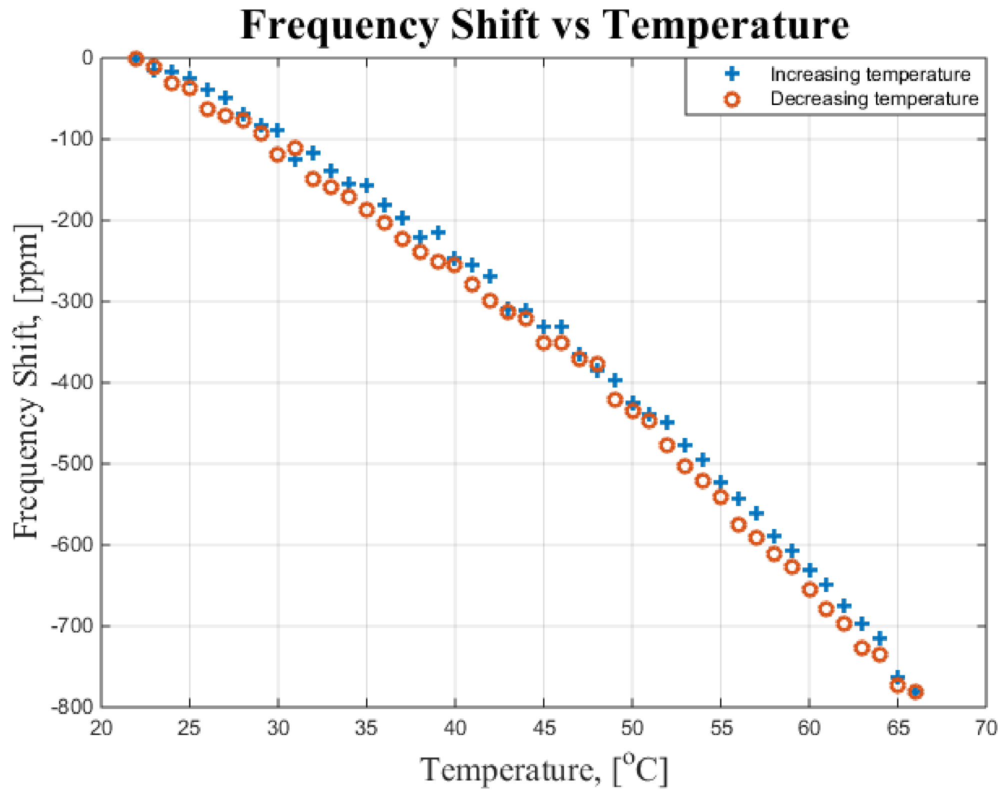

Figure 3.11: Frequency response of the fabricated resonator with changing temperature from 22 to 66 °C at 20mTorr ambient pressure. The proof mass voltage is 15V. Both increasing and decreasing cases are presented.

Frequency shift is given as parts per million (ppm) over the temperature range of 22 – 66 °C. Note that, the given response is the mechanical response of the resonator, meaning that feedthrough capacitance is subtracted from the overall response. It is seen that both increasing and decreasing case show similar response.

3.2.3. Laser Doppler Vibrometer Test Results

Laser Doppler Vibrometer (LDV) tests are carried out to verify mathematical model for both natural frequencies and corresponding mode shapes. In addition, all of the mode shapes are scanned between 0-175 kHz frequency range to locate the parasitic modes. Frequency response of the plate at vacuum level of 0.364mTorr with 15V proof mass voltage is measured with Ploytec micro system analyzer MSA – 500 Scanning Laser Doppler Vibrometer. Figure 3.12 shows the measured response.

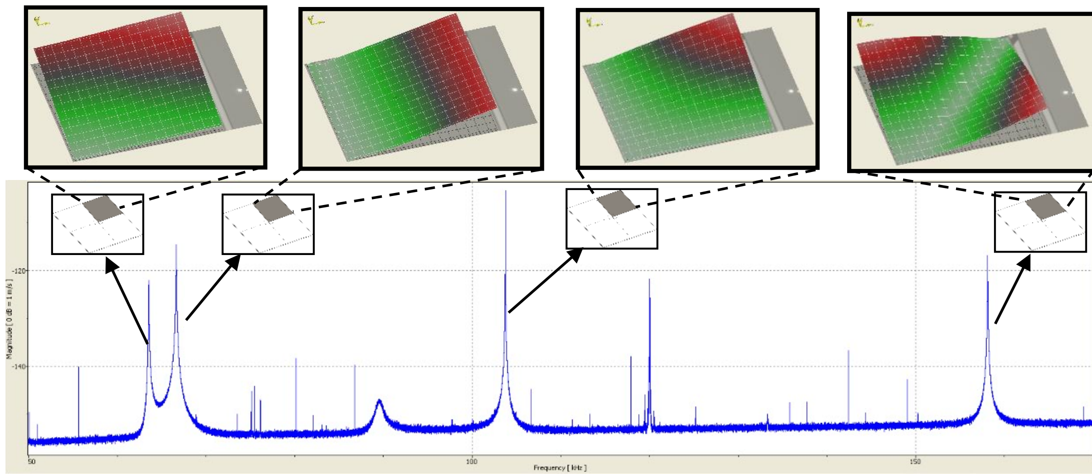

Figure 3.12: Frequency response of the plate at vacuum level of 0.364mTorr measured with Ploytec micro system analyzer MSA - 500 Scanning Laser Doppler Vibrometer between 0-175 kHz frequency range at 0.364mTorr vacuum pressure level with 15V proof mass voltage. Mode shapes are measured for the one quarter of the plate due to optical capabilities of the measurement device.

Notice that presented mode shapes in Figure 3.12 show only one quarter of the plate due to optical capabilities of the measurement device. As a result of overall comparison, the measured values of natural frequencies for modes-of interests are close to analytical model and FE simulations.

First two peaks which are very close to each other around 65 kHz are the pitch and roll of the plate around post which were also observed in frequency response tests. These modes are at 63.65 kHz and 66.65 kHz, respectively. Differences in vacuum level, measuring technique and circuitry used in these tests cause slight discrepancy in natural frequencies between frequency response and LDV tests. Once more, these pitch and roll modes are expected to be at the same frequency for completely symmetric structure. However, fabrication imperfections distort the symmetric and separate them. Third peak in the LDV results corresponds to mode (1,1) at 103.76 kHz and last peak shown is the natural frequency of mode (2,0) - (0,2) at 158.1 kHz.

3.2.4. Electrostatic Softening Effect Test Results

Verifying the analytical model and FE simulations of natural frequencies and mode shapes model, the analytical model of electrostatic softening effect is also tested and verified. In the modelling chapter, electrostatic softening effect is analyzed for two cases: single square electrode layout and trapezoid electrode layout. Analytical model of the softening effect for single square electrode layout case is validated with FE simulation; however, it is not verified with test results, since single electrode layout is not fabricated. This is done to be sure the validity of the method used. On the other hand, electrostatic softening effect for trapezoidal electrode layout is tested also. Figure 3.13 shows the electrostatic effect for proof mass voltage of 0-40 V range, verifying the validity of the method to find electrostatic spring constant. Tests are done at 20mTorr ambient vacuum pressure level. The results are published in [54].

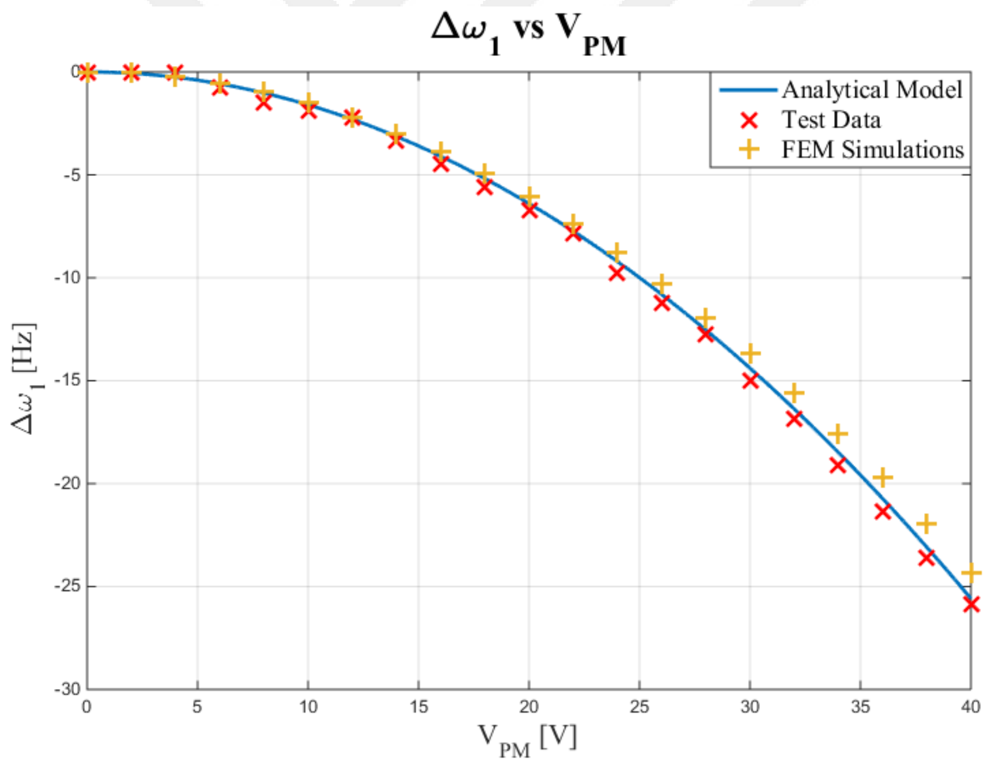

Figure 3.13: Test results of electrostatic softening effect on the natural frequency of mode (1,1) with analytical model and FE simulation for trapezoidal electrode layout at 20mTorr ambient vacuum pressure for proof mass voltage of 0-40V.

3.3. System Level Temperature Tests

As described in the proposed application section, temperature of the resonator plate shifts the natural frequencies. To be able to detect the frequency shift, a closed loop controller is implemented to keep the MEMS plate in resonance. If the resonance frequency shifts, the controller should follow that shift and drive the plate at the new resonance frequency. That driving signal, input, of the plate is generated from voltage controlled oscillator (VCO).

One of the methods used as a closed loop controller for resonance in oscillators is Phase Locked Loop (PLL). Phase difference between the input and output of the resonator is measured by the PLL and this is fed to the controller as an error signal. The controller adjusts the input voltage of the VCO which generates the input signal having adjusted frequency for the resonator.

The error signal for the controller is generated by multiplying the drive and sense signal. If these two signals have same frequency but different phase, then the multiplication gives:

$$A\sin(\omega t)B\sin(\omega t-\Phi)=\frac{1}{2}AB\left[\cos(\Phi)-\cos(2\omega t-\Phi)\right] \quad (3.1)$$

Multiplication results a DC term and a double frequency term. Notice that the DC terms is composed of only cosine of the phase angle. Therefore, one can extract the phase information filtering out the double frequency term using a low pass filter (LPF). From the basics of control theory, controllers try to make error signal, cosine of the phase angle in this case, zero. Cosine of an angle zero if and only if the angle equals to $\pi/2$ or $3\pi/2$. Due to the known fact that input of the TIA is derivative of the resonator output signal, the output of TIA is shifted by $\pi/2$.

If the frequencies of the signals are not equal, then the multiplication is:

$$A\sin(\omega_1 t)B\sin(\omega_2 t-\Phi)=\frac{1}{2}AB\left[\cos((\omega_1-\omega_2)t+\Phi)-\cos((\omega_1+\omega_2)t-\Phi)\right] \quad (3.2)$$

This time the terms are separated as low frequency and high frequency term. The low frequency term is the useful part. The output of the controller fluctuates due to fluctuation in the error; however, an integral control takes care of this fluctuation due to accumulation of error [55].

In Figure 3.14, a PLL system is shown with basic components used in this thesis study.

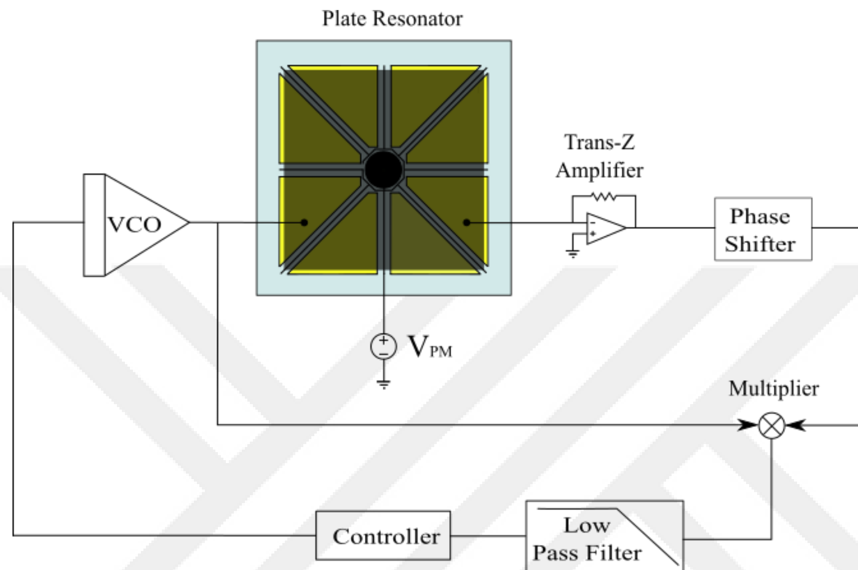

Figure 3.14: The PLL controller with its main elements that are VCO, plate resonator, TIA, phase shifter, multiplier and controller used in this study.

Frequency change is tracked with the PLL controller. The fabricated sensors are placed in the vacuum chamber on top of a thermoelectric cooler (TE cooler) and it is heated up and cooled down with the TE cooler. The temperature data is collected with a commercial temperature sensor LM35 produced by Texas Instruments. It is placed inside the package to acquire precise measurements. Both the frequency and temperature data are logged simultaneously.

3.3.1. System Level Temperature Test Setup

In the temperature tests, same experimental setup is used with the addition of PLL controller, TE cooler, temperature sensor and data logging computer. Vacuum level

for the system level temperature tests is 0.405mTorr. The experimental setup is shown in Figure 3.15.

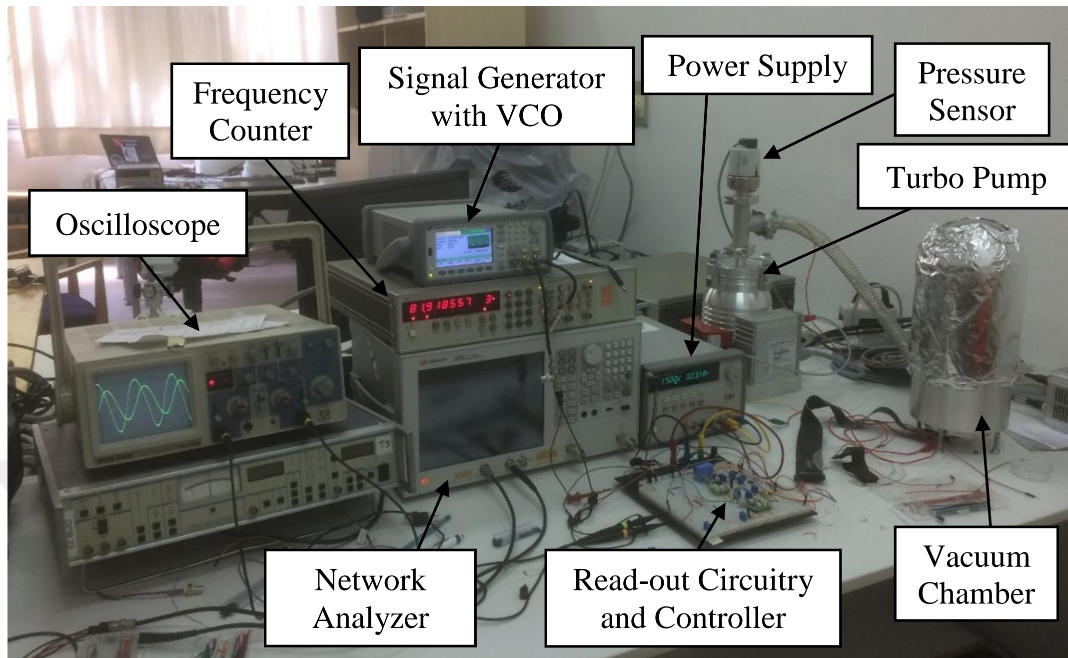

Figure 3.15: Experimental setup for the system level temperature tests showing oscilloscope, frequency counter, signal generator used as VCO, power supply, vacuum pump and chamber, network analyzer and readout circuitry.

The output of the fabricated sensor is converted to voltage with a TIA placed near the sensor inside the vacuum chamber as in the frequency response experiments. Output signal of TIA is first passed through a HPF (high pass filter) to eliminate the DC offsets if there is any and then it is amplified due to fact that multiplier input has a minimum threshold value. For the amplifier stage shown in Figure 3.16, LF353 operational amplifiers are used. The multiplier stage works as a comparator as explained in the theory of the system level tests section. Multiplication of two signals having same frequency results with a cosine term of phase difference between those signals. As seen, driving and sensing signals of the plate resonators are multiplied which are expected to have same frequency at the resonance. Therefore, multiplier is actually comparator for the circuitry given in Figure 3.16.

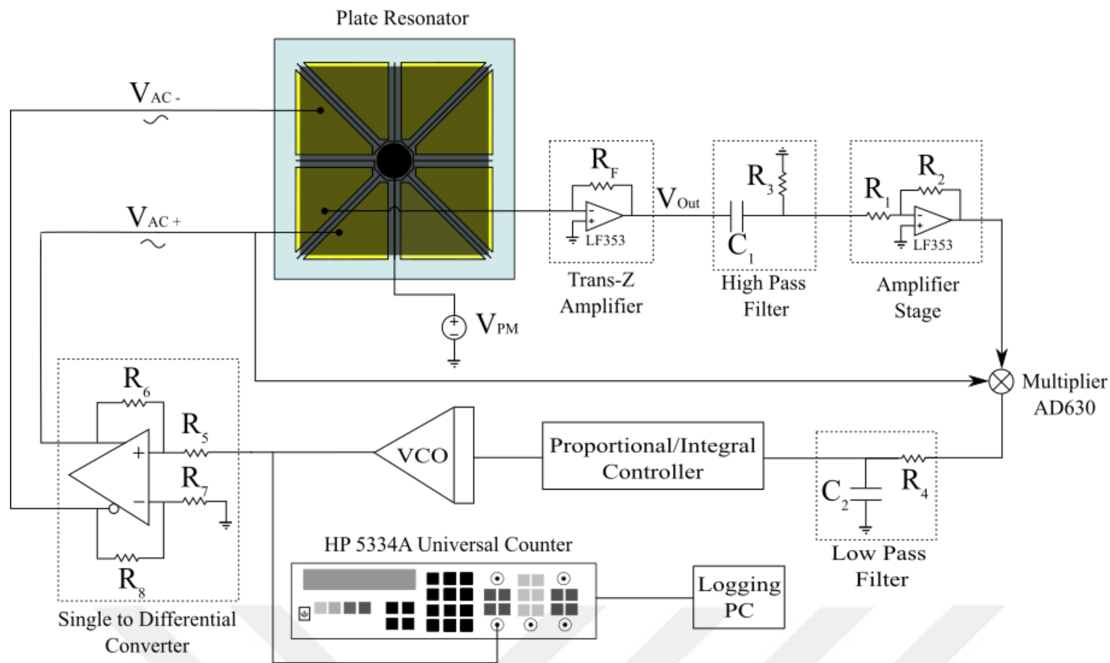

Figure 3.16: The PLL circuit shown in detail with main blocks that are , VCO, a controller, amplifier stages and a phase detector (multiplier).

AD630 is used to multiply input and output of the resonator. The output goes to the controller as error. Output of the controller change the frequency output of the Voltage-Controlled-Oscillator (VCO). A signal generator is used as a VCO. Then the generated sine signal is manipulated to get two sine signal having 180° phase difference. The fabricated plate is differentially derived to minimize the feedthrough capacitance present in the system. To differentially drive the plate resonator, the signal produced by VCO is converted into two signal having exactly same amplitude but 180° phase difference. For this purpose, single to differential converter is utilized. These two sine signals drive the plate resonator and output signal of the resonator is fed to the TIA and the loop closes. The controller forces error to be zero which corresponds to 90° phase difference between input and output of the plate resonator. As explained before, this occurs at the resonance. The frequency of the output of sine shaper is logged using HP 5334A Universal Counter.

3.3.2. System Level Temperature Test Results

System level temperature tests results are obtained with the experimental setup explained in previous section. The temperature tests are held at the vacuum level of 0.405mTorr with proof mass voltage of 42V. The commercial products of AD620 of Analog Devices and LF353 of Texas Instruments are used as instrumentation and operational amplifiers, respectively. The commercial product with the code AD630 of Analog Devices is used to multiply input and output signals of the resonator. As explained, sine shaper and VCO are combined in the Keysight 33500B Series Waveform Generator. Agilent E3631A Power supplies energize the readout circuitry and the fabricated sensors. For counting and logging frequency data, HP5443A Universal Counter with a logging computer is used. Lastly, frequency responses are collected by Agilent E5061B Network Analyzer.

The obtained response of the plate resonators with changing temperature for mode (1,1) in given in Figure 3.17.

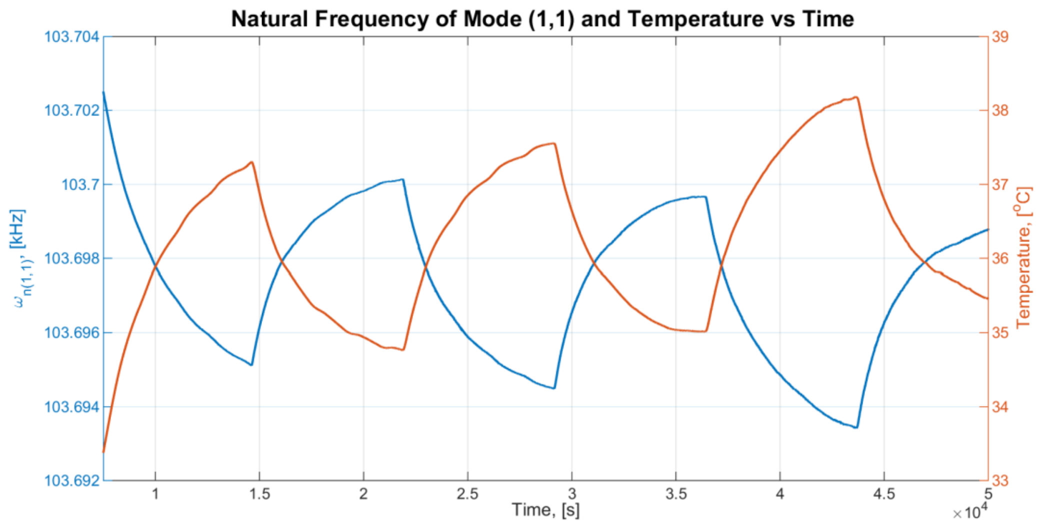

Figure 3.17: The obtained results for natural frequency of mode (1,1) of the fabricated plate resonator and its temperature vs time.

The natural frequency shift of the fabricated device with a larger temperature range is also tested and corresponding response is given in Figure 3.18.

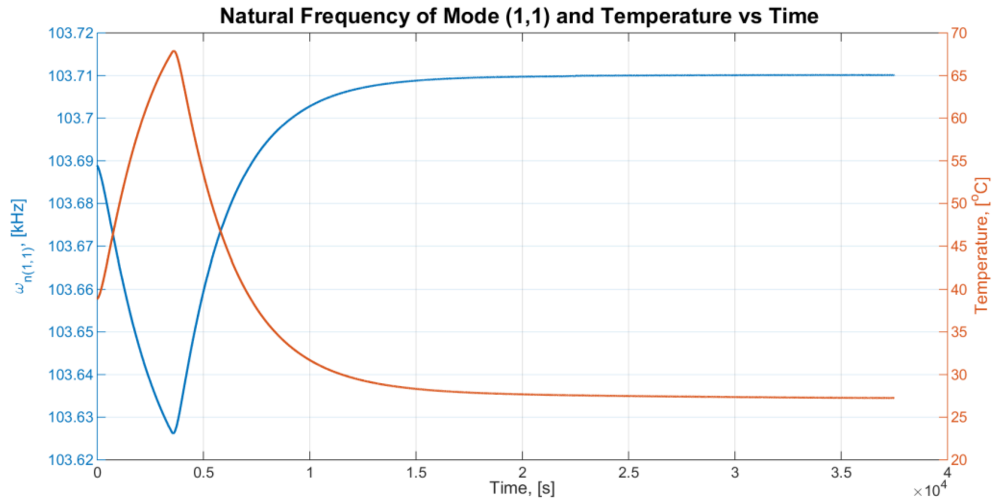

Figure 3.18: Natural frequency of mode (1,1) of the fabricated plate resonator and its temperature vs time in larger temperature range.

The scale factor for mode (1,1) is calculated to be 2.0214Hz/°C from the obtained results of system level temperature tests shown in Figure 3.19.

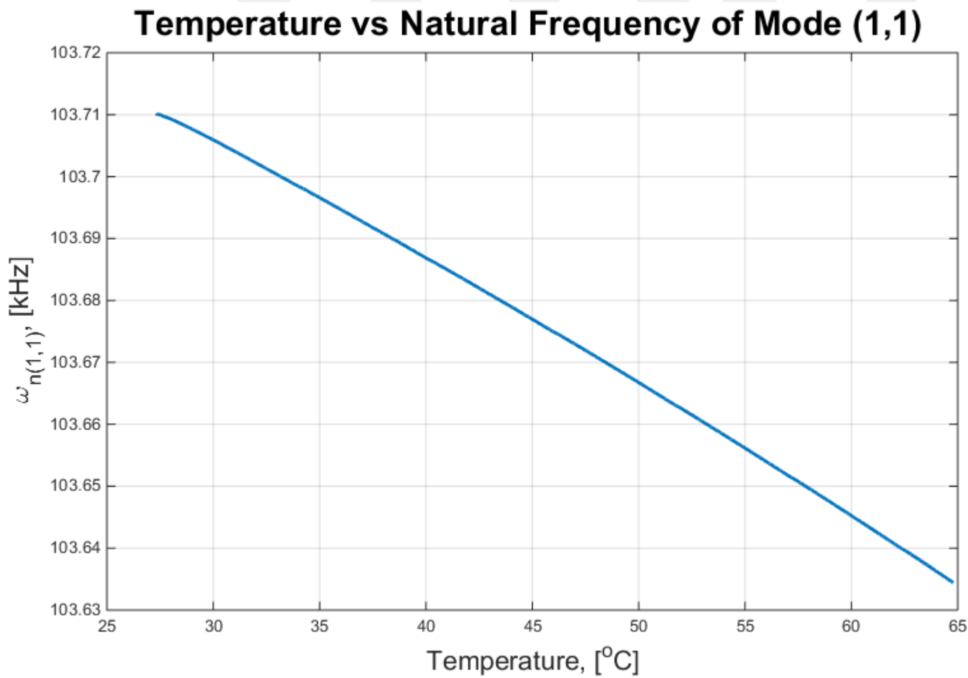

Figure 3.19: Change of natural frequency of mode (1,1) with respect to temperature.

The results are compared with the analytical model and FE simulation for the thermal effect in Figure 3.20.

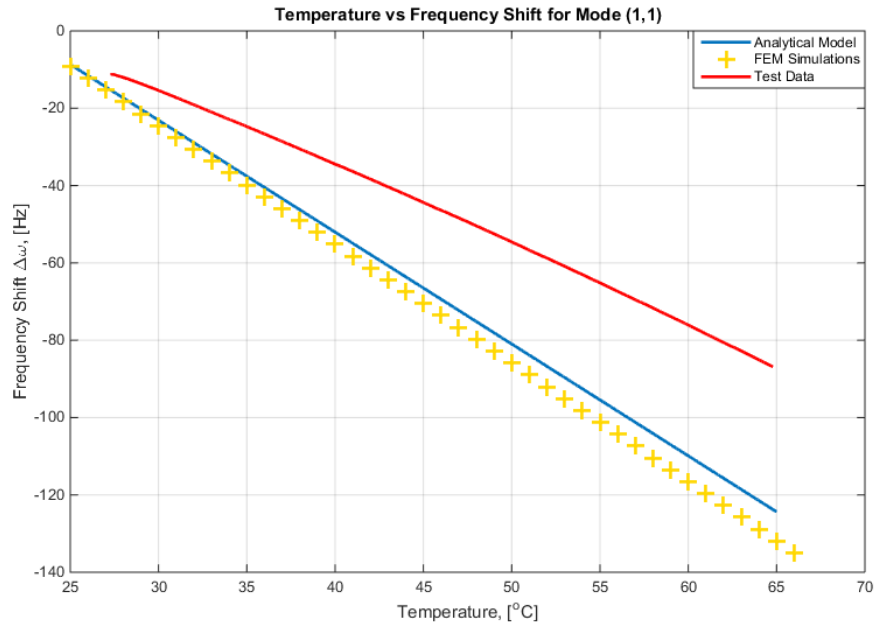

Figure 3.20: Test results of thermal effect on the natural frequency of mode (1,1) with analytical model and FE simulation for the temperature of 25-55°C.

Analytical model, FE simulations and obtained test results have same behavior. Analytical model neglects the effects of post, feedthrough capacitance and fabrication impurities; therefore, there is a discrepancy as expected. Therefore; the characterization data in the next chapter are obtained from the tests rather than model and simulations.

To experimentally determine the maximum temperature resolution, the frequency data for mode (1,1) is acquired over 50000 seconds with a sample rate of 6.01 Hz (0.17 seconds sampling time). Obtained frequency data over a time is given in Figure 3.21. It should be noted that the collected data is for sensor and PLL electronics together.

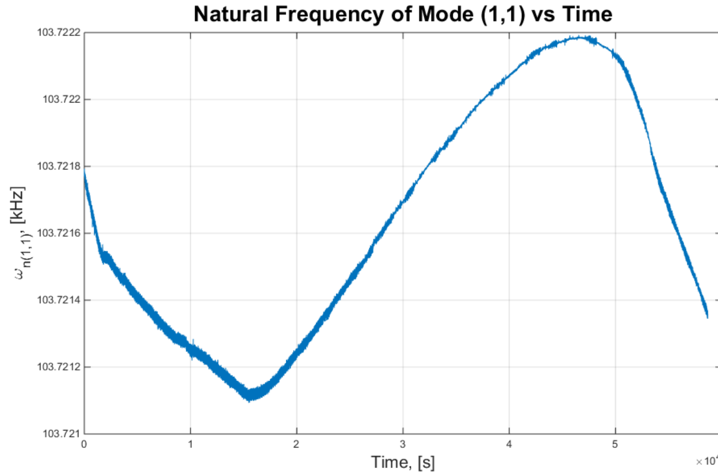

Figure 3.21: Natural frequency vs Time for mode (1,1) plot obtained from the data acquired over 50000s with a sampling rate of 6.01 Hz for the sensor and PLL electronics together.

The frequency stability analysis is done using Allan variation method [56]. The Allan variance of the drift data is given in Figure 3.22. The Allan variance analysis is concluded that resolutions as low as 0.0003725°C are obtained with an integration time of 8 seconds for mode (1,1).

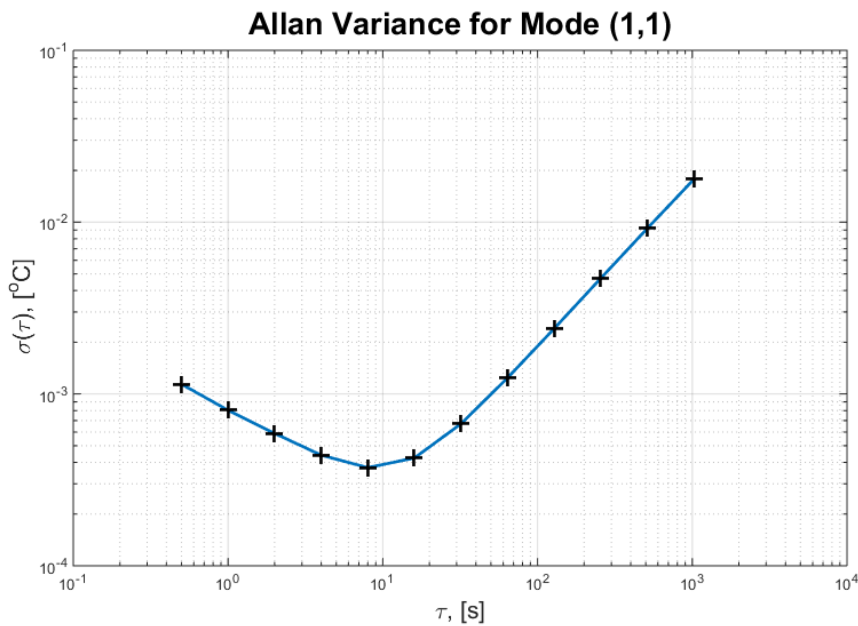

Figure 3.22: Allan variance plot for the natural frequency of mode (1,1).

The obtained response of the plate resonators with changing temperature for mode (2,0) – (0,2) in given in Figure 3.23.

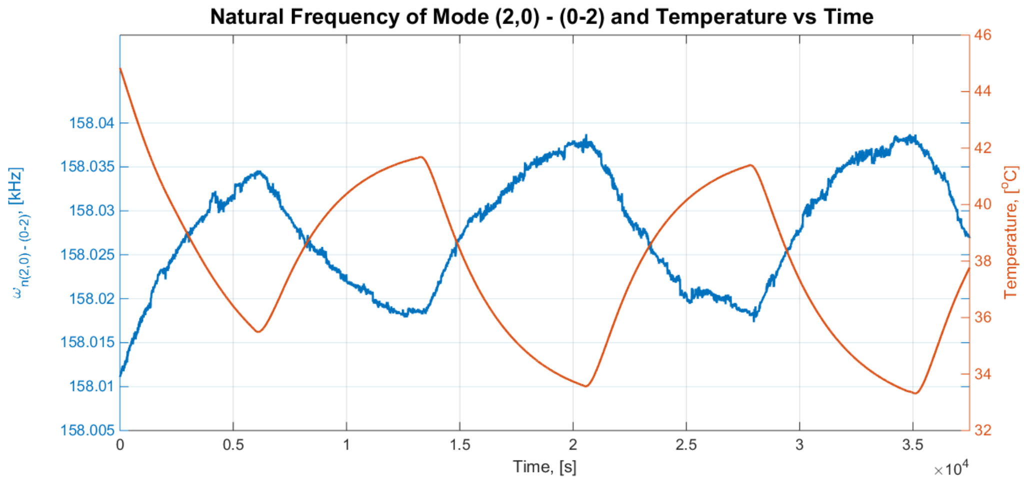

Figure 3.23: Natural frequency of mode (2,0) – (0,2) of the fabricated plate resonator and its temperature vs time.

The natural frequency shift of the fabricated device with a larger temperature range is also tested and corresponding response is given in Figure 3.24.

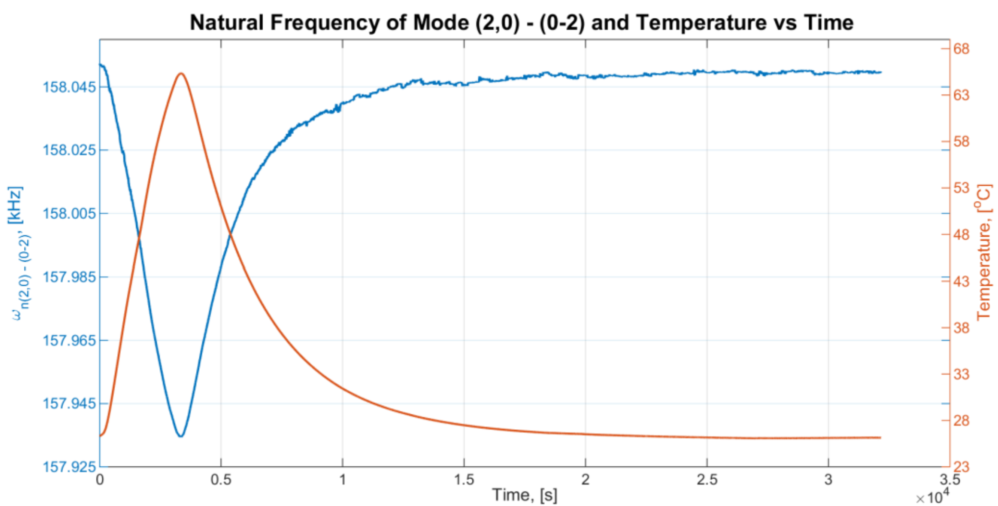

Figure 3.24: Natural frequency of mode (2,0) – (0,2) of the fabricated plate resonator and its temperature vs time in larger temperature range.

The scale factor for mode (2,0) – (0,2) is calculated to be 2.7211Hz/°C from the obtained results of system level temperature tests shown in Figure 3.25.

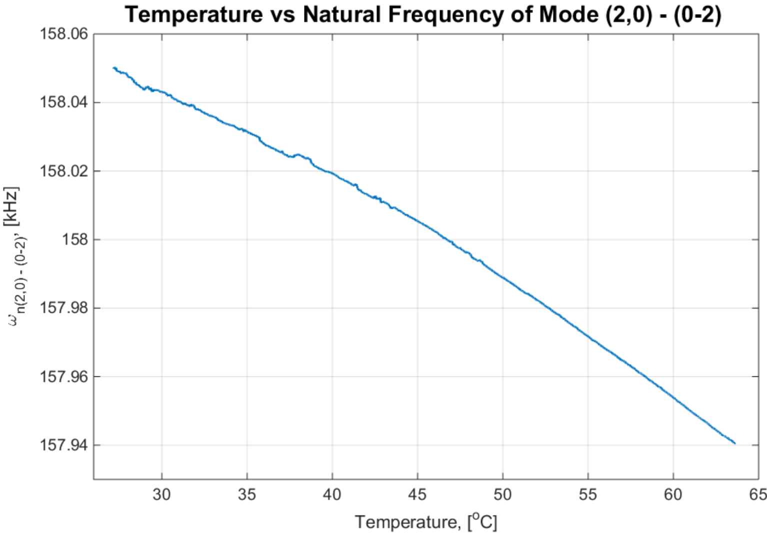

Figure 3.25: Change of natural frequency of mode (2,0) – (0,2) with respect to temperature.

The results are compared with the analytical model and FE simulation for the thermal effect in Figure 3.26. The results behave in the same manner; however, there is a discrepancy reasons of which are given above for the mode (1,1).

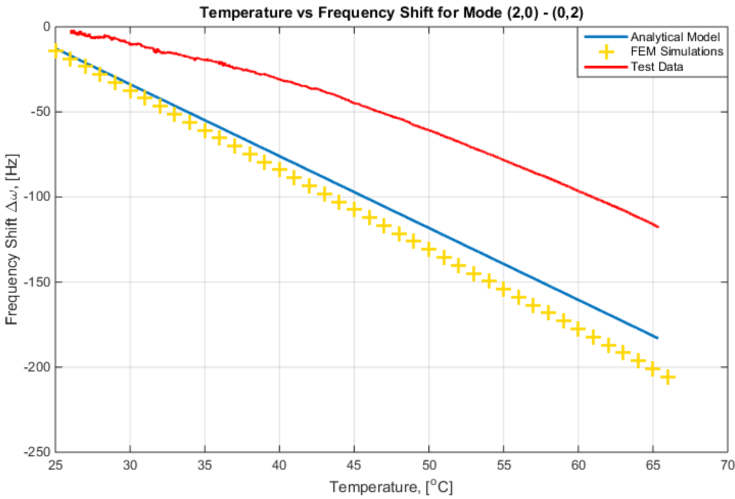

Figure 3.26: Test results of thermal effect on the natural frequency of mode (2,0) – (0,2) with analytical model and FE simulation for the temperature of 25-66°C.

To experimentally determine the maximum temperature resolution, the frequency data for mode (2,0) – (0,2) is acquired over 40000 seconds with a sample rate of 200 Hz (0.005 seconds sampling time). Obtained frequency data over a time is given in Figure 3.27. It should be noted that the collected data is for sensor and PLL electronics together.

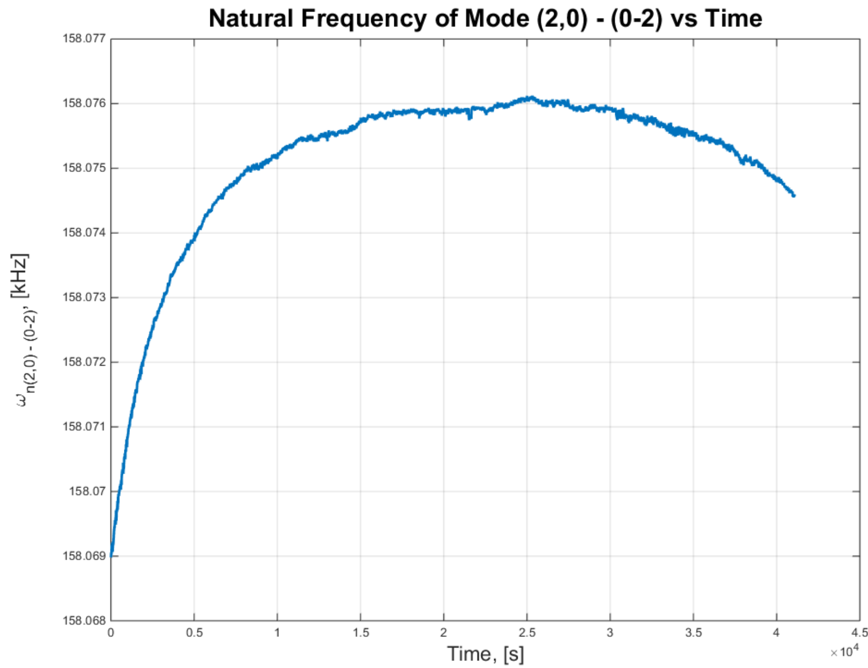

Figure 3.27: Natural frequency vs Time for mode (2,0) – (0,2) plot obtained from the data acquired over 40000s with a sampling rate of 200Hz for the sensor and PLL electronics together.

The frequency stability analysis is done using Allan variation method [56]. The Allan variance of the drift data is given in Figure 3.28. The Allan variance analysis is concluded that resolutions as low as 0.0001499°C are obtained for mode (2,0) – (0,2).

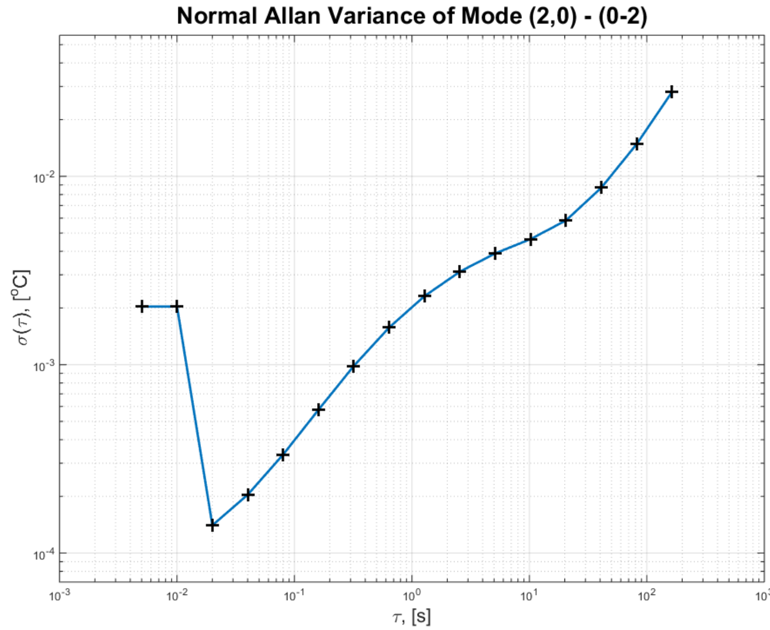

Figure 3.28: Allan variance plot for the natural frequency of mode (2,0) – (0,2). The Allan variance analysis is done to determine minimum detectable temperature.

3.4. Summary

In this chapter, the fabrication and characterization tests of resonant MEMS plate temperature sensor are presented. The SEM images of the fabricated devices are presented and fabrication imperfections are underlined. The test setup and results are presented in two categories; frequency response tests and system level temperature tests. The results of experiments are compared with the results obtained from analytical model and FE simulations.

Characterization of the fabricated devices divided into two stage; frequency response and system level temperature experiments. In the frequency response tests, the resonance frequency and Q-factor of mode (1,1) are measured to be 104.2 kHz and 14300, respectively. For mode (2,0) - (0,2), the measured resonance frequency and Q-factor are 156.68 kHz and 10700, respectively. All the frequency response tests are conducted at the ambient vacuum level of 20mTorr. The natural frequency results are slightly different than the model due to two main reasons being that there is a post

holding the plate which is not included into analytical model and microfabrication is not perfect as it has impurities. The LDV tests done at vacuum level of 0.364mTorr support the values obtained from frequency response test, analytical model and FE simulations. In addition, effect of electrostatic actuation is also tested for the proof mass voltage range of 0-40V. For proof mass voltage of 15V, frequency of (1,1) mode shifts 3.6Hz, which is in perfect agreement with the analytical model and FE simulation. As the proof mass voltage increased, test results verify the analytical model and FE simulation. At the maximum proof mass voltage, 40V, the frequency shift is around 26Hz. The frequency response tests are done between 22-66°C.

System level temperature tests are done with an implemented PLL controller to track frequency drifts with changing temperature. Tests are done at vacuum level of 0.405mTorr. Natural frequency of the fabricated plate tracks the temperature change, that is, natural frequency decreases as the temperature increases and vice versa. The scale factor of the fabricated sensor is obtained as 2.0214Hz/°C and 2.7211Hz/°C for mode shapes (1,1) and (2,0) - (0,2), respectively. The temperature equivalent frequency instability of the fabricated sensor is measured to be 0.3725mK for (1,1) mode shapes and 0.1499mK for (2,0) - (0,2) mode shape. When compared with the smart temperature sensors realized in the literature [57], the minimum detectable temperature values of 0.3725mK and 0.1499mK.

In conclusion, microfabrication of the designed sensors, the frequency response tests and system level temperature tests are successfully completed and the results are in great agreement with the analytical model and FE simulations, supporting the model to be used in further studies.

CHAPTER 4

CONCLUSION AND FUTURE WORK

In this research, a resonant MEMS plate temperature sensor is developed. The proposed application utilizes micro plate vibration to detect temperature of a substance which is in contact with the sensor. Within the scope of this research, the design, modelling, fabrication and characterization experiments of the sensor are carried out and reported. The conclusions drawn from the results of this research are summarized as follows:

- The theory, principles of operation and application areas of MEMS resonators are investigated. Temperature detection, MEMS resonators and plate vibrations are introduced separately. One of the driving and sensing method commonly used in MEMS devices, electrostatic actuation and detection, is introduced. The electrostatic softening effect is explained and modelled.

- The proposed application is explained in detail which is detecting temperature by tracking natural frequency shifts of the resonating micro plate. Each mode behaves different under the same temperature effect. The natural frequency shifts for mode (1,1) and mode (2,0) – (0,2) are compared.

- The theory of plate vibrations is examined in order to build a valid analytical model of the behavior of a transversely vibrating plate having four edges free to move. Transverse vibration of the plate modelled as a continuous media; however, it is seen that the analytical solution of the transverse vibration of the

plate with all edges free to move requires infinite series solution. Due to this impractical solution, Rayleigh and Rayleigh-Ritz method is applied. The effect of number of trial functions used in the solution of the problem is analyzed and optimized considering the computational power needed. The closed form analytical model of the natural frequencies and mode shapes of transversely vibrating plate is constructed.

- As the problem is composed of thermal, electrical and mechanical parts, analytical model of the mechanical part is developed with the addition of thermal and electrical effects. First the electrostatic softening effect, then the thermal effects are added to the mechanical model.

- The preliminary verification of the analytical model is done with FE simulations. The FE simulations are closer to actual system, but has some discrepancy due to the fact that effect of post and fringing fields are ignored in the analytical model. In the order of mechanical, electromechanical and thermo-electro-mechanical FE simulations are held in order to compare the electrical and thermal effects with the analytical model. The maxima of the operational parameters such as feasible range of proof mass voltage to be applied without pull-in and static deflections are determined based on the results obtained from FE simulations. Modal FE simulations are conducted in order to verify analytical model. Electromechanical FE simulations validates the analytical model with electrostatic softening effect. Lastly, results obtained from thermo-electro-mechanical analytic model and FE simulations are compared.

- The fabrication of the designed temperature sensors is performed with a silicon-on-glass process, aMEMS, which is an optimized, high yielding microfabrication process developed in METU MEMS Center. SEM images of the fabricated sensors are given to see the quality of the fabrication. The device layer thickness of the sensors is 35µm and side length of the square plate is 1400µm. In each die having lengths of 7.6mm x 7mm, two resonant MEMS plate temperature sensors are placed with 18 electrical pads.

- Characterization tests are divided into two parts; frequency response and system level temperature tests. The Q-factors of modes (1,1) and (2,0) - (0,2) are measured to be 14300 and 10700 at a vacuum pressure level of 20mTorr, respectively. Natural frequencies of modes-of-interest are measured to be very close to values obtained from analytical model and FE simulations. The LDV tests done at vacuum level of 0.364mTorr support the values obtained from frequency response test, analytical model and FE simulations. In addition, effect of electrostatic actuation is also tested for the proof mass voltage range of 0-40V and corresponding frequency shift is measured to be 0-26Hz. System level temperature tests are done with a PLL controller to track frequency drifts with changing temperature at vacuum level of 0.405mTorr. The scale factor of the fabricated sensor is obtained as 2.0214Hz/°C and 2.7211Hz/°C for mode shapes (1,1) and (2,0) - (0,2), respectively. The temperature equivalent frequency instability of the fabricated sensor is measured to be 0.3725mK for (1,1) mode shape and 0.1499mK for (2,0) - (0,2) mode shape.

Apart from these major achievements obtained from this research, below points should be considered as future work.

- All three dimension of the resonating plate should be decreased in order to get more portable device and measure more local temperatures. As the dimensions get smaller, the temperature sensor can be placed more precisely. Since the analytical model is verified with FE simulations and characterization tests, it is suggested to be used for further development.

- The readout circuitry and the electronic for PLL control should be printed in order to minimize the feedthrough capacitance. The vacuum chamber used in this study does not allow much room for all the circuitry to be placed nearby the sensor.

- In order to measure the exact temperature of the vibrating plate, a laser type temperature sensor should be used. In fact, a high precision temperature

controlled-oven would be a better solution for the tracking temperature of the resonating body.

- Higher mode shapes of the resonating plate should be analyzed in order to see the temperature characteristics of these modes. As the interested frequency gets higher, readout circuitry specifically the operational and instrumentation amplifiers may need to be changed.

- The developed thermal sensor can be used in IR detecting applications because of the reason that the working principle of the sensor is based on temperature of the resonating plate. For detecting the substrate temperature, the heat from the substance should reach to the plate and change its temperature. However, for IR applications, the heat energy directly comes to the plate in terms of infrared radiation.

- The diameter of the post should be decreased in order to reduce the heat transfer from plate to substrate by conduction, which will increase the temperature change of the plate as a result of incident radiation.

- For the IR detection application, it is better to isolate the detecting element, the micro plate, from rest of the structure thermally. Therefore, the micro plate should be suspended using inner or outer crab legs with a small cross sectional are to minimize the heat flow from the plate to the substrate.

- Since the fabrication flow is composed of very small number of masks, the cost of fabrication is low. Therefore, the resonant MEMS plate temperature sensors is a cost effective solution for thermal imaging as uncooled bolometers. Focal plane array (FPA) of resonant MEMS plate temperature sensors can also be realized for thermal imaging purposes.

REFERENCES

[1] R. P. Feynman. There's Plenty of Room at the Bottom [Online]. Available: http://www.phy.pku.edu.cn/~qhcao/resources/class/QM/Feynman's-Talk.pdf, [Last accessed: 23.05.2017]

[2] K. D. Wise, "Integrated Microsystems: Merging MEMS, micropower electronics, and wireless communications," in *Twelfth Annual IEEE International ASIC/SOC Conference (Cat. No.99TH8454)*, 1999, pp. 23-29.

[3] Y. Développement. (2015, 23.05.2017). *Status of the MEMS Industry 2015* [Online]. Available: http://www.yole.fr/iso_upload/Samples/Status_of_The_MEMS_Industry_2015_Sample.pdf, [Last accessed: 23.05.2017]

[4] K. Lightman. MEMS and Sensor Trends Smaller, Faster and Available to the Mass Market [Online]. Available: https://c.ymcdn.com/sites/memsindustrygroup.site-ym.com/resource/collection/A1DAAF83-11BC-4D42-A98F-BF250C325EE8/MEMS_and_Sensor_Trends_Smaller_Faster_and_Available_to_the_Mass_Market.pdf

[5] M. H. Sadd, *Elasticity Theory, Applicaions and Numerics*, 2 ed. Oxford, UK: Academic Press, 2009.

[6] E. F. F. Chladni, *Entdeckungen über die Theorie des Klanges*, 1787.

[7] S. Timoshenko, *Vibration Problems in Engineering*, Second ed. New York: D. Van Nostrand Company, INC., 1937.

[8] A. W. Leissa, *Vibrations of Plates*. Washington, DC: Office of Technology Utilization - National Aeronautics and Space Administration, 1969.

[9] A. W. Leissa, "The Free Vibration of Rectangular Plates," *Journal of Sound and Vibration,* vol. 31, pp. 257-293, 1973.

[10] S. F. Bassily and S. M. Dickinson, "On the Use of Beam Functions for Problems of Plates Involving Free Edges," *Journal of Applied Mechanics,* vol. 42, pp. 858-864, 1975.

[11] G. B. Warburton, "The Vibration of Rectangular Plates," *Proceedings of the Institution of Mechanical Engineers,* pp. 371-384, 1954.

[12] L. Rayleigh, *The Theory of Sound*, Second ed. New York: Dover Publications, 1894.

[13] S. Timoshenko and S. Woinowsky-Krieger, *Theory of Plates and Shells*. San Francisco: McGraw-Hill Book Company, 1987.

[14] A. C. Ugural, *Stresses in Beams, Plates and Shells*, 3 ed. Boca Raton: CRC Press Taylor and Francis Group, 2010.

[15] E. F. F. Chladni, *Die Akustik*: Leipzig, 1802.

[16] C. T. C. Nguyen, "MEMS technology for timing and frequency control," *IEEE Transactions on Ultrasonics, Ferroelectrics, and Frequency Control,* vol. 54, pp. 251-270, 2007.

[17] H. K. Lee, R. Melamud, B. Kim, M. A. Hopcroft, J. C. Salvia, and T. W. Kenny, "Electrostatic Tuning to Achieve Higher Stability Microelectromechanical Composite Resonators," *Journal of Microelectromechanical Systems,* vol. 20, pp. 1355-1365, 2011.

[18] H. Yuan-Ta, T. Sheng-Hsiang, F. Chiao-Li, W. Jian-Fu, T. Hann-Huei, and J. Ying-Zong, "Ultra-low power boost DC-DC converter with integrated MEMS

resonator," in *Power Electronics and Drive Systems (PEDS), 2015 IEEE 11th International Conference on*, 2015, pp. 711-714.

[19] K. Azgin and L. Valdevit, "The effects of tine coupling and geometrical imperfections on the response of DETF resonators," *Journal of Micromechanics and Microengineering,* vol. 23, p. 125011, 2013.

[20] K. Azgin, T. Akin, and L. Valdevit, "Ultrahigh-Dynamic-Range Resonant MEMS Load Cells for Micromechanical Test Frames," *Microelectromechanical Systems, Journal of,* vol. 21, pp. 1519-1529, 2012.

[21] T. Kose, K. Azgin, and T. Akin, "Temperature compensation of a capacitive MEMS accelerometer by using a MEMS oscillator," in *2016 IEEE International Symposium on Inertial Sensors and Systems*, 2016, pp. 33-36.

[22] S. Pala, M. Çiçek, and K. Azgın, "A Lorentz force MEMS magnetometer," in *2016 IEEE SENSORS*, 2016, pp. 1-3.

[23] K. Azgın, "High Performance MEMS Gyroscopes," Master of Science, Department of Electrical and Electronics Engineering, Middle East Technical University, Ankara, 2007.

[24] H. Yu and M. Rinaldi, "Spectrally selective infrared detector based on an ultra-thin piezoelectric resonant metamaterial," in *Micro Electro Mechanical Systems (MEMS), 2015 28th IEEE International Conference on*, 2015, pp. 984-987.

[25] M. B. Pisani, K. Ren, K. Ping, and S. Tadigadapa, "Application of Micromachined Y-Cut-Quartz Bulk Acoustic Wave Resonator for Infrared Sensing," *Microelectromechanical Systems, Journal of,* vol. 20, pp. 288-296, 2011.

[26] V. Agache, G. Blanco-Gomez, M. Cochet, and P. Caillat, "Suspended nanochannel in MEMS plate resonator for mass sensing in liquid," in *Micro*

Electro Mechanical Systems (MEMS), 2011 IEEE 24th International Conference on, 2011, pp. 157-160.

[27] M. H. Li, W. C. Chen, and S. S. Li, "CMOS-MEMS transverse-mode square plate resonator with high Q and low motional impedance," in *Solid-State Sensors, Actuators and Microsystems Conference (TRANSDUCERS), 2011 16th International*, 2011, pp. 1500-1503.

[28] M. U. Demirci and C. T. C. Nguyen, "Mechanically Corner-Coupled Square Microresonator Array for Reduced Series Motional Resistance," *Journal of Microelectromechanical Systems,* vol. 15, pp. 1419-1436, 2006.

[29] M. Shahmohammadi, K. Souri, and K. A. A. Makinwa, "A resistor-based temperature sensor for MEMS frequency references," in *2013 Proceedings of the ESSCIRC (ESSCIRC)*, 2013, pp. 225-228.

[30] P. Park, K. A. A. Makinwa, and D. Ruffieux, "A resistor-based temperature sensor for a real time clock with ±2ppm frequency stability," in *ESSCIRC 2014 - 40th European Solid State Circuits Conference (ESSCIRC)*, 2014, pp. 391-394.

[31] T. Köse, "Development of an Integration Resonant MEMS Temperature Sensor," Master of Science, Department of Mechanical Engineering, Middle East Technical University, Ankara, 2016.

[32] M. A. Hopcroft, "Temperature-stabilized Silicon Resonators for Frequency References," Doctor of Philosophy, Department of Mechanical Engineering, Stanford University, 2007.

[33] A. Rogalski, "Infrared detectors: an overview," *Infrared Physics & Technology,* vol. 43, pp. 187-210, 6// 2002.

[34] E. S. Barr, "The infrared pioneers—III. Samuel Pierpont Langley," *Infrared Physics,* vol. 3, pp. 195-206, 12// 1963.

[35] S. P. Langley, "The Bolometer and Radiant Energy," *Proceedings of the American Academy,* pp. 342-358, 1881.

[36] H. Yu and M. Rinaldi, "Ultra-fast and high resolution NEMS thermal detector based on a nano-air-gap piezoelectric resonant structure," in *Sensors, 2012 IEEE*, 2012, pp. 1-4.

[37] Y. Hui and M. Rinaldi, "High performance NEMS resonant infrared detector based on an aluminum nitride nano-plate resonator," in *Solid-State Sensors, Actuators and Microsystems, 2013 Transducers & Eurosensors XXVII: The 17th International Conference on*, 2013, pp. 968-971.

[38] H. Yu and M. Rinaldi, "Aluminum Nitride nano-plate infrared sensor with self-sustained CMOS oscillator for nano-watts range power detection," in *European Frequency and Time Forum & International Frequency Control Symposium (EFTF/IFC), 2013 Joint*, 2013, pp. 62-65.

[39] V. J. Gokhale and M. Rais-Zadeh, "Uncooled Infrared Detectors Using Gallium Nitride on Silicon Micromechanical Resonators," *Microelectromechanical Systems, Journal of,* vol. 23, pp. 803-810, 2014.

[40] P. Kao and S. Tadigadapa, "Micromachined quartz resonator based infrared detector array," *Sensors and Actuators A: Physical,* vol. 149, pp. 189-192, 2/16/ 2009.

[41] W. C. Chen, M. H. Li, Y. C. Liu, D. Weinstein, W. Fang, and S. S. Li, "Fully differential CMOS-MEMS square-plate oxide resonators with embedded poly-silicon electrodes," in *2013 Transducers & Eurosensors XXVII: The 17th International Conference on Solid-State Sensors, Actuators and Microsystems (Transducers & Eurosensors XXVII)*, 2013, pp. 2292-2295.

[42] M. H. Roshan, S. Zaliasl, K. Joo, K. Souri, R. Palwai, L. W. Chen*, et al.*, "A MEMS-Assisted Temperature Sensor With 20- $mu text{K}$ Resolution,

Conversion Rate of 200 S/s, and FOM of 0.04 pJK2," *IEEE Journal of Solid-State Circuits,* vol. 52, pp. 185-197, 2017.

[43] M. H. Roshan, S. Zaliasl, K. Joo, K. Souri, R. Palwai, W. Chen*, et al.*, "11.1 Dual-MEMS-resonator temperature-to-digital converter with 40 K resolution and FOM of 0.12pJK2," in *2016 IEEE International Solid-State Circuits Conference (ISSCC)*, 2016, pp. 200-201.

[44] S. Eminoglu, M. Y. Tanrikulu, and T. Akin, "A Low-Cost 128x128 Uncooled Infrared Detector Array in CMOS Process," *Journal of Microelectromechanical Systems,* vol. 17, pp. 20-30, 2008.

[45] B. E. Platin, M. Çalışkan, and H. N. Özgüven, *Dynamics of Engineering Systems*. Ankara: Middle East Technical University, 1991.

[46] J. Kim, D.-i. D. Cho, and R. S. Muller, "Why is (111) silicon a better mechanical material for MEMS ?," in *Proc. 11th Int. Conf. TRANSDUCERS*, Munich, Germany, 2001, pp. 662–665.

[47] K. G. Lyon, G. L. Salinger, C. A. Swenson, and G. K. White, "Linear thermal expansion measurements on silicon from 6 to 340 K " *Journal of Applied Physics,* vol. 48, pp. 865-868, 1977.

[48] H. Tada, A. E. Kumpel, R. E. Lathrop, J. B. S. Nieva, P. ZavrackyIoannis, N. Miaoulis*, et al.*, "Thermal expansion coefficient of polycrystalline silicon and silicon dioxide thin films at high temperatures," *Journal of Applied Physics,* vol. 87, pp. 4189-4193, 2000/05/01 2000.

[49] M. A. Hopcroft, W. D. Nix, and T. W. Kenny, "What is the Young's Modulus of Silicon?," *Microelectromechanical Systems, Journal of,* vol. 19, pp. 229-238, 2010.

[50] S. S. Rao, *Vibration of Continuous Systems*. New Jersey: John Wiley & Sons, 2007.

[51] S. S. Rao, *Mechanical Vibrations*, 5 ed. Upper Saddle River, NJ: Prentice Hall, 2011.

[52] T. A. W. Roessig, "Integrated MEMS Tuning Fork Oscillators for Sensor Appliations," Doctor of Philosophy, Department of Mechanical Engineering, University of California, Berkeley, 1998.

[53] M. M. Torunbalci, S. E. Alper, and T. Akin, "Advanced MEMS Process for Wafer Level Hermetic Encapsulation of MEMS Devices Using SOI Cap Wafers With Vertical Feedthroughs," *Microelectromechanical Systems, Journal of,* vol. 24, pp. 556-564, 2015.

[54] P. Sedat and A. Kıvanç, "A MEMS square Chladni plate resonator," *Journal of Micromechanics and Microengineering,* vol. 26, p. 105016, 2016.

[55] K. Azgın, "Very High Dynamic Range Resonant MEMS Load Cells for Micromechanial Test Frames," Doctor of Philosophy, Department of Mechanical and Aerospace Engineering, University of California, Irvine, 2012.

[56] W. J. Riley, *Handbook of Frequency Stability Analysis*. Washington: U.S. Government Printing Office, 2008.

[57] K. A. A. Makinwa. Smart Temperature Survey [Online]. Available: http://ei.ewi.tudelft.nl/ei/index.php/people-ei/17-group-makinwa/59-smart-temperature-sensor-survey, [Last accessed: 23.05.2017]